Chapter 4

The strength and stiffness of geocell support packs

4.1 Introduction

Geocell reinforced soil structures are composite structures comprising of the soil fill and the geocell membranes. The constitutive behaviour of the structure, therefore, is governed by the constitutive behaviour of these two components and their mechanical interaction.

An understanding of the constitutive behaviour of the two components is therefore a prerequisite for a better understanding of the constitutive behaviour of the composite. Of equal importance is the mechanical interaction between the two components, which, in turn, is influenced by the deformation mode and the boundary conditions imposed onto the geocell composite structure.

Due to the nature of the problem, the discussion presented in this chapter, is divided into three parts, focussing on the soil behaviour, the membrane behaviour and the composite behaviour, respectively. Although each part forms an independent unit, it must be read and understood within the context of the whole study.

The chapter is structured as follows:

- Sections 4.2 to 4.4 are devoted to understanding the constitutive behaviour of the cycloned gold tailings;
- Section 4.5 is devoted to the understanding of the membrane behaviour in uniaxial loading at different strain rates; and
- Section 4.6 and 4.7 focus on the behaviour of the geocell-soil composite structures.

4.2 Laboratory tests on fill material

4.2.1 Basic indicator tests

Specific gravity

The Specific gravity obtained for the classified tailings material is 2.75 Mg/m^3.

Stanley (1987) provides the mineral composition of a typical Witwatersrand gold reef. A simple calculation based on the percentage of occurrence of the minerals provided by Stanley (1987) (Table 4.1) and their individual values of Specific gravity indicate that one could expect the Specific gravity of the tailings products derived from the parent rock with the composition presented in Table 4.1 will have a specific gravity ranging between 2.7 and 2.8.

Table 4.1 The mineral composition of a typical Witwatersrand gold reef.

Mineral	Abundance	G_s
Quartz	70-90%	2.65
Muscovites and other Phyllosilicates	10-30%	2.8-2.9
Pyrites	3-4%	4.9-5.2
Other sulphides	1-2%	4-7
Grains of primary minerals	1-2%	
Kerogen[1]	1%	~2.2[2]

1. Kerogen = A form of carbon, common to the Witwatersrand gold mines.
2. Specific gravity of graphite.

Vermeulen (2001) worked on material from similar parent rock. The specific gravity of 2.75 obtained from a sample of the classified tailings material is remarkably close to the value of 2.74 recommended by Vermeulen as a good average for gold mine tailings from the Witwatersrand complex.

The value of 2.75 Mg/m^3 has been used in all relevant calculations for this study.

Material grading

The cycloned gold tailings is a uniformly graded silty fine sand and can be classified as an A-4 material according to the AASHTO Soil Classification System, and an ML material according to the Unified Soil Classification System. The material has a D_{50} = 0.065 mm, a C_u = 6.23 and a C_c = 1.28.

The cycloning process has the purpose of reducing the fraction of the material with a grain size < 40 μm. The cycloned tailings therefore consist of the silt and fine sand portion of the original tailings.

From the grading analysis it can be seen that the material consists of grains smaller that the 250 μm and larger than the 2 μm. It therefore seems that the cycloning process is effective in removing the clay-sized particles from the original mother material.

4.2.2 Microscopy on the material grains

The classified tailings consists of particles between about 250 μm and 2 μm. The study of the soil particles under both the light- and electron microscopes revealed a general similarity between the particle shape and surface textures throughout the whole range of particle sizes, although the < 20 μm portion seem to have more smooth surfaced particles and tend to be slightly more flaky.

The classified tailings generally consist of very angular to angular, sometimes sub-angular, irregularly shaped particles with sharp corners and edges. These particles are generally flattened, often elongated or needle shaped. Particle surfaces are generally either smooth or rough with the rougher particles tending to be sub-angular. These observations are consistent with the non-plastic nature of the material.

Vermeulen (2001) made similar observations on the sand portion of gold tailings. He pointed out that the angularity of a granular material has a profound influence on the engineering behaviour of the material. Under load, angular corners can break and crush, but tend to resist shear displacement while more rounded particles are less resistant to displacement and less likely to crush (Vermeulen, 2001).

Mittal and Morgenstern (1975) pointed out that the angularity of the grains affect the internal friction angle of the material and suggested that tailings should have slightly higher friction angles than natural sands as a result of the angularity of the particles.

Apart from the angularity, the flatness of the particles will also influence the engineering behaviour of the material. It is reasonable to expect that the generally flattened shape of the particles will result in a suppressed dilational behaviour compared to a more rotund sand with similar angularity.

4.2.3 Compaction characteristics of the classified tailings

The maximum dry density for the classified tailings obtained with the Modified AASHTO method was 1620 kg/m^3. Vermeulen performed, amongst others, the British Standard 'Heavy' compaction test, with an energy input equivalent to that of the modified AASHTO method, on whole gold tailings. The density of 1620 kg/m^3 is substantially lower than the value of 1850 kg/m^3 obtained for whole tailings.

This lower value for the maximum Modified AASHTO density for the classified tailings compared to whole tailings can be attributed to the fact that the classified tailings, due to the cycloning process, have a more uniform grain size distribution. Adding to this is the fact that the clay-sized particles that would act as void fillers in the whole tailings are absent in the classified tailings.

The compaction curve of the classified tailings is fairly flat, that is, the difference between the dry density at the optimum moisture content and the dry density at a lower moisture content is small. This can be expected, as a flat curve generally denotes a uniform grading and a curve with a pronounced peak, a well-graded soil (Road Research Laboratory, 1952).

Figure 4.1 shows results of compaction tests performed on coarse well-graded sand and fine uniformly graded sand (Road Research Laboratory, 1952). The compaction curve and grading curve for the classified tailings is also shown in the figure. The gradings and compaction curves of the fine uniform sand and the classified tailings are similar. The compaction characteristics of the classified tailings material is therefore similar to that of other fine uniform sands.

The minimum density of the classified tailings is 1234 kg/m^3 which is high compared to the minimum density of 867 kg/m^3 obtained by Vermeulen (2001) for whole tailings material.

The non-standard vibration test indicates that with an increase in energy the density of the material increases rapidly from the minimum density and tends towards an asymptote at about 1600 kg/m^3. This value is lower than the maximum density obtained from the modified AASHTO method. This can be attributed to particle crushing occurring in the modified AASHTO test or the fact that no surcharge was placed on the soil in the non-standard test, or possibly both these factors. For the purpose of relative density calculations, a minimum density of 1234 kg/m^3 and a maximum density of 1620 kg/m^3 were used.

4.2.4 Compression tests on soil

The interpretation of, and discussion on the performed compression tests, will be done in the following section concerned with the constitutive behaviour of the classified tailings.

4.3 The constitutive behaviour of the fill material

4.3.1 Elastic range

During the 1980's, researchers became increasingly aware of the marked difference between the stiffness of the soil at different strain levels. This has led to the following distinction between the different ranges of soil strain referred to in literature (Table 4.2) (Atkinson and Sallfors, 1991; Clayton and Heymann, 2001).

Table 4.2 Strain levels referred to in literature.

Strain level	Strain magnitude (%)
Very small strain	< 0.001
Small strain	0.001 – 0.1
Intermediate strain	0.1 – 1
Large strain	> 1

The importance of the small strain stiffness of soils is reflected in the vast amount of research that has been done on the subject in a relatively short period (Cf. Jardine et al., 1998)

For the purpose of understanding and modelling of the stress-strain behaviour of geocell support packs, however, in this study the interest lies with stiffness of the soil in the higher intermediate and large strain levels. For this purpose, the stiffness behaviour of the soil has been obtained from the isotropic compression test data following to the classical approach also followed by Vesic and Clough (1968).

Several non-linear models for the elastic behaviour of soils have been proposed (e.g. Vermeer, 1978). The approach followed here is based on the assumption that there is a linear relationship between the voids ratio and the logarithm of the mean effective stress. This assumption was first made by Roscoe et al. (1958) in the development of the critical state soil mechanics.

The elastic model that was fitted to the data is shown in Figure 4.2 and can be written as:

$$e = e_{\kappa} - \kappa \cdot \ln(p') \tag{4.1}$$

Where:

e = the voids ratio,

κ = the slope of the e-ln(p') line,

e_{κ} = the voids ratio of the material at ln(p')=0,

p' = the mean effective stress.

From the data presented in Chapter 3 it can be seen that the value of κ seems to be constant for the material over the ranges of stresses and densities that were tested. The value of e_{κ} varies linearly with density. This results from the linear relationship that exists between voids ratio and density, and the constant κ. The parameter, e_{κ}, is a function of the state of the material and can be obtained by using the following equation:

$$e_{\kappa} = e_0 + \kappa \cdot \ln(p'_0) \tag{4.2}$$

Where:

e_{κ} = the voids ratio of the material at ln(p')=0 for its current state,

e_0 = the voids ratio at the in-situ state,

κ = the slope of the e-ln(p') line,

p'_0 = the in-situ mean effective stress.

The fitted model and the original data are shown in Figure 4.3. The approach suggested by Roscoe et al. (1958) seems to adequately model the elastic material behaviour.

Using Equation (4.2), with basic elasticity theory it can be shown that:

$$E = \frac{3 \cdot (1 - 2 \cdot \nu)}{\kappa} \cdot (1 + e_{\kappa} \cdot \kappa \cdot \ln(p')) \cdot p' \tag{4.3}$$

Where:

E = the Young's modulus,

ν = the Poisson's ratio,

e_κ = the voids ratio of the material at ln(p')=0,

κ = the slope of the e-ln(p') line,

p' = the mean effective stress.

The Young's modulus is therefore non-linear and a function of the mean effective stress. In order to obtain the Young's modulus at a given stress state, the Poisson's ratio is needed. Data presented by Vesic and Clough (1968) for Chattahoochee river sand shows that although the Poisson's ratio is dependent on the confining stress, the Poisson's ratio can be assumed to be constant for stress ranges normally encountered in practice. The Poisson's ratio was therefore assumed to be constant for the material over the stress ranges and densities that were tested.

Vesic and Clough (1968) pointed out that an estimate of the Poisson's ratio of the soil can be obtained by combining the well-known relationship for an ideal elastic-isotropic solid,

$$\nu = \frac{K_0}{1 + K_0} \tag{4.4}$$

with Jáky's (1944, 1948) semi-empirical expression for the coefficient of earth pressure at rest,

$$K_0 = 1 - \sin(\phi') \tag{4.5}$$

Where:

ν = the Poisson's ratio,

K_0 = the coefficient of earth pressure at rest,

ϕ' = the Mohr-Coulomb friction angle.

Using these expressions, the calculated Poisson's ratio for the material is 0.25.

The value of the Poisson's ratio can also be estimated in the following manner: If one assumes elastic behaviour in the initial stages of the triaxial test, it can be shown from elasticity theory that the Poisson's ratio can be obtained from the tangent of the volumetric strain - axial strain curve ($\varepsilon_v / \varepsilon_a$) at the onset of the triaxial shear test.

The Poisson's ratio for the material was obtained by fitting the elastic volume change line through the data. The elastic volume change line is given by:

$$\varepsilon_v = \varepsilon_a \cdot (1 - 2 \cdot \nu) \tag{4.6}$$

The value of the Poisson's ratio for the soil that was obtained through this method is 0.23. Figure 4.4 shows ε_v against ε_a for the early stages of the test along with the elastic volume change line corresponding to a Poisson's ratio of 0.23.

Even though the Young's modulus of the material is not constant, the elastic strains for sands are normally small compared to the plastic strain and assuming a constant value will normally result in an insignificant error. An "equivalent" constant Young's modulus can be obtained from Equation (4.3) by assuming an average value for the mean effective stress, *p'*.

4.3.2 The strength and strain of the material at peak stress

The parameters presented here are corrected for the influence of the rough end platens used in the triaxial tests. The procedure used to obtain the corrected parameters is discussed in Section 4.4.4.

The Mohr-Coulomb friction angle

The strength of granular material is most often referred to in terms of the Mohr-Coulomb strength parameters, which for a cohesionless material can be written as:

$$\sin(\phi') = \frac{R-1}{R+1} \tag{4.7}$$

Where:

R = the principal stress ratio, $\frac{\sigma'_1}{\sigma'_3}$,

ϕ' = the Mohr-Coulomb friction angle.

The Mohr-Coulomb friction angle obtained from the test data is shown in Figure 4.5 with respect to the relative density and confining stress.

The friction angle increases with an increase in the relative density. Although this behaviour is shared by other granular materials (Figure 4.6), the rate at which the friction angle increase with an increase in the relative density seems

to be higher than that for the other materials for which the data is plotted in Figure 4.6.

Vesic and Clough (1968) compiled published data on sands tested at different confining stresses and performed tests on Chatahoochee River sand in a loose and dense state under confining stresses ranging from 100 kPa to 100 000 kPa. Alshibli et al. (2003) have performed tests under low confining stresses in conventional laboratories (σ_3 = 1.3 – 70 kPa) and at very low stresses (σ_3 = 0.05 – 1.3 kPa) under micro-gravity conditions aboard the NASA space shuttle. The data presented by Vesic and Clough (1969) and Alshibli (2003) is plotted together with the present test data in Figure 4.7.

It can be seen that for the tested material and for sand in general, the Mohr-Coulomb friction angle increases with a decrease in the confining stress. It is reasonable to expect an asymptote in the value of ϕ' with continued decrease in the confining stress (Bolton, 1986). The data by Alshibli et al. (2003) does not show that such an asymptote has been reached and suggests that, if such an asymptote exists, it will not be reached under normal stress conditions.

From Figure 4.7, it seems that a linear relationship between ϕ', and the logarithm of the confining stress exists.

The data of the samples prepared via the moist tamping method fit the overall trend better than the data from the dry compacted samples. Due to the process of dry compaction being more difficult than the moist tamping, it is possible that the scatter in the results of the dry compacted samples is larger than that of the moist tamped samples and that this increased scatter masks the trend visible in the other data.

The dilational behaviour

A very important factor that governs the behaviour of granular soils is the soil's volume change upon shearing. The plastic volumetric change of the soil is most often referred to in terms of the dilation angle, ψ.

Vermeer and De Borst (1984) suggested that the dilation angle of a material could be obtained from drained triaxial test data. Near the peak, the axial stress hardly increases with further straining of the sample. At this point, the elastic strain rate of the material is almost zero and the further strain increments are of a plastic nature. The slope of the $\varepsilon_v/\varepsilon_a$ curve at the axial strain where the peak

stress in the sample occur may thus be used to obtain the dilation angle with the following expression (Figure 4.8):

$$\sin(\psi_{max}) = \frac{\left(\frac{\partial \varepsilon_v}{\partial \varepsilon_a}\right)_{peak}}{2 + \left(\frac{\partial \varepsilon_v}{\partial \varepsilon_a}\right)_{peak}} \tag{4.8}$$

Where:

ψ_{max} = the maximum dilation angle of the material,

ε_v and ε_a = the volumetric and axial strain.

The values of ψ_{max} obtained from the triaxial test data are shown in Figure 4.9. The data are shown together with the data from F-75 Ottawa sand obtained by Alshibli et al. (2003) in Figure 4.10. The value of ψ_{max} increases with a decrease in the confining pressure.

The plastic volumetric behaviour of a dilative material is also sometimes referred to in terms of the dilational parameter, D_{max}, where:

$$D_{max} = \frac{1 + \sin(\psi_{max})}{1 - \sin(\psi_{max})} \tag{4.9}$$

Rowe (1962), Hanna (2001) and other researchers have shown an increase in D_{max} with an increase in the density of the material. Data of Hanna (2001), Rowe (1962), Cornforth (1964) Bishop and Green (1965) are shown in Figure 4.11.

According to theoretical and experimental findings of Rowe (1962, 1969), Horn (1965), and Hanna (2001), the value of D_{max} at peak stress is bounded by 1, at its loosest state and 2 at its densest state. Cuccovillo and Coop (1999), however, reported values for D_{max} of 4.9 for structured weakly cemented sands and values of 1.33 for the same sand in reconstituted state. Rowe (1969) observed that the limiting value of 2 is not necessarily reached by dense packings. This seems to be the case for the cycloned tailings material with a D_{max} of about 1.6.

This ma be attributed to the fact that the soil consists mainly of flattened and elongated particles (Cf. Section 4.2.2) as the flatness of the particles would result in a suppressed dilation behaviour, compared to soils consisting of more rotund particles.

Part of the scatter in the data shown in Figure 4.11 is due to the fact that the influence of the confining stress is ignored. The data of Alshibli et al. (2003) indicate a D_{max} of about 2 at a confining stress of 10 kPa and a D_{max} = 3 at confining stresses of 0.1 to 1 kPa.

Statistical analyses of the data for the cycloned tailings showed that the influence of the confining stress on D_{max}, for this material can be quantified as follows:

$$\frac{\partial D_{max}}{\partial \sigma_3} = 3.4 \cdot 10^{-4} \cdot \frac{1}{\text{kPa}} \tag{4.10}$$

Using this relationship the data in Figure 4.9 can be normalized to a constant value of confining stress by the following equation:

$$D_{max\,\sigma'_{3n}} = D_{max} + \frac{\partial D_{max}}{\partial \sigma'_3} \cdot \left(\sigma'_3 - \sigma'_{3n}\right) \tag{4.11}$$

Where:

$D_{max\,\sigma'_{3n}}$ = D_{max}, normalized to a confining stress of σ'_{3n}

Figure 4.12 shows the values of D_{max}, normalised to a confining stress of 100 kPa. The linear relationship shown in Figure 4.12 confirms the fact that both the density and the confining stress influence the dilation behaviour of the soil. For the range of stresses and densities that were tested, the relationship between D_{max} and both the density and confining stress can be assumed to be linear for the ranges of stresses and densities that were tested.

The plastic shear strain at peak stress

It has been mentioned earlier that the sample preparation method has an influence on the material behaviour. This can most clearly be seen in the comparison of the plastic shear strain at peak, $(\varepsilon_s^p)_{peak}$, the relative density, D_r, and the confining stress, σ'_3 (Figure 4.13).

Both the confining stress and the density of the material influences the value of $(\varepsilon_s^p)_{peak}$. Statistical analyses of the data has shown that the influence of the density of the material prepared by both the methods is the same and can be quantified as follows:

$$\frac{\partial\left(\left(\varepsilon_s^p\right)_{peak}\right)}{\partial D_r} = -0.229 \tag{4.12}$$

Using this relationship, the data can be normalized to a $D_r = 0$, for direct comparison as shown in Figure 4.14. It can be seen that the value of $(\varepsilon_s^p)_{peak}$ is influenced by the density, the confining stress and the sample preparation method.

The increase in the $(\varepsilon_s^p)_{peak}$ with an increase in the confining stress has also been shown by Han (1991) who performed biaxial tests on coarse Ottawa sand (Figure 4.15).

Of the three factors influencing $(\varepsilon_s^p)_{peak}$, the sample preparation has the largest influence. The difference in the material behaviour between the differently prepared samples may be attributed to a difference in the soil fabric that results from the difference in the preparation method.

Høeg et al. (2000) found a marked difference in the stress-strain behaviour of undisturbed and reconstituted silt and silty sand specimens, which they attributed to the difference in the soil fabric. They pointed out that even if the voids ratio is the same, the structural configuration of the particle assembly and the sizes and shapes of the individual voids might well be different in the undisturbed and reconstituted specimens. The same would apply to specimens prepared by dry compaction and moist tamping. Due to the flattened elongated nature of the particles, the presence of moisture would cause negative pore pressures between particles and one would expect a more open randomly orientated bookhouse structure.

As the negative pore pressures acting on the soil particles would tend to resist differential movement of the particles, this would also explain the fact that, to obtain a certain density, higher energy input is necessary with moist tamping compared to the dry compaction method.

4.3.3 The material behaviour in terms of the stress-dilatancy theory

The first reference to the dilational behaviour of granular soil is credited to Reynolds (1885), but the first attempts to quantify the influence of the dilational behaviour of a soil on its strength were made by Taylor (1948) and Bishop (1950). Further work on the theory was presented by Rowe (1962, 1969, 1971a), which became known as the stress-dilatancy theory.

Stress-dilatancy theory distinguishes between three components contributing to the strength of a granular soil. These components are the inter particle friction,

ϕ'_{μ}, the effect of particle reorientation and the dilational behaviour of the material (Figure 4.16).

Since the stress-dilatancy theory was first presented in 1962, it has met with both enthusiasm (e.g. Barden and Khayatt, 1966) and criticism (e.g. Bishop 1971). Many researchers have, however, worked on the theory and it has now been widely accepted as a useful framework for interpreting and modelling of the constitutive behaviour of granular material (e.g. Horn, 1965a; Horn, 1965b; Barden and Khayatt, 1966; Lee and Seed, 1967; De Josselin de Jong, 1976; Bolton, 1986; Wan and Guo, 1998; Hanna, 2001). It is within the framework of the stress-dilatancy theory that the constitutive behaviour of the tested material will be discussed.

Rowe's stress-dilatancy theory is normally presented in the following form:

$$R = D \cdot K \tag{4.13}$$

With:

$$R = \frac{\sigma'_1}{\sigma'_3}$$

$$D = 1 - \frac{\varepsilon_v^p}{\varepsilon_1^p}$$

$$K = \tan^2\left(\frac{\pi}{4} + \frac{\phi'_f}{2}\right)$$

Where:

ε_v^p = the plastic component of volumetric strain,

ε_1^p = the plastic component of the major principal strain,

ϕ'_f = the Rowe friction angle.

Stress-dilatancy theory is applicable to granular soil in both plane-strain and triaxial-strain compression loading conditions. Figure 4.17 presents typical results for dense and loose sand.

The limiting friction angles

The Rowe friction angle, ϕ'_f, is bounded by the inter-particle friction angle, ϕ'_{μ}, and the friction angle at constant volume, ϕ'_{cv}, so that:

$$\phi'_{\mu} \leq \phi'_f \leq \phi'_{cv} \tag{4.14}$$

The value of ϕ'_{μ}, is dependent on the nature of the mineral, the properties and roughness of its surface and on the size of the load per particle (Rowe, 1962).

Rowe suggest that the value of ϕ'_{μ} can be measured by sliding a mass of particles over a block of the same mineral with the same surface roughness, all surfaces being immersed in a chosen fluid. The results of direct measurement of quartz performed by Rowe (1962) are shown in Figure 4.18. Rowe states that the friction angle varied by about 1° in the pressure range 13 to 690 kPa.

Direct measurement of ϕ'_{μ} is, however, not practical. Hanna (2001) suggests using the value of R at peak stress with $D_{max} = 2$ to calculate the value of ϕ'_{μ}, and in similar vein the value of R at $D_{max} = 1$ to calculate the value of ϕ'_{cv}. This procedure implicitly assumes that the theoretical maximum value of D is equal to 2, and the method needs enough test results for which the value of D_{max} is near 2 and 1. It has been shown earlier that the maximum value of D is about 1.6 for the tested classified tailings. The method proposed by Hanna (2001) is therefore not applicable to the classified tailings material.

Figures 4.19 and 4.20 present the test results for all the tests in R-D space. The values of the limiting angles can be obtained by applying the theoretical relationships presented in Figure 4.17. The limiting values of $\phi'_{\mu} = 29.4 \pm 0.98°$ and $\phi'_{cv} = 34.38$ for the tested material is obtained in this manner. The value of ϕ'_{μ}, against the mean particle size is shown in Figure 4.18 with the direct measurement results of Rowe and data obtained by Hanna (2001).

Using the published data of 17 different sands, Bolton (1986) derived empirical relationships for the peak Mohr-Coulomb friction angle, ϕ', and ϕ'_{cv} as well as for the dilation rate. These relationships are:

$$\phi' - \phi'_{cv} = 0.8\psi_{max} = 5 \cdot I_r \quad \text{for plane strain conditions, and} \tag{4.15}$$

$$\phi' - \phi'_{cv} = 3 \cdot I_r \quad \text{and} \tag{4.16}$$

$$\left(\frac{d\varepsilon_v}{d\varepsilon_1}\right)_{max} = 0.3 \cdot I_r \quad \text{for triaxial strain conditions.} \tag{4.17}$$

With:

$$I_r = D_r \cdot \left(Q - \ln(p')\right) - P \tag{4.18}$$

Where:

I_r = the relative dilatancy index,
D_r = the relative density,
p' = the mean effective stress (kPa),
Q = a parameter with value 10,
P = a parameter with value 1 (The symbol, R, was used by Bolton (1986). P is used here as, R, is being used for

the principal stress ratio).

Figure 4.21 compares the value of *D* estimated from the relative density with Bolton's equation and the values measured for the cycloned tailings.

The values predicted by the equation of Bolton do not resemble the measured values. This discrepancy can be contributed to the fact that the maximum value of *D* for the cycloned tailings is about 1.6 compared to the value of about 2 at stress of about 300 kPa for the soils used in the study by Bolton. The dilational behaviour of the cycloned tailings is therefore overestimated for a particular relative density. These results seem to indicate that the equation for I_r (Equation (4.18)) is not applicable for the tested material.

Bolton related both the values of $(\phi' - \phi'_{cv})$ and the value of D_{max} to the parameter I_r. An estimate of the underlying relationship between the values of $(\phi' - \phi'_{cv})$ and D_{max} can therefore be obtained by eliminating the value of I_r from the expressions.

This can be achieved by way of substitution, resulting in the following expressions:

$$\phi' - \phi'_{cv} = 17 \cdot (D_{\max} - 1) \quad \text{for plane strain and} \tag{4.19}$$

$$\phi' - \phi'_{cv} = 10 \cdot (D_{\max} - 1) \quad \text{for triaxial strain conditions,} \tag{4.20}$$

Where:

D_{max} = the maximum value of *D.*

The value obtained for the ϕ'_{cv} for the tested material obtained in this manner is 35.2±0.9° (34.46±0.55° for the moist tamped samples and 35.39±0.38° for the dry prepared samples). These values are remarkably close to the value of 34.38° obtained directly from the triaxial test data.

Several relationships between the two limiting friction angles have been suggested in the past. These relationship, and an empirical relationship proposed by the author (Equation (4.21)) are discussed in Appendix B. Equation (4.21) is based on data presented in literature.

$$\phi'_{cv} = 0.0001373\phi'^{3}_{\mu} - 0.019\phi'^{2}_{\mu} + 1.67\phi'_{\mu} \tag{4.21}$$

Where:

ϕ'_{cv} = *the* Mohr-Coulomb friction angle at constant volume shearing,

ϕ'_{μ} = the inter-particle friction angle.

The work of Bolton (1986) and Horn (1969) along with the methods for the estimation of the limiting angles, ϕ'_{μ} and ϕ'_{cv}, presented here and by Hanna (2001) provides enough redundancy to obtain estimates of these limiting angles from triaxial tests, sufficiently accurate for normal use in practice.

The effect of particle reorientation

The value of ϕ'_f at peak stress can be obtained from the data, using Rowe's stress-dilatancy theory. These values are shown in Figure 4.22 with respect to the value of $(\varepsilon_s^p)_{peak}$.

The value of ϕ'_f at peak stress ranges between ϕ'_{μ} and ϕ'_{cv} and the author suggest that the following empirical equation can be used to model this phenomenon:

$$\phi'_f = \left(\phi'_{cv} - \phi'_{\mu}\right) \cdot \left(1 - e^{-b \cdot \left(\varepsilon_s^p\right)_{peak}}\right) + \phi'_{\mu} \qquad (4.22)$$

Where:

b = a parameter governing the rate of change of Rowe's friction angle between the two limiting angles.

This equation introduces an extra parameter, b, which needs to be obtained from triaxial test data. This can be done by fitting the presented equation through the data shown in Figure 4.22. The value of the parameter, b, for the tested soil is 14.

Predicting the peak strength of the soil

The strength of soil as a function of the density and the confining stress can be modelled using Rowe's stress-dilatancy theory along with the relationships for D_{max}, and $(\varepsilon_s^p)_{peak}$ as functions of D_r and σ'_3 and the relationship of ϕ'_f as a function of $(\varepsilon_s^p)_{peak}$

The measured and predicted values of R, are shown in Figure 4.23.

The predicted and measured values of R, using the relationship established earlier, cluster around the line of equality for both the moist tamped and dry compacted samples.

4.4 Formulation of a constitutive model for the fill material

For the sake of readability and flow of this chapter, the detailed discussion on the presented constitutive model and its components are presented in Appendix C, while a brief summary of each of the components of the model will be given in this section.

4.4.1 The elastic range

The elastic component of the material model has been discussed in the previous section.

4.4.2 The yield surface

A yield surface of the Mohr-Coulomb type is assumed which can be formulated as:

$$R = \frac{\sigma'_1}{\sigma'_3} = \frac{1+\sin(\phi'_{mob})}{1-\sin(\phi'_{mob})} \tag{4.23}$$

Where:

ϕ'_{mob} = the mobilized internal angle of friction.

4.4.3 The hardening behaviour and flow rule

The plastic shear strain, ε_s^p, is used as hardening parameter for this model and has proven adequate for the cycloned tailings. The plastic shear strain is defined as:

$$\varepsilon_s^p = \frac{\sqrt{2}}{3} \cdot \sqrt{\left(\varepsilon_1^p - \varepsilon_2^p\right)^2 + \left(\varepsilon_2^p - \varepsilon_3^p\right)^2 + \left(\varepsilon_3^p - \varepsilon_1^p\right)^2} \tag{4.24}$$

Where:

ε_s^p = the plastic shear strain,

ε_1^p, ε_2^p, ε_3^p = the plastic components of the major, intermediate and minor principal strain.

Non-associated flow is assumed according to the stress-dilatancy theory and the flow rule can be written as:

$$\sin(\phi'_{mob}) = \frac{\sin(\phi'_f)+\sin(\psi)}{1+\sin(\phi'_f)\cdot\sin(\psi)} \tag{4.25}$$

Where:

ϕ'_{mob} = the mobilized internal angel of friction,

ϕ'_f = the Rowe friction angle,

ψ = the dilation angle.

Normality is assumed in the deviatoric stress plane and the plastic potential will therefore have the same shape as the Mohr-Coulomb yield surface in the deviatoric stress plane, i.e. the plastic potential function, *g*, is given by:

$$g = \sigma'_1 + \sigma'_3 \cdot \left(\frac{1+\sin(\psi)}{1-\sin(\psi)} \right) \tag{4.26}$$

Where:

σ'_1 and σ'_3 = the major and minor effective principal stress,

ψ = the dilation angle.

Strain hardening of the material occurs before the peak strength and strain softening thereafter. The strain hardening/softening behaviour of the soil is written as a hardening/softening of the dilational component of the soil, and a hardening of the Rowe friction angle.

The strain hardening/softening equation for *D* is:

$$D = \begin{cases} (D_{\max} - D_0) \cdot f_1 + D_0 & \varepsilon_s^p \le \left(\varepsilon_s^p\right)_{peak} \\ (D_{\max} - 1) \cdot f_2 + 1 & \text{for } \left(\varepsilon_s^p\right)_{peak} < \varepsilon_s^p \le \left(\varepsilon_s^p\right)_{cv} \\ 1 & \varepsilon_s^p > \left(\varepsilon_s^p\right)_{cv} \end{cases} \tag{4.27}$$

Where:

D = Rowe's dilatancy parameter,

D_{max} = the maximum value of *D,*

D_0 = the initial value of *D* at the start of plastic deformation,

f_1 = the hardening function applicable to the pre-peak plastic strain,

f_2 = the hardening function applicable to the post-peak plastic strain.

The initial value of *D* at the start of plastic deformation is,

$$D_0 = \frac{1+\sin(\psi_0)}{1-\sin(\psi_0)} \tag{4.28}$$

With:

$$\sin(\psi_0) = \frac{\sin(\phi'_0) - \sin(\phi'_{initial})}{1 - \sin(\phi'_0) \cdot \sin(\phi'_{initial})}$$

Where:

$\phi'_{initial}$ = ϕ'_{cv} for plain strain conditions,

$\phi'_{initial}$ = ϕ'_{μ} for triaxial strain conditions,

ϕ'_0 = the internal angle of friction before the onset of work hardening.

The value of ϕ'_0 is a measure of the size of the initial Mohr-Coulomb yield surface and can be obtained from triaxial testing data with:

$$\sin(\phi'_0) = \frac{1 - R_0}{1 + R_0} \tag{4.29}$$

Where:

R_0 = the stress ratio at the start of plastic behaviour.

The hardening function applicable to the pre-peak plastic strain is:

$$f_1 = \frac{2 \cdot \sqrt{\varepsilon_s^p \cdot (\varepsilon_s^p)_{peak}}}{\varepsilon_s^p + (\varepsilon_s^p)_{peak}} \tag{4.30}$$

Where:

ε_s^p = the hardening parameter, plastic shear strain,

$(\varepsilon_s^p)_{peak}$ = the plastic shear strain at peak strength.

The hardening function applicable to the post-peak plastic strain is:

$$f_2 = 1 - A^2 \cdot (3 - 2 \cdot A) \tag{4.31}$$

With:

$$A = \left(\frac{\ln(\varepsilon_s^p) - \ln((\varepsilon_s^p)_{peak})}{\ln((\varepsilon_s^p)_{cv}) - \ln((\varepsilon_s^p)_{peak})} \right)$$

Where:

ε_s^p = the hardening parameter, plastic shear strain,

$(\varepsilon_s^p)_{peak}$ = the plastic shear strain at peak,

$(\varepsilon_s^p)_{cv}$ = the plastic shear strain at which the dilation parameter can be assumed to be 1.

The change in ϕ'_f between ϕ'_μ and ϕ'_{cv} can be modelled as a work hardening process using the following equation:

$$\phi'_f = \left(\phi'_{cv} - \phi'_\mu\right) \cdot \left(1 - e^{-b \cdot \varepsilon_s^p}\right) + \phi'_\mu \tag{4.32}$$

Where:

b = a parameter governing the rate of change of Rowe's friction angle between the two limiting angles.

This equation is equivalent to Equation (4.22) presented in the previous section for ϕ'_f at peak and the b parameter is the same.

With the equations presented in this section the mobilized dilation and friction angles can be obtained as a function of the plastic shear strain. The model can therefore easily be implemented into analytical calculation procedures and numerical analysis codes.

4.4.4 Obtaining parameters

It has long been recognized that the friction on the end platens in triaxial testing has an influence on the triaxial tests and therefore the parameters obtained from it. End restraints cause stress concentrations and retards lateral strain near the platens. The influence of the end restraints on the strain distribution within a sample is shown by the results of experiments performed by Deman (1975) (Figure 4.24).

In a work hardening material, a non-uniform strain distribution results in a non-uniform distribution of friction and dilation parameters. This manifest itself in an increased strength and decreased axial and volumetric strain for a sample tested with end restraints compared to a sample tested with free ends (Figure 4.25).

For discussion purposes the following three factors are defined:

$$f_R = \frac{R_L}{R_n}, \qquad f_\varepsilon = \frac{\varepsilon_{aL}}{\varepsilon_{an}}, \quad \text{and} \quad f_\psi = \frac{\psi_{aL}}{\psi_{an}} \tag{4.33}$$

Where:

R_L = the value of R obtained from a triaxial test with free ends,

R_n = the value of R obtained from a triaxial test with fixed ends,

ε_{aL} = the axial strain at peak obtained from a triaxial test with free ends,

ε_{an} = the axial strain at peak obtained from a triaxial test with fixed ends,

ψ_{aL} = the peak dilation angle obtained from a triaxial test with free ends,

ψ_{an} = the peak dilation angle obtained from a triaxial test with fixed ends.

Utilizing numerical analysis software FLAC3D, and implementing the model presented above, the material parameters applicable to a uniformly strained sample can be back calculated using the following procedure:

1. Calculate the parameters from the uncorrected conventional triaxial test data.
2. Run numerical analysis.
3. Compare curves and estimate multiplication factors f_R and f_ε and f_ψ.
4. Estimate new parameter set with:

$$\psi_{\max} = f_\psi \cdot \psi_{\max\_measured}$$

$$R = f_R \cdot R_{measured}$$

$$\varepsilon_a = f_\varepsilon \cdot \varepsilon_{a\_measured}$$

5. Update estimations of the limiting friction angles and the *b* parameter.
6. Repeat steps 2 to 5 until satisfactory results are obtained.

This procedure was performed for all the triaxial tests performed on the cycloned tailings. It was found that 3 iterations of the above mentioned procedure gave satisfactory results. With this procedure, f_R values ranging between 0.93 and 0.96 were obtained. This compares well with experimental data on Mersey River sand presented by Rowe and Barden (1964) where the denser samples exhibited an f_R of about 0.95. A value for f_ε of 1.125 was obtained through the above-mentioned procedure. Bishop and Green (1965) present data on Ham River sand that indicate a value for f_ε of about 1.25.

It was found that for this study the value of f_ψ could be assumed to be 1. Bishop and Green (1965) state that the end constraints on the test sample reduces the volumetric strain of the whole sample taking place during the shearing process, but has very little influence on the peak dilation rate.

This may be due to the fact that the change in the dilational parameter, *D*, with a change in the plastic shear strain, ε_s^p, is close to zero near the peak strain, that is, the dilation angle is fairly constant near the peak strain. An element of the material that is at a state slightly before peak and slightly after peak all have a dilation angle close to that at the peak. This results in a situation where the largest part of the sample has a dilation angle close to the peak value at the sample peak strain, even though only a small portion of the sample is at the peak strain.

4.4.5 Comparison of model and data

The original data obtained from the triaxial tests shown in Chapter 3 is shown in

Figure 4.26 to 4.29 with the results of numerical simulation of the same tests.

The parameters used in these numerical simulations were back calculated according to the procedure presented above. In the numerical models the sample was fixed horizontally at the ends to model the constraints applicable to conventional triaxial tests on granular soil.

The agreement between the test data and the numerical simulations indicate that the simple constitutive model presented, satisfactorily represent the tested material behaviour under triaxial compression loading conditions.

The numerical modelling procedure did not model the strain localization and sudden strength drop evident in the test data is not visible in the modelled behaviour.

4.5 The behaviour of the HDPE membrane

From the data on the uniaxial stress-strain response of the HDPE membranes presented in Chapter 3, it can be seen that the strength and stiffness of the geocell membranes are strain-rate-dependent. The influence the membrane behaviour has on the behaviour of the composite structure, can only be understood and quantified if the strain-rate-dependent stress-strain behaviour of the membranes is quantified. This is even more important because the strain rate of the membrane in the field application is generally lower than the strain rate practically achievable in the laboratory.

Complex viscoelastic and viscoplastic models for the strain-rate-dependent behaviour of HDPE exist (e.g. Zhang and Moore, 1997b; Beijer and Spoormaker, 2000; Nikolov and Doghri, 2000) but these, unfortunately, do not provide the engineer with a practical model that can be incorporated into normal design procedures.

Two simple mathematical models for the strain-rate-dependent stress-strain curve for the HDPE membranes under uniaxial loading conditions are presented in this section.

4.5.1 Interpretation of the test results

In the interpretation of the test results of the uniaxial tensile tests on the membrane material several assumptions are made regarding the behaviour of the membranes:

Although anisotropy in the membrane behaviour exists in the plane of the membrane due to the manufacturing process, the membrane is expected to be isotropic over the cross section of the membrane. It is therefore assumed that the membrane is isotropic and homogeneous over the cross section of the membrane. This assumption is often made, explicitly or implicitly, when interpreting test results on membranes (e.g. Merry and Bray, 1997) and deemed acceptable.

It is also assumed that, when tested, the membranes were perfectly clamped with respect to the length of the specimen, that is, the axial strains have developed only in the specimen length between clamps. Inspection of the specimens after testing has shown that this assumption is acceptable.

Similar to Merry and Bray (1997) it is assumed that in the middle of the specimen, the membrane deforms as a prismatic bar that is unrestrained with respect to lateral deformation and that the stress through the middle portion of the specimen is uniform and equal to the average stress. Merry and Bray (1997) have found this assumption to be acceptable. In this regard, it was also assumed that an aspect ratio (w/L) of 0.5 is small enough to result in a uniaxial stress distribution in the central half of the specimen and a uniform stress distribution in the central quarter.

Figure 4.30 shows the measured deformation pattern for one of the tests. From this figure, it can be seen that the deformation profile for the central half of the specimen is essentially uniform. It therefore seems that the observed deformation profile supports the assumption of a uniaxial stress field in the central half of the specimen.

Further support for the assumption was obtained from numerical analyses. The numerical analyses software, FLAC3D was used to model the laboratory tests. For this purpose, one of the geomembrane stress-strain models presented in the Section 4.5.3 was used to model the constitutive behaviour of the membrane elements. Figure 4.31 to 4.34 shows the deformed grid and the contour plots of the vertical stress, horizontal in-plane stress and the in-plane shear stress in the membrane. The plots of shear stress and horizontal in-plane stress show that the central half of the sample is loaded uniaxially. From the plot of vertical stress, it can be seen that vertical stress in the central quarter of the sample is essentially uniform.

The measurement of local longitudinal strain

Figure 3.26 compares the local strain measurements to the strain from the grip separation. The difference between the longitudinal strain calculated from grip separation and the local longitudinal strain is small for strain values less than 0.5. For practical purposes, the difference between the two strain values could be ignored, at least up to strains of 0.2. Data presented by Merry and Bray (1996) for wide strip tensile tests on both HDPE and Polyvinyl Chloride (PVC) membranes support this conclusion (Figure 4.35).

The measurement of engineering Poisson's ratio

Previous studies (e.g. De Lorenzi et al., 1991 and Merry and Bray, 1996) have shown that polymeric materials such as HDPE and PVC can be assumed to be

constant volume materials. Constant volume materials have a true (or natural) Poisson's ratio of 0.5 where the true Poisson's ratio is defined as: (Merry and Bray, 1996)

$$\nu = \frac{\varepsilon_{tl}}{\varepsilon_{ta}} \tag{4.34}$$

Where:

ν = the true Poisson's ratio of the material,

ε_{tl} = the true lateral strain,

ε_{ta} = the true axial strain.

When engineering strains are used, the Poisson's ratio is formulated as

$$\nu = \frac{\varepsilon_{el}}{\varepsilon_{ea}} \tag{4.35}$$

Where:

ν = the engineering Poisson's ratio of the material,

ε_{el} = the engineering lateral strain,

ε_{ea} = the engineering axial strain.

The engineering Poisson's ratio for a constant volume material can be expressed as: (Giroud, 2004)

$$\nu = \frac{1}{\varepsilon_a}\left(1 - \frac{1}{\sqrt{1+\varepsilon_a}}\right) \tag{4.36}$$

Where:

ν = the engineering Poisson's ratio of the material,

ε_a = the axial strain of the material.

From this expression, it can be seen that the engineering Poisson's ratio is equal to 0.5 only at infinitesimal strains. From the data presented in Chapter 3, it can be seen that the engineering Poisson's ratio for the HDPE membrane reduces throughout the test.

Assuming that necking of the specimen is limited to 15% of the specimen length on each side of the specimen, Giroud (2004) has shown that the measured Poisson's ratio will overestimate the true Poisson's ratio by about 15%. For the membranes tested in this study, this assumption seems to be acceptable (Figure 4.30).

The theoretical relationship between the longitudinal and lateral strain of the membrane is plotted together with the data in Figure 4.36. This relationship was obtained from the theoretical expression presented by Giroud, by multiplying the Poisson's ratio by 1.15 to take account of necking.

The data regarding the engineering Poisson's ratio of the HDPE membrane were obtained from tests performed at different strain rates. Although a limited range of strain rates were achievable in the laboratory was used, the data suggest that the strain distribution and the engineering Poisson's ratio are strain, but not strain-rate-dependent. It also seems that the Poisson's ratio is independent of the loading history. This can be seen from the fact that the data obtained from the permanent deformations after the tests, plot together with the data obtained during the tests.

The amount of permanent deformation in the membranes after they were removed from the test machine is dependent on the strain at the end of the test, the rate at which the membrane were strained and the amount of creep that took place between the end of the test and the time the specimen was unloaded. These factors resulted in the data obtained from the direct measurements taken after the tests to range between local longitudinal strain values of 0.2 and 1.2. It therefore appears that the measurement of the lateral strain during the test is not necessary. The relationship between the longitudinal and lateral strain could be obtained from direct measurements after completion of the tests, provided that the membranes did not rupture or failed due to localised necking (cold drawing).

4.5.2 Membrane behaviour

The stress-strain results shown in Chapter 3 are given in terms of engineering stress and engineering strain. This is the way tensile test results are most often presented. Assuming that the plastic behaves isotropically over the cross section of the membrane, the reduction in both the width and thickness of the membrane can be corrected for, by applying the measured lateral strain to both the width and the thickness. The "true" membrane stress can therefore be calculated. The geomembrane stress-strain response, in terms of "true" membrane stress and engineering strain, is shown in Figure 4.37. The true stress in the membranes seems to increase continuously. At high strain, the stress increases linearly with the engineering strain. The continued increase in the true stress in the HDPE and the linear relationship between true stress and strain is confirmed by the qualitatively similar stress-strain curves shown by

Beijer and Spoormaker (2000) and Zhang and Moore (1997a) up to the strain levels of 0.22 and 0.14 respectively.

For discussion purposes and for the purpose of the mathematical model presented in Section 4.5.3 the "transition" point on the stress-strain curve will be defined as the point where the non-linear behaviour of the material ends and the linear behaviour starts. The transition point could be found by fitting a line through the linear part of the data after the transition point and determining the point of separation between the fitted line and stress-strain curve (Figure 4.38).

For the data presented here, the transition strain was chosen at 0.16. Due to the asymptotic nature of the difference between the stress-strain curve and the fitted line, the transition strain is subject to some margin of error and a subjective judgment of the value of the transition strain must be made. However, differences arising from the small errors in identifying the transition strain values will be small.

The transition strain of 0.16 for the tested membranes compares well with the value of about 0.15 for the transition strain for bars of injection moulding grade HDPE tested by Beijer and Spoormaker (2000).

From Figure 4.37 it seems that the transition strain is independent of strain rate. As the tests were done with strain rates varying over 3 orders of magnitude, this conclusion could be made with some confidence. Data for tests performed by Beijer and Spoormaker (2000) with strain rates varying over 5 orders of magnitude, also support this conclusion.

Figure 4.39 shows the relationship between the transition stress and the strain rate. For strain rates between 0.1%/min and 20%/min there seems to be a linear relationship between the transition stress and the logarithm of the strain rate. For strain rates below 0.1%/min the rate of change in the transition stress with reduction in the strain rate reduces for lower values of strain rate. This behaviour is also shown by Beijer and Spoormaker (2000) for injection moulding grade HDPE bars (Figure 4.40). The transition stress obtained from data presented by Merry and Bray (1997) for bi-axial tests on HDPE geomembranes shown in Figure 4.40 also follows the above-mentioned behaviour at low strain rates.

Beijer and Spoormaker (2000) suggest that this behaviour can be attributed to two parallel plastic processes: At low strain rates only one process contributes

to the total measured stress, at higher strain rates, the second process starts to carry load which leads to a stiffer yield behaviour.

At strain rates higher than 20%/min, a reduction in the rate at which the transition stress increases with an increase in the strain rate is shown for the membranes tested in the current programme. The membranes tested bi-axially by Merry and Bray (1996) seem to behave similarly.

It therefore seems that the transition stress will reach an asymptote both at very low and very high strain rates.

The stress-strain curves shown in Figure 4.37 can be normalised by dividing the membrane stress by the transition stress value. The normalized stress-strain curves are shown in Figure 4.41. From this figure, it can be seen that both the magnitude and the form of the stress-strain function changes with strain rate. Data from the tensile tests performed on bars of injection moulding grade HDPE performed by Beijer and Spoormaker (2000) and the data from compression tests on material from HDPE pipes tested performed by Zhang and Moore (1997a) show qualitatively similar normalised stress-strain curves (Figure 4.42). The normalized stress-strain behaviour seems not to be strongly dependent on the strain rate, as the normalized stress-strain curves do not differ significantly for the strain rates tested in the laboratory.

4.5.3 Formulation of mathematical models for the membrane behaviour

Two mathematical models for the strain-rate-dependent stress-strain curve for the HDPE membranes under uniaxial loading conditions are briefly presented in this section and discussed in detail in Appendix D.

The hyperbolic model for uniaxial loading

The hyperbolic model consisting of a form function ($B(\dot{\varepsilon})$) and magnitude function ($\sigma_t(\dot{\varepsilon})$) which can be written as:

$$\sigma(\varepsilon,\dot{\varepsilon}) = B(\varepsilon,\dot{\varepsilon})\cdot\sigma_t(\dot{\varepsilon}) \tag{4.37}$$

Where:

$$B(\varepsilon,\dot{\varepsilon}) = \begin{cases} \dfrac{\varepsilon}{\beta(\dot{\varepsilon})\cdot\varepsilon_t + (1-\beta(\dot{\varepsilon}))\cdot\varepsilon} & \text{if } \varepsilon \le \varepsilon_t \\ 1 + \dfrac{\beta(\dot{\varepsilon})}{\varepsilon_t}\cdot(\varepsilon-\varepsilon_t) & \text{if } \varepsilon > \varepsilon_t \end{cases} \tag{4.38}$$

With

ε and $\dot{\varepsilon}$ = the strain and strain rate,

$\beta(\dot{\varepsilon})$ and $\sigma_t(\dot{\varepsilon})$ are strain-rate-dependent functions that can be written as:

$$\sigma_t(\dot{\varepsilon}) = \frac{\sigma_{t\,max} - \sigma_{t\,min}}{1 + e^{-d_\sigma \cdot \ln(\dot{\varepsilon}) - e_\sigma}} + \sigma_{t\,min} \tag{4.39}$$

Where:

d_σ and e_σ = the parameters obtained from fitting the equation to the data,

$\sigma_{t\,max}$ and $\sigma_{t\,min}$ = the maximum and minimum asymptote value of the transition stress,

$\dot{\varepsilon}$ = the strain rate.

and

$$\beta(\dot{\varepsilon}) = \frac{\beta_{max} - \beta_{min}}{1 + e^{-d_\beta \cdot \ln(\dot{\varepsilon}) - e_\beta}} + \beta_{min} \tag{4.40}$$

Where:

d_β and e_β = parameters obtained from fitting the equation to the data,

β_{max} and β_{min} = the maximum an minimum asymptote value of β,

$\dot{\varepsilon}$ = the strain rate.

The parameters for the above mentioned model obtained from the data are presented in Table 4.3.

Table 4.3 Parameters for the hyperbolic model obtained from data.

β				σ_t				ε_t
β_{max}	β_{min}	d_β	E_β	$\sigma_{t\,max}$	$\sigma_{t\,min}$	d_σ	e_σ	
0.304	0.187	0.6	0.35	15	7.45	0.737	-0.345	0.16

Figure 4.43 compares the form function, *B,* using the parameters given in Table 4.3 with the normalized data. The curves in the figures are limited to 4 for the sake of clarity. Figure 4.44 shows the original data with the model curve using the parameters in Table 4.3. The model lines in Figure 4.44 match the data slightly less than in Figure 4.43. This is due to the scatter of the transition stress around the assumed logarithmic relationship (Figure 4.39). It is believed that the scatter is partly due to the limited accuracy with which the thickness of the 0.2 mm membrane could be measured.

The hyperbolic model, although adequate for describing the geomembrane behaviour, has two important drawbacks: the necessity for choosing a transition point and the fact that the model consists of two separate equations for the regions before and after the transition point. Another model that does not suffer these drawbacks is the exponential model presented in the following section.

An exponential model for uniaxial membrane loading

The following empirical equation (Equation (4.41)) can also be used to model the geomembrane behaviour under uniaxial loading conditions:

$$\sigma(\varepsilon,\dot{\varepsilon}) = \left(a(\dot{\varepsilon})\cdot\varepsilon + c(\dot{\varepsilon})\right)\cdot\left(1 - e^{-b\cdot\varepsilon}\right) \tag{4.41}$$

Where

b = a parameter that can be obtained from simple laboratory tests,

ε and $\dot{\varepsilon}$ = the strain and strain rate.

The strain-rate-dependent functions $c(\dot{\varepsilon})$ and $a(\dot{\varepsilon})$ are:

$$c(\dot{\varepsilon}) = \frac{c_{max} - c_{min}}{1 + e^{-d_c\cdot\ln(\dot{\varepsilon})-e_c}} + c_{min} \tag{4.42}$$

Where:

d_c and e_c = parameters obtained from fitting the equation to the data,

c_{max} and c_{min} = the maximum and minimum asymptote value of the c parameter,

$\dot{\varepsilon}$ = the strain rate.

and

$$a(\dot{\varepsilon}) = \frac{a_{max} - a_{min}}{1 + e^{-d_a\cdot\ln(\dot{\varepsilon})-e_a}} + a_{min} \tag{4.43}$$

Where:

d_a and e_a = parameters obtained from fitting the equation to the data,

a_{max} and a_{min} = the maximum and minimum asymptote value of a,

$\dot{\varepsilon}$ = the strain rate.

The parameters obtained from the data are shown in Table 4.4. Figure 4.45 compares the exponential model and the original data, using the parameters from Table 4.4. The exponential model compares favourably with the hyperbolic model.

Table 4.4 Parameters for the exponential model obtained from data.

a				***c***				***b***
a_{max}	a_{min}	d_a	e_a	c_{max}	c_{min}	d_c	e_c	
17.54	14.12	1.931	1.172	12.45	4.79	0.651	-0.287	32.52

4.5.4 Model interpolation and extrapolation

In order to understand and quantify the long-term behaviour of the geocell-soil composite, it is necessary to obtain the stress-strain response for the geomembranes at very low strain rates. Due to time and practical constraints, performing laboratory tests at strain rates comparable to those expected in field conditions, is not a viable option.

The absence of test data for strain rates lower than that practically achievable in the laboratory can be overcome by the ease by which the currently presented models can be extrapolated to strain rates lower than those tested in the laboratory.

Cyclic compression tests performed by Zhang and Moore (1997a) on HDPE material recovered from manufactured pipes showed that the HDPE did not undergo cyclic hardening (Figure 4.46a). They also performed tests at a constant initial strain rate, which was changed to another constant strain rate during the tests (Figure 4.46b). They observed that after a brief period of rapid stress change, the stress attains the level it would have held if the new strain rate had been used from the beginning of the test. The memory of the previous strain rate is therefore conserved only during a brief adjustment period. This strain history need therefore not be taken into account for design purposes and a design stress-strain curve for an appropriate strain rate will suffice for most design purposes.

Using Equation (4.39) and Equation (4.42) estimates of the σ_t and c at the desired strain rates can be obtained. Values of β and a can be obtained by extrapolation via the appropriate equations. The stress-strain curves is not

sensitively dependent on the values of β or *a* and accuracy in the extrapolation of these parameters is of lesser importance.

Extrapolation of the two models presented here, outside of the range of laboratory tested strain rates provides a procedure for obtaining a design stress-strain curve at low strain rates. As this cannot be substantiated by test data, such extrapolations should be done with caution.

4.6 The constitutive behaviour of soil reinforced with a single geocell

It was shown in Chapter 2 that little research on the interaction of the components of geocell reinforced soil has been done. Notable exceptions are the work of Bathurst and Karpurapu (1993) and Rajagopal et al. (1999).

Using the theories presented by Bathurst and Karpurapu (1993) and Rajagopal et al. (1999), only the peak strength of granular soil confined in geocells can be predicted.

The aim of this section is to further develop the theories mentioned above in order to facilitate the understanding and modelling of the constitutive behaviour of geocell reinforced soil structures.

As mentioned before, a prerequisite for understanding and modelling the stress-strain behaviour of granular soil confined within a single geocell, is an understanding of the constitutive behaviour of the soil and the membrane material. The plastic volumetric and strain hardening behaviour of the soil is important and an appropriate constitutive model needs to be used. As the constitutive behaviour of the membranes is non-linear and strain-rate-dependent, it is equally important to use an appropriate membrane stress-strain curve. Sections 4.4 and 4.5.3 provide such models that will be used in this section to develop a calculation scheme for the stress-strain response of soil reinforced with a single geocell.

4.6.1 Implementation of the soil constitutive model into a calculation procedure

Vermeer and De Borst (1984) showed that, for a Coulomb type model with the intermediate principal strain, ε_2 = 0, the following relationship is applicable:

$$\sin(\psi) = \frac{\delta\varepsilon_v^p}{-2\delta\varepsilon_1^p + \delta\varepsilon_v^p} \tag{4.44}$$

Where:

ψ = the dilation angle of the material,

$\delta_{\varepsilon 1}{}^p$, $\delta_{\varepsilon v}{}^p$ = the plastic volumetric and plastic major principal strain rate.

Using this expression, it can easily be shown that:

$$\frac{\delta\varepsilon_v^p}{\delta\varepsilon_1^p} = \frac{2\cdot\sin(\psi)}{\sin(\psi)-1} \tag{4.45}$$

With the dilation angle, ψ, as a function of the plastic shear state, the rate of plastic volumetric strain with plastic major principal strain for an element of soil, can be obtained for any state of plasticity. It is thus possible to calculate the plastic volumetric strain increment of a soil element, $\Delta\varepsilon_v^p$, for an incremental increase in the plastic major principal strain, $\Delta\varepsilon_1^p$:

$$\Delta\varepsilon_v^p = \frac{2\cdot\sin(\psi)\cdot\Delta\varepsilon_1^p}{\sin(\psi)-1} \tag{4.46}$$

Where:

ψ = the dilation angle of the material,

$\Delta\varepsilon_1^p$, $\Delta\varepsilon_v^p$ = the plastic volumetric and plastic major principal strain increment.

As the Mohr-Coulomb friction angle is known for any plastic state when using the soil model presented in Section 4.4, the principal stress ratio, *R*, for the soil element can be obtained with:

$$R = \frac{1+\sin(\phi')}{1-\sin(\phi')} \tag{4.47}$$

Where:

ϕ' = the Mohr-Coulomb friction angle,

R = the principal stress ratio, $\frac{\sigma_1'}{\sigma_3'}$.

The elastic components of the major principal strain and the volumetric strain under triaxial conditions can be calculated, using the following equations obtained from linear elastic theory:

$$\varepsilon_1^e = \frac{\sigma_3'}{E}\cdot(R-1) \tag{4.48}$$

$$\varepsilon_v^e = \frac{(1-2\cdot\nu)\cdot\sigma_3'}{E}\cdot(R-1) \tag{4.49}$$

Where:

ε_1^e, ε_v^e = the elastic component of the major principal strain and the volumetric strain,

ν, E = the Poisson's ratio and Young's modulus of the soil,

σ'_3 = the minor principal stress,

R = the principal stress ratio.

The total major principal strain and volumetric strain for a soil element can therefore be obtained by summing the elastic and plastic components, i.e.:

$$\varepsilon_1 = \varepsilon_1^e + \varepsilon_1^p \tag{4.50}$$

$$\varepsilon_v = \varepsilon_v^e + \varepsilon_v^p \tag{4.51}$$

Where:

ε_1, ε_v = the total major principal strain and volumetric strain,

ε_v^e, ε_v^p = the elastic and plastic components of the volumetric strain,

ε_1^e, ε_1^p = the elastic and plastic components of the major principal strain.

The stresses and strains calculated with the equations presented above are applicable to a soil element. Due to the non-uniform stress and strain distribution in a cylinder of soil of which the ends are constrained, the stresses and strains calculated for a soil element is not the same for the soil cylinder.

Correction factors will be introduced here to enable one to obtain the cylinder axial strain and volumetric strain from the mean of the local strains throughout the soil cylinder.

4.6.2 Corrections for non-uniform strain

The quantification of the extent of the "dead zone"

Consider a triaxial test specimen tested with rough ends. Several researchers have shown (e.g. Deman, 1975; Alshibli et al., 2003) that a zone adjacent to each of the end platens exist, in which little strain occurs. These zones are sometimes referred to as "dead zones" and, for cylindrical specimens, have the shape of round nosed cones which form at an angle, β, to the direction of the

minor compressive stress (Figure 4.47). Due to the necessity for sophisticated techniques, the value of β is seldom recorded.

The β angle is an important parameter for estimating the size of the "dead zone" and needs to be estimated for different states of plastic shear in the soil. The author suggests that the angle, β, can be assumed equal to the angle of the mean shearing direction of the soil element, χ (Figure 4.47) which can be estimated by:

$$\beta = \chi = \frac{\phi'_{mob} + \psi_{mob}}{4} + 45° \tag{4.52}$$

Where:

ϕ'_{mob} = the mobilized Mohr-Coulomb friction angle,

ψ_{mob} = the mobilized dilation angle.

The mean shearing direction of a soil element is discussed in Appendix E.

When a rupture surface (shear band) develops in the soil, the direction of the shear band, θ, is equal to χ. Alshibli et al. (2003) used computed tomography[1] to study the internal structure of silty sand specimens under triaxial loading in a conventional triaxial testing apparatus. Figure 4.48 shows three of the images produced by Alshibli et al. (2003). These images are sections at the locations in the sample shown in the same figure. In Figure 4.48(a) and (b) the similarity of β and θ can be seen. Figure 4.48(c) is a section near the centre of the sample. Separate shear bands are not easily distinguishable in this section. As this section cuts the "dead zone" at a right angle, the angle between the horizontal and the boundary of the "dead zone" visible in the figure, is the true β angle.

Using Equation 4.52 and the peak values for ϕ' and ψ, from the data presented by Alshibli et al. (2003), β for the tested material under the stress conditions at which it was tested is about 66°. Lines showing the β angles of 66° are shown in Figure 4.48*c*. The peak values of the friction and dilation angles were used as the images in Figure 4.48 were produced for post peak strain conditions and the maximum inclination of the shear bands are obtained from the peak values of the two angles. The data of Alshibli et al. (2003) therefore supports the assumption that $\beta = \chi$, at least for the state after the development of shear bands.

[1] More detail on the method of Computed Tomography is given by Batiste et al. (2001)

It has been mentioned (Dresher and Vardoulakis, 1982) that the angle, β, increases with an increase in the strain of the sample. This is also implied by Equation (4.52) as β will increase from the early stages of plastic strain where lower values of ϕ'_{mob} and ψ_{mob} are applicable, to the peak stress state where the angles will be a maximum (Figure 4.49).

In order to estimate the volume of material in the "dead zones" an assumption on the geometry of the "dead zones" needs to be made.

The author suggests that the zone can be assumed to be a paraboloid. The depth of this zone from the confined ends can be obtained with the following equation, derived from the assumption of a paraboloidal zone: (Derivation given in Appendix A.)

$$d = \frac{Diam_0 \cdot \tan(\beta)}{4} \tag{4.53}$$

Where:

d = the maximum depth of the "dead zone" from the confined surface,

$Diam_0$ = the diameter of the soil cylinder at the confined ends,

β = the angle between the "dead zone" and the confined boundary, at the confined boundary.

Figure 4.48 and Figure 4.50 show the appropriate parabolas superimposed on images from Alshibli et al. (2003) and Deman (1975). Assuming the dead zone to be of a paraboloidal form seems to be acceptable.

Correction factors for axial and volumetric strain

By assuming the "dead zones" to be a paraboloid, it can be shown that the mean length of the plasticly deforming part of the soil specimen (Figure 4.51) can be written as:

$$l' = l - \frac{Diam_0}{4} \cdot \tan(\beta) \tag{4.54}$$

Where:

l' = the mean length of the plasticly deforming soil,

l = the length of the soil cylinder,

β = the angle between the "dead zone" and the confined

boundary, at the confined boundary.

This equation therefore provides a method for estimating the relationship between the mean local axial strain, $\bar{\varepsilon}_{al}$, and the axial strain of the whole sample, ε_{ag}, i.e.:

$$\varepsilon_{ag} = \bar{\varepsilon}_{al} \cdot \left(1 - \frac{Diam_0}{l_0 \cdot (1-\varepsilon_{ag})} \frac{\tan(\beta)}{4}\right) \tag{4.55}$$

Where:

l, l_0 = the current and original length of the soil cylinder,

β = the angle between the "dead zone" and the confined boundary, at the confined boundary.

The derivation of Equation (4.55) is provided in Appendix A. The simplifying assumption, that the soil within the "dead zones" do not undergo any volume change, enables one to derive the following relationship between the mean local volumetric strain, $\bar{\varepsilon}_{vl}$, and the volumetric strain measured for the whole sample, ε_{vg}: (The derivation of the equation is provided in Appendix A.)

$$\varepsilon_{vg} = \bar{\varepsilon}_{vl} \cdot \left(1 - \frac{Diam_0}{l_0 \cdot (1-\varepsilon_{vg})} \frac{\tan(\beta)}{4}\right) \tag{4.56}$$

Where:

l, l_0 = the current and original length of the soil cylinder,

β = the angle between the "dead zone" and the confined boundary, at the confined boundary.

4.6.3 Calculation of the stress state in the soil

If the confining stress on a soil element is known, the major principal stress can be calculated using Equation (4.47). It is therefore necessary to estimate the component of the confining stress resulting from the membrane action. Frost and Yang (2003) mentioned that the middle part of a soil cylinder with an aspect ratio of 2, is less affected by the end constraints and is able to deform more freely. They also pointed out that the middle part of the soil specimen governs the behaviour of the soil specimen. It is therefore assumed that the strength of the cylinder can be estimated by considering the confining stress over the middle half of the cylinder. As the membrane stress is dependent on the radial strain of the soil cylinder, the major principal stress in the centre half of the

cylinder can only be estimated if the diameter of the soil in this section of the soil cylinder is known.

Following the recommendation made by Bishop and Henkel (1957) a triaxial test specimen is often assumed to deform as a right cylinder. The diameter of the right cylinder can then be obtained through the following equation:

$$D_c = Diam_0 \cdot \sqrt{\frac{1-\varepsilon_v}{1-\varepsilon_a}} \tag{4.57}$$

Where:

D_c, $Diam_0$ = the diameter at the centre of the soil cylinder and the original diameter of the soil cylinder,

ε_a, ε_v = the total axial and volumetric strain of the soil cylinder.

If the soil cylinder deforms uniformly this equation will be accurate. For soil cylinders tested with rough end platens, the equation underestimates the area of the sample in the centre half of the soil cylinder and therefore the radial strain in this area (Figure 4.52).

As an alternative to the above-mentioned assumption, Roscoe et al. (1959) suggested that the bulging profile of the soil cylinder with an aspect ratio of 2, under triaxial compression loading, may be approximated as being parabolic. Assuming a parabolic deformation shape, the following equation for the centre diameter can be derived: (Derivation provided in Appendix A.)

$$D_c = 2 \cdot \sqrt{\frac{5}{16} \cdot \left(\frac{6}{\pi} \cdot \frac{V_0 \cdot (1-\varepsilon_{vg})}{l_0 \cdot (1-\varepsilon_{ag})} - \left(\frac{Diam_0}{2} \right)^2 \right)} - \frac{Diam_0}{8} \tag{4.58}$$

Where:

D_c = the diameter at the centre of the soil cylinder,

V_0, l_0, $Diam_0$ = the original volume, length and diameter of the soil cylinder,

ε_{ag}, ε_{vg} = the axial and volumetric strain measured for the whole soil cylinder.

Figure 4.53 compares the horizontal sectional area at the centre of a triaxial test sample modelled with FLAC3D using the constitutive soil model presented in Section 4.4 and the area calculated with the analytical scheme presented in Section 4.6.4 using Equation (4.58). The close correlation between the two

analyses suggests that the assumption of a parabolic deformation under triaxial loading conditions is reasonable.

Also shown in the figure is the area change implicitly assumed by Henkel and Gilbert's (1952) for their "hoop stress" correction for undrained tests. The approach followed by Henkel and Gilbert underestimates the area at the centre of the sample.

This assumption also seems reasonable for a soil cylinder confined within a membrane if the confining stress resulting from the membrane action is small compared to the ambient confining stress.

However, under conditions where the ambient confining stress is small, the membrane has a greater influence on the deformation mode. The membrane stress increases as the strain in the membrane increases. After a small axial deformation, the confining stress due to the membrane action at the centre section of the soil cylinder will be larger than that at the top and bottom of the cylinder. As a result of this stress difference, the soil deformation at the centre of the sample will be restricted more than that closer to the ends. This concept is illustrated in (Figure 4.54).

Comparison between the numerical and analytical solutions to the problem lead to the derivation of the following equation for the centre diameter of the soil cylinder under non-uniform confining stress resulting from membrane action:

$$D_c = \frac{1}{8} \cdot \left(\sqrt{\frac{384}{\pi} \cdot \frac{V_0 \cdot (1 - \varepsilon_{vg})}{l_0 \cdot (1 - \varepsilon_{ag})} - 15 \cdot Diam_0} - Diam_0 \right) \tag{4.59}$$

Where:

D_c = the diameter at the centre of the soil cylinder,

V_0, l_0, $Diam_0$ = the original volume, length and diameter of the soil cylinder,

ε_{ag}, ε_{vg} = the axial and volumetric strain measured for the whole soil cylinder.

This equation is derived for a simplified deformed shape consisting of a cylindrical and two conical sections as shown in Figure 4.55 and the derivation is given in Appendix A.

Figure 4.56 compares the change in the horizontal cross sectional area of the soil cylinder with axial strain obtained from the measurements of the radial

strain to the area calculated with Equation (4.59). The close agreement between the results indicates that Equation (4.59) adequately approximates the central area of the soil cylinder. It seems that only after the complete development of shear bands in the soil does the measured data deviate significantly from the theory. Also shown in the figure is the area calculated by following the approach suggested by Henkel and Gilbert (1952), and the theoretical equivalent horizontal cross section area for slip deformation on a shear band.

From the diameter of the soil cylinder, the membrane strain, which is equal to the radial strain, can be obtained from:

$$\varepsilon_{mh} = \frac{D_h - Diam_0}{Diam_0} \tag{4.60}$$

Where:

D_h = the diameter of the soil cylinder at position *h,*

$Diam_0$ = the original diameter of the soil cylinder,

ε_{mh} = the hoop strain in the membrane at position *h.*

The confining stress imposed onto the soil can be calculated as follows:

$$\sigma'_{3h} = \sigma'_{30} + \sigma_m(\varepsilon_{mh}) \cdot \frac{2 \cdot t}{D_h} \cdot f_s \tag{4.61}$$

with:

$$f_s = \frac{1 - \varepsilon_{mh} \cdot \nu_m}{1 - \varepsilon_a}$$

Where:

σ'_{3h} = the confining stress imposed onto the soil at position *h*,

σ'_{30} = the ambient confining stress,

σ_m = the membrane stress,

ε_{mh} = the hoop strain in the membrane at position *h*,

t = the thickness of the membrane,

D_h = the diameter of the soil cylinder at position *h*,

ε_a = the mean axial strain of the soil cylinder,

ν_m = the Poisson's ratio of the membrane.

This equation consists of the sum of the ambient confining stress and the confining stress resulting from the membrane action. The multiplication of the membrane confining stress term with the factor, f_s, is necessary to account for

the shortening of the cylinder under compression and the shortening of the membrane in the long axis of the cylinder due to the Poisson's ratio of the membrane. The derivation of the confining stress resulting from the membrane action is given in Appendix A.

The membrane strain and subsequent membrane stress at any point in the membrane, other than at the centre of the cylinder, will be less than the value at the centre of the cylinder. It therefore follows that the mean membrane confining stress over the centre half of the cylinder will be less than the value at the centre of the cylinder.

If a linear elastic membrane confines the soil, the mean membrane confining stress can be obtained by calculating a mean membrane strain over the centre half of the cylinder. For this purpose, one can assume a parabolic deformation, resulting in the following equation of which the derivation is provided in Appendix A:

$$\overline{D}_m = \frac{4}{48} \cdot \left(\frac{Diam_0}{D_c} + 11 \right) \cdot D_c \qquad (4.62)$$

Where:

$\overline{D}_m$ = the mean diameter of the centre half of the soil cylinder,

D_c = the diameter at the centre of the soil cylinder,

$Diam_0$ = the original diameter of the soil cylinder.

The mean membrane strain over the centre half of the cylinder can thus be obtained from Equation (4.60) and the confining stress obtained by using Equation (4.61) by substituting D_h for $\overline{D}_m$.

For a membrane with a non-linear stress-strain response, this approach is not acceptable. The mean confining membrane stress needs to be obtained through integration of the membrane confining stress over the centre half of the cylinder. This can be achieved by utilizing Simpson's numerical integration rule. For this purpose, the deformation mode of the soil cylinder can be assumed to be parabolic, resulting in the following equation for the diameter of the cylinder at the top and bottom of the centre half of the cylinder (Figure 4.57):

$$D_{\frac{L}{4}} = \frac{3D_c + Diam_0}{4} \qquad (4.63)$$

Where:

$\overline{D}_{\frac{l}{4}}$ = the diameter of the soil cylinder at position ¼*l* from the ends,

l = the length of the soil cylinder,

D_c = the diameter at the centre of the soil cylinder,

$Diam_0$ = the original diameter of the soil cylinder.

The acceptability of this approach is illustrated by the close agreement between the measured and calculated section areas at ¾-height of the soil sample shown in Figure 4.56.

An estimate of the membrane strain at the top and bottom of the centre half of the cylinder, $\varepsilon_{m\frac{l}{4}}$, can therefore be obtained. Using Equation (4.61) the membrane confining stress at the centre, σ_{3c}, and at quarter height, $\sigma_{3\frac{l}{4}}$ can be obtained and the mean membrane confining stress over the centre half of the cylinder $\overline{\sigma}_{3m}$ can be estimated with the following equation obtained by applying Simpson's rule:

$$\overline{\sigma}_m = \frac{1}{3}\cdot\left(2\cdot\sigma_c + \sigma_{\frac{l}{4}}\right) \tag{4.64}$$

Where:

$\overline{\sigma}_m$ = the mean membrane hoop stress over the centre half of the soil cylinder,

$\sigma_c, \sigma_{3\frac{l}{4}}$ = the membrane hoop stress at the centre of the soil cylinder and at the at position ¼*l* from the ends,

l = the length of the soil cylinder.

The theory of the stress-strain behaviour of sand reinforced with a single geocell presented here, can be compiled into a calculation procedure to obtain the full stress-strain curve for the single cell geocell system. The theoretical discussion in this section and the calculation procedure presented in Section 4.6.4 is not applicable when a shear band develop in the soil.

The mechanism by which a single geocell-soil composite generates resistance after a shear band has developed, is substantially different to the mechanism applicable before the development of such a shear band. After the peak state of the soil has been reached, both bulging and slip deformation of the geocell structure have been observed. The bulging deformation increases the cross

sectional area of the structure and therefore increases the engineering stress while the slip deformation reduces the contact area and therefore reduces the engineering stress. The development of the shear band localizes the shear strain, resulting in an increased rate of deformation within the shear band and a subsequent increased rate of strain softening. Because of the change in the deformation mode, the horizontal strain rate reduces, which has the effect of reducing the rate at which the membrane generated confining stress increase. Added to these complexities is the development of diagonal tension zones in the membrane that would tend to increase the resistance of the composite structure (Figure 4.58).

4.6.4 Calculation procedure

Figure 4.59 shows a flow chart outlining a calculation procedure for the stress-strain response of sand reinforced with a single geocell. The presented calculation procedure, combines the components discussed above.

The different sections in the flow chart can be explained as follows:

1. Define the appropriate functions for ϕ', ψ and σ_m as described in Sections 4.4 and 4.5.3.
2. Initialise the parameters for the stepwise calculation.
3. Calculate the plastic axial strain, ε_a^p, and the corresponding plastic volumetric strain, ε_v^p. The dilation angle, ψ, is used in the calculation of ε_v^p but is, however, a function of both ε_a^p and ε_v^p. In the iterative analytical solution presented in Figure 4.59, the value of ψ, for the previous calculation step is used to calculate a value for the plastic volumetric strain, which is used to calculate the plastic shear strain parameter, ε_s^p. The calculated plastic shear strain is then used to update the value of ψ and, using the updated value of ψ, the value of ε_v^p for the particular iteration is calculated. The difference between the initial and updated values of ψ and ε_v^p for each calculation step is small for small values of $\Delta\varepsilon_a^p$. This calculation step uses Equation (4.46).
4. Having calculated the plastic shear strain parameter, the appropriate strength parameters for the soil corresponding to a particular plastic state can be calculated. This calculation step uses Equation (4.47).

5. The elastic strain components for each stress state can be calculated. In these calculations, the confining stress calculated for the previous iteration is used. This calculation step uses Equation (4.48) to (4.51).

6. The value of β and the factors for obtaining the global strain values from the local strain values can be calculated. This calculation step uses Equation (4.52), (4.55) and (4.56).

7. The global volumetric and axial strain of the whole soil cylinder is calculated from the mean local strain values and the correction factors obtained in the previous step.

8. Using the appropriate equation applicable to the deformation mode of the soil cylinder, the membrane strain and resulting confining stress can then be calculated. Depending on the conditions analysed, the calculation step uses one of Equation (4.58) or (4.59) to calculate the centre diameter of the soil cylinder. Equation (4.60) is used to calculate the hoop strain of the membrane and Equation (4.61) to calculate the confining stress resulting from the membrane. The mean confining stress in the centre half of the soil cylinder is then calculated.

9. This step calculates the major principal stress in the soil cylinder.

4.6.5 Verification of the proposed calculational scheme

The presented calculation scheme is applicable to granular soil confined with a single geocell, of which a triaxial compression test is a special case. It is therefore possible to verify the calculational procedure against conventional triaxial test data.

Figure 4.60 compares the stress-strain curves for the soil calculated with numerical analyses software and the analytical procedure presented in Section 4.6.4. The numerical analyses were performed with the finite difference code FLAC3D. For the purpose of comparing the material response predicted by the two methods a uniform strain distribution was assumed in the analytical procedure, that is, $\varepsilon_{vg} = \varepsilon_{vl}$ and $\varepsilon_{ag} = \varepsilon_{al}$.

The conventional triaxial tests can be modelled with both the numerical and analytical methods. In the numerical analyses the ends of the sample were constrained against horizontal movement. In the analytical procedure non-uniform deformation was assumed and Equations (4.3) and (4.41) were used to estimate the sample volumetric and axial strain.

Figure 4.61 compares the stress-strain curves obtained with the analytical and numerical methods and the measured data for a drained triaxial compression test on a dense classified tailings sample with a confining stress of 175 kPa.

The area at the centre of the sample was not measured in the triaxial test. However, as shown previously in Figure 4.53, the calculated areas obtained from the numerical method and the analytical methods, using Equation (4.58) compare well.

A good correlation between the results from the numerical and analytical procedures is obtained under other conditions as well. Figure 4.62 compares the stress-strain response of the triaxial test modelled previously with a geocell membrane, having a linear stress-strain behaviour, added to the soil cylinder. The membrane thickness was assumed to be 0.18 mm and the membrane stiffness was assumed to be 59 MPa.

If, however, the ambient confining stress is lowered to 10 kPa the deformation profile of the soil cylinder changes as discussed in the previous section. For this analysis the diameter at the centre of the soil cylinder was calculated with Equation (4.59). Figure 4.63 shows the calculated stress-strain response for this scenario.

The difference in the stress-strain curves after ε_{ag} = 0.08 is a direct result of the difference in the predicted cross sectional area (Figure 4.64). Refinement of the analytical estimation of the deformation shape and the cross sectional area, will result in a better fit at larger strains.

Repeating the analysis with a non-linear stress-strain response for the geocell membrane produces the results shown in Figure 4.65 and Figure 4.66. The membrane behaviour discussed in Section 4.5.3 was used in this analysis.

4.6.6 Comparison with laboratory tests on soil reinforced with a single geocell

From the measured radial strain and numerical analysis it seems that the strain rate of the membrane at the centre of the geocell is about 10% higher than the axial strain of the geocell. The strain rate of the membrane was therefore assumed to be 5.7 %/min. The parameters for the membrane model applicable to the specified strain rate is shown in Table 4.5. The original thickness of the membranes were assumed to be equal to the mean measured thickness of

0.18 mm. A nominal membrane strain at the start of the test was assumed to be 0.003, resulting in a long term confining stress of about 1.5 kPa.

Table 4.5 Parameters for plastic models for applicable strain rate for single geocell tests.

Hyperbolic model			Exponential model		
β	σ_t	ε_t	a	c	b
0.248	9.97	0.16	16.06	7.52	32.517

In Section 4.3 the relationships between the soil density, mean principal stress and the soil strength and stiffness parameters were discussed. From these relationships the parameters applicable to the soil in the single geocell tests can be obtained. Table 4.6 summarizes the soil parameters applicable to the three single geocell tests.

Table 4.6 Soil parameters for the single geocell tests.

Test	Elastic parameters		Stress-dilation parameters					Work-hardening parameters		
	κ	ν	ϕ'_μ (°)	ϕ'_{cv} (°)	ϕ' (°)	D_{min}	D_{max}	b	$(\varepsilon_s^p)_{peak}$	$(\varepsilon_s^p)_{cv}$
A					42.6		1.598		0.066	
B	5.82×10^3	0.23	29.4	34.38	42.7	0.446	1.616	-12	0.062	0.45
C					42.8		1.625		0.060	

Using the parameters presented in Table 4.5 and Table 4.6 and the calculation procedure presented in Section 4.6.4 the theoretical stress-strain response for the tested single geocell structures were calculated. The results of these calculations are compared with the measured stress-strain response in Figure 4.67.

Both the measured and calculated curves show stiffening at the initial stages of deformation. The initial stiffening for the theoretical curves however takes place at a slower rate than for the measured curves. This may be attributed to an overestimation of the amount of plastic collapse taking place in the soil due to a small amount of plastic collapse taking place before commencement of the test due to handling of the specimen or an overestimation of the plastic collapse by the soil model.

A good correlation exists between the measured and theoretical curve up to the peak strength of the single geocell composite structure after which the engineering stress predicted by the theory increases while the measured value remains fairly constant. This is a result of the development of a shear band in the single geocell system, which is not taken into account by the theory.

It is interesting to note that the peak strength of the composite structure is reached after the soil reaches its peak mobilized friction and dilation. This results from the increase in the confining stress due to the increase in the membrane stress upon further shearing.

During the tests it was noted that the bulging deformation of the specimen continued even after the initial development of the shear band and it seems that the membrane, due to its resistance against the shearing along the shear "plane", to some extent, slows down the development of the shear band.

This explains the good correlation between the theoretical curve and the measured data between the stage at which the soil reaches its peak state and the stage at which the composite structure reaches its peak strength. Further support for the interpretation is obtained from calculated and measured projected areas shown in Figure 4.56. From this figure it can be seen that after reaching the peak state in the soil the specimen follows the "bulging" behaviour before gradually reducing towards the slip behaviour.

4.7 The stress-strain behaviour of soil reinforced with a multiple cell geocell structure

As with the single cell structure, the "dead zone" at the ends of the packs has an important influence on the strain distribution within the pack and the subsequent stress-strain results.

Using the measured data of the profile of the "dead zone" presented in Chapter 3, the three dimensional "dead zone" profile shown in Figure 4.68 was reconstructed. The "dead zone" profile for the "square" geocell packs seems to be similar to the paraboloidal "dead zone" profile applicable to circular single cell specimens.

Figure 4.69 shows the peak β angle of 59° superimposed on the section profiles reconstructed from the measured data. This β angle was calculated using the

equation presented in Section 4.6.2. This equation is repeated here for convenience:

$$\beta = \frac{\phi'_{mob} + \psi_{mob}}{4} + 45° \tag{4.52}$$

Where:

ϕ'_{mob} = the mobilized Mohr-Coulomb friction angle,

ψ_{mob} = the mobilized dilation angle.

In Section 4.6.2 it was also proposed that the "dead zone" for a cylindrical specimen can be assumed to be a paraboloid. Along all three symmetrical axes of the "square" packs, the assumption of a parabolic "dead zone" profile seems acceptable (Figure 4.69). The profile of the "dead zone" along the diagonal in Figure 4.69 is also normalized with respect to the width, W. The depth of the "dead zone" can therefore be calculated using Equation (4.53) presented in Section 4.6.2 and repeated here for convenience sake:

$$d = \frac{W_0 \cdot \tan(\beta)}{4} \tag{4.53}$$

Where:

d = the maximum depth of the "dead zone" from the confined surface,

W_0 = the width of the geocell pack at the confined ends,

β = the angle between the "dead zone" and the confined boundary, at the confined boundary.

As shown in Figure 4.69, Equation (4.53) provides a good estimate for the depth of the "dead zone".

As a direct result of the shape of the "dead zone", larger horizontal strains are expected closer to the centre of the pack and lower strains closer to the sides of the packs.

From the measured deformation of the 3x3 and 7x7 cell pack presented in Chapter 3 it can be seen that the horizontal strain in the centre cell at the mid-height, far exceeds the horizontal strain of the outer cells at larger strains. For the 7x7 cell pack the horizontal strain of the outer cells seem to cease at a vertical strain of about 0.08 while the horizontal strain in the centre cell continues with the vertical straining of the pack. The horizontal strain in each cell closer to the centre of the pack exceeds the strain in the cells directly on its

outside. The results of the measurements are consistent with observations made during the compression tests and the permanent deformation profile after completion of the tests.

Using the measurements of the LVDT's and assuming symmetry the cumulative horizontal strain distribution in the packs can be reconstructed at different axial strain levels (Figure 4.70). The fitted relationships shown in Figure 4.70(a) were differentiated to give the curves for the horizontal strain distribution shown in Figure 4.70(b). From Figure 4.70(a) it can be seen that there is little difference between the data obtained from the 2x2, 3x3 and 7x7 cell packs.

It seems that the number of cells in the packs does not significantly influence the horizontal strain distribution in the packs, at least for the thin membrane structures used in this study. This is also shown by the close correlation of the total horizontal strain at the mid-height of the multi cell packs presented in Figure 4.71.

Also shown in Figure 4.71 is the total horizontal strain for the single cell geocell structure. The horizontal strain at the mid-height of the single cell structure is about 20% lower than that measured for the multi cell packs. This difference can be attributed to the fact that the multi cell packs have "square" horizontal cross section shapes, compared to the circular shape of the single cell structure. Where straining in the circular structure is axisymmetric, this is not the case for the "square" packs. The cross section shape of the packs increasingly deviate from the original "square" shape towards a more circular shape with increased axial strain. As shown by the measurements of deformation on the 7x7 cell pack, the strain rate at the middle of the pack sides is about 13-16% higher than the strain rate along the diagonals of the pack.

The strain rate and strain magnitude of the membranes is the highest in the centre cell and the lowest in the outer cells. The stress in the membranes of the inner cells will therefore be higher than the stress in the membranes of the outer cells. The stress in the outermost membranes will be the lowest.

The stress in the membrane is transferred to the soil through a "hoop stress" effect and is therefore dependent on the curvature of the membrane. The lower the curvature of the membrane, the lower the stress in the soil resulting from a particular stress in the membrane. The stress transfer from the membranes to the soil is therefore less efficient for the originally planar inner membranes. One would expect the membrane/soil stress transfer to be the least efficient for the

innermost membranes. The absolute value of stress increase in a cell will be a result of the strain, strain rate, and membrane curvature.

The absolute confining stress in each cell results from its membrane "hoop stress" as well as the superposition of the stresses due to all the membranes on its outside.

The stress-strain response of the 1, 2x2 and 3x3 cell packs shows a sudden stress drop. This is a result of strain localization. In the single cell structure, the strain localization results in the formation of a shear band. A shear band also developed in the 2x2 cell pack but, the inner membranes prevented the pack from failing in a shear mode. No visible shear band developed in the 3x3 pack test but the stress drop in the stress-strain curve suggest that strain localization did occur. From the 7x7 cell pack stress-strain response, no stress drop occurred, suggesting that the increased number of membranes were adequate to prevent a shear band from developing.

The confining stress in the soil resulting from a cell membrane is dependent on the curvature of the cell membrane and therefore also dependent on the cell size. From the theoretical formulation of the confining stress resulting from the membrane "hoop stress" presented by Henkel and Gilbert (1952) as well as the theoretical formulation presented in Section 4.6, it can be shown that the confining stress resulting from the "hoop stress" action on a cylindrical specimen is directly proportional to the inverse of the cell diameter. The measured and theoretical stress-strain response for the single cell tests presented in Figure 4.67 are shown in Figure 4.72, normalized with respect to the original cell diameter.

Normalization of the stress in the packs with respect to the original cell diameter provides a means for direct comparison of the data obtained for the multi-cell packs. Figure 4.73 shows the normalized stress-strain curves for the single cell and multi-cell packs. The results show a systematic change in both the magnitude and shape of the stress-strain curve, with an increase in the number of cells in the pack. At axial strains of less than about 0.015, a systematic increase in the stiffness of the packs with an increase in the number of cells can be seen. At higher strains, the pack stiffness and strength decrease with an increase in the cell number.

The systematic change in the peak strength of the pack with a change in the number of cells is shown in Figure 4.74(a). The results in the figure are shown

in terms of an efficiency factor at the peak stress of the multi-cell pack, $(f_{eff})_{peak}$ The efficiency factor, f_{eff}, is defined as follows:

$$f_{eff} = \frac{\sigma_{a\,\text{single cell}}}{\sigma_{a\,\text{multi-cell}}} \tag{4.65}$$

Where:

f_{eff} = the efficiency factor,

$\sigma_{a\ single}$ = the axial stress in a single cell structure at a specified diameter and axial strain rate,

$\sigma_{a\ multi\text{-}cell}$ = the axial stress in a multi-cell structure at the same specified cell diameter and axial strain rate.

The efficiency factor can be obtained experimentally by performing single cell and multi-cell tests at the same density and strain rates. The necessary single cell tests were not performed as part of this study and the appropriate single cell stress-strain curves were calculated using the theoretical procedure presented in Section 4.6.

For the tested packs the efficiency of the geocell packs decreases with an increase in the number of cells. Assuming the peak stress of the single cell structure to be correctly predicted by the theory, the data presented in Figure 4.74(a) shows that the peak stress in the 7x7 cell pack will be overestimated by about 40% by the single cell theory.

This seems to be in complete disagreement with the work of Rajagopal et al. (1999) who concluded that the "hoop stress" theory presented by Henkel and Gilbert (1952) can be used to estimate the peak stress of both single and multi-cell structures. As shown in Chapter 2 the tested configurations used by Rajagopal et al. (1999) was biased towards their conclusion as the interaction of the separate cells in their tests were limited. Due consideration was neither given to the influence of the cell diameters on the strength of the composite structures. Re-evaluation of the data presented by Rajagopal et al. (1999) produced the results shown in Figure 4.74(b) which are compared to the results of this study in Figure 4.74(c).

To enable the comparison of the data obtained from different geometries, the data are plotted against the "periphery factor" which is defined as follows:

$$f_{periphery} = No_{cp} \cdot f_{mp} \tag{4.66}$$

Where:

$f_{periphery}$ = the periphery factor,

No_{cp} = the number of cells on the periphery of the pack,

f_{mp} = the fraction of membranes belonging to only one cell.

The number of cell on the periphery of the 3x3 cell pack, for example, is 8 (No_{cp}=8) and half of the membranes belong to only one cell (f_{mp}=0.5), leading to a periphery factor of 4. For the 7x7 cell pack No_{cp}=24 and f_{mp}=0.25.

It can be seen that the inner membranes in the tests performed by Rajagopal et al. (1999) are curved into the centre cell at the start of compression. These membranes will therefore be unproductive. Using only the productive membranes to calculate the "periphery factor" leads to a better fit between the data obtained in this study and the data from Rajagopal et al. (1999) (Figure 4.74(c)).

The following empirical relationship can be fitted to the data:

$$(f_{eff})_{peak} = 1 - a_f \cdot \ln(f_{periphery}) \quad (4.67)$$

Where:

$(f_{eff})_{peak}$ = the efficiency factor at peak stress,

a_f = the parameter defining the rate of efficiency loss with an increase in the number of cells in the pack,

$f_{periphery}$ = the periphery factor of the pack.

The curve shown in Figure 4.74(c) is fitted to the data obtained in this study and has an a_f of 0.204. The value of a_f obtained from the data from Rajagopal et al. (1999) is 0.213. Using both the data from this study and the data from Rajagopal et al. (1999) a value of 0.207 for a_f was obtained.

The secondary x-axis in Figure 4.74(c) shows the cell geometry of the packs used in this study. Due to the non-linear relationship between the pack geometry and $f_{periphery}$, only a limited extrapolation is necessary for packs consisting of more cells than were tested in the laboratory. For a square pack a value of $f_{periphery} = 8$ correponds to a 10 000x10 000 cell configuration and can be regarded as the absolute maximum.

Comparison of the theoretical stress for the single cell configuration, and the tested single and multi-cell configuration are shown in Figure 4.75. The slight

underprediction by the theoretical formulation of the stress in the single cell structures and the increased stiffness of the multi-cell packs with an increase in the number of cells in the packs, during the early stages of compression can be seen in this figure.

Also evident in Figure 4.75 is the fact that the stress in the multi-cell packs tend towards a constant fraction of that predicted for continuum single cell behaviour. For the 2x2 and 3x3 cell tests this continuum response is preceded by a stage where a slight drop in the measured stress due to strain localization occurs. The effect of the strain localization, visible in the results of the single, 2x2 and 3x3 cell packs, is absent in the 7x7 cell pack.

The efficiency factor defined previously can be evaluated at different strains. Figure 4.76 shows the efficiency factor for different configurations at axial strain levels of 0.003, axial strain at peak stress and at axial strain levels of 0.12.

From the graph in Figure 4.76, the increase in f_{eff} at small strains and the decrease at larger strains can be seen. The f_{eff} increases monotonically with an increase in the number of cells at small strains and decrease monotonically with an increase in the number of cells at larger strains.

Taking a $f_{periphery} = 8$ as the absolute maximum and extrapolating the data to this value, the absolute maximum value for f_{eff} at a axial strain of 0.003 is of the order of 3.78. In similar vein, the absolute minimum values for f_{eff} at the peak and strain of 0.12 are of the order of 0.58 and 0.5 respectively.

A value of 7 may be regarded as a practical maximum value of $f_{periphery}$. This corresponds to a square pack configuration of 15x15 cells. For such a pack configuration, the values of f_{eff} at an axial strain of 0.003, at peak and at an axial strain of 0.12, are 3, 0.6, 0.52 respectively.

The work presented in this thesis can be used to estimate the expected stiffness and strength of geocell support packs with an aspect ratio of 0.5 in the following manner:

- Estimate the stress-strain curve for the fill material, confined with a single geocell, strained at a strain rate equivalent to that expected in the field. This can be achieved by using the analytical solution presented in Section 4.6 and can be confirmed with single cell tests which can easily be performed. The parameters of the suggested soil model can be

obtained from triaxial testing and the parameters for the HDPE membrane model can be obtained from uniaxial tensile testing.

- Estimate the efficiency factor for the field pack configuration at different strain levels. The efficiency factor at an axial strain of 0.003, at the peak and at an axial strain of 0.12 can be obtained from Figure 4.76 and will suffice for design purposes.
- These efficiency factors can then be used to obtain a design stress-strain curve for the support pack.

With further research, this design procedure can be extended to incorporate other aspects like the aspect ratio, membrane damage and temperature effects that influence the strength and stiffness of the geocell support pack which have been excluded from the scope of this research.

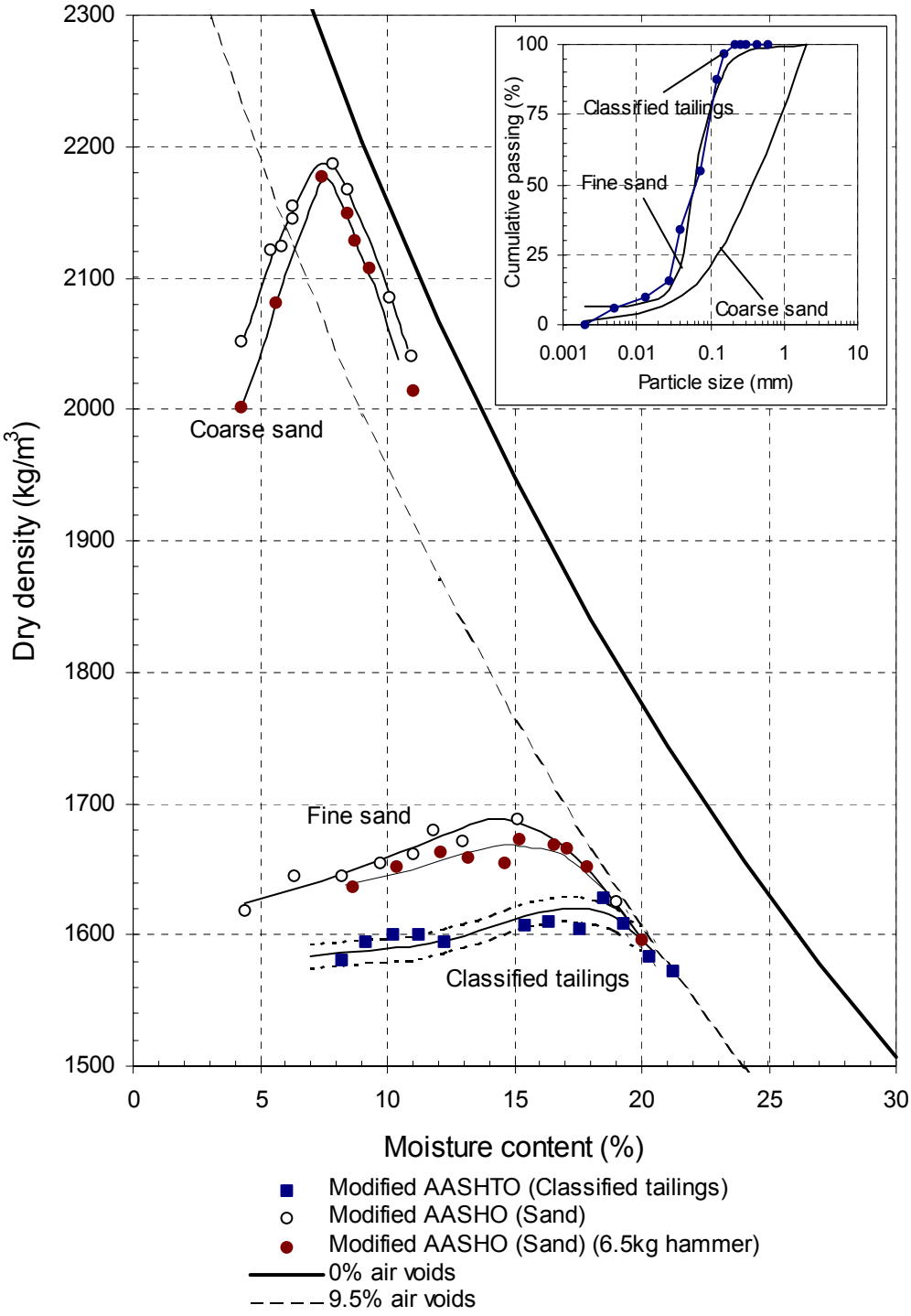

Data for the coarse and fine sand obtained from Road Research Laboratory (1952)

Figure 4.1 Comparison between the dry density/ moisture content curves for classified tailings and coarse and fine sand.

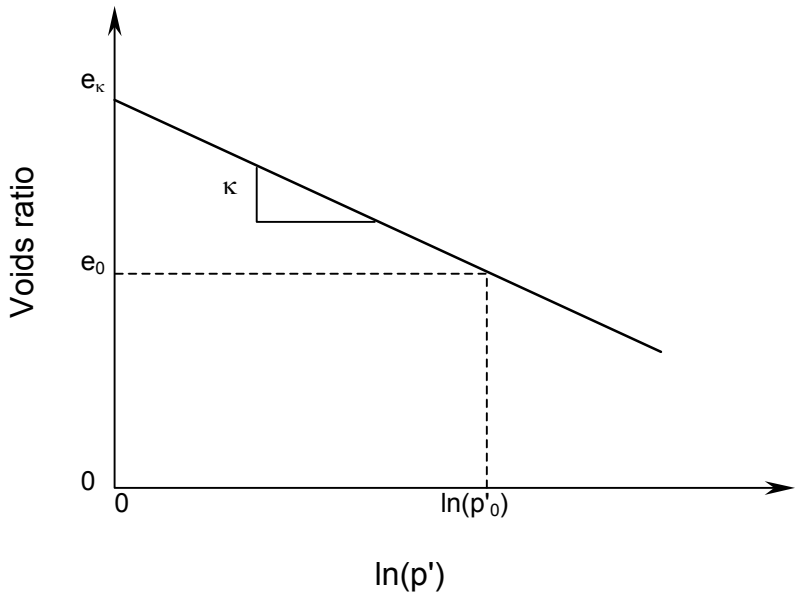

Figure 4.2 *The proposed elastic model for the classified tailings.*

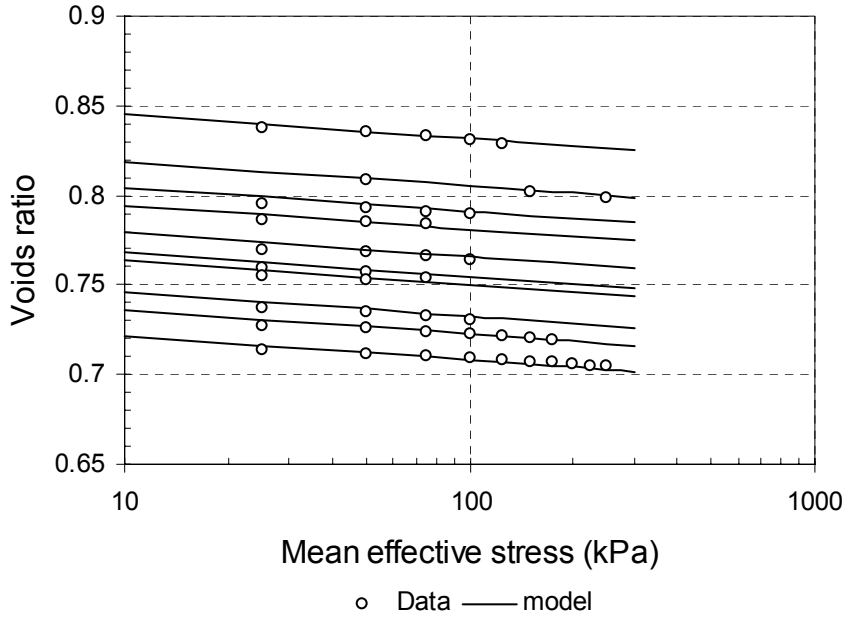

Figure 4.3 *Comparison between the isotropic compression test data and the fitted elastic model for the classified tailings.*

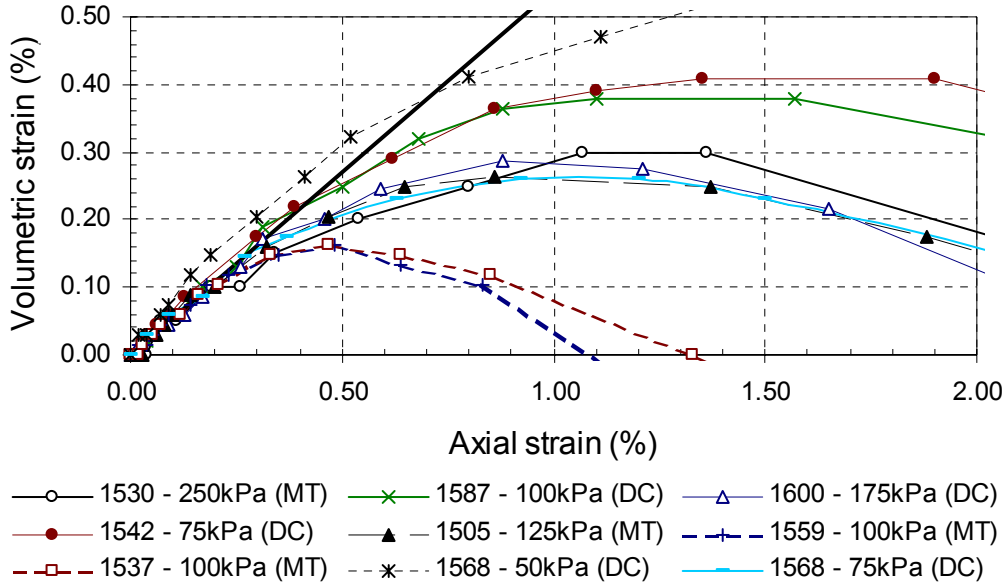

Figure 4.4 *The volumetric strain behaviour of the classified tailings at the early stages of shearing.*

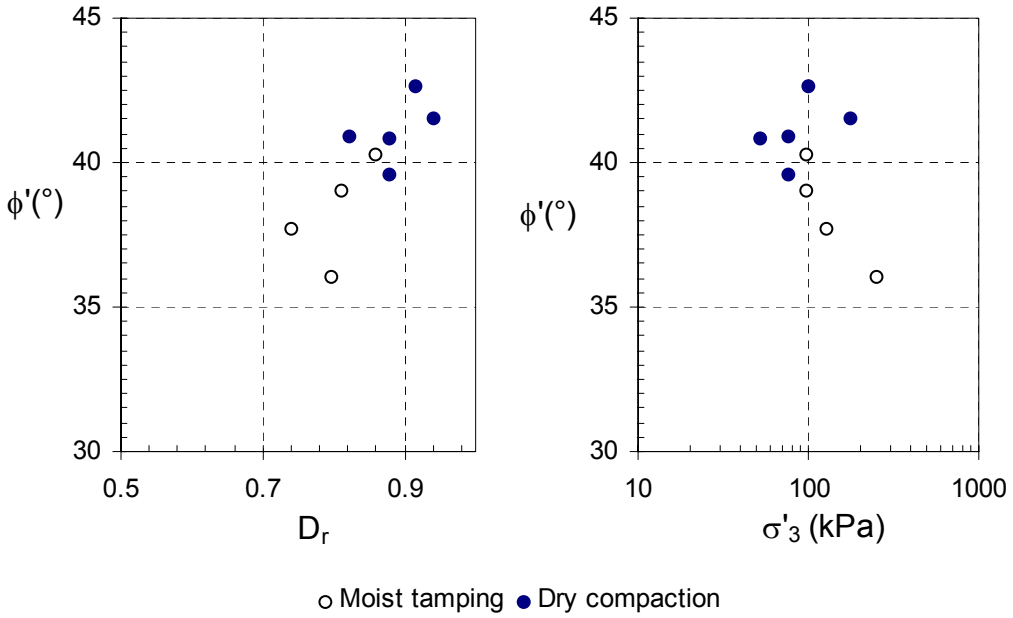

Figure 4.5 *The ϕ' as a function of relative density, D_r and confining stress, σ'_3.*

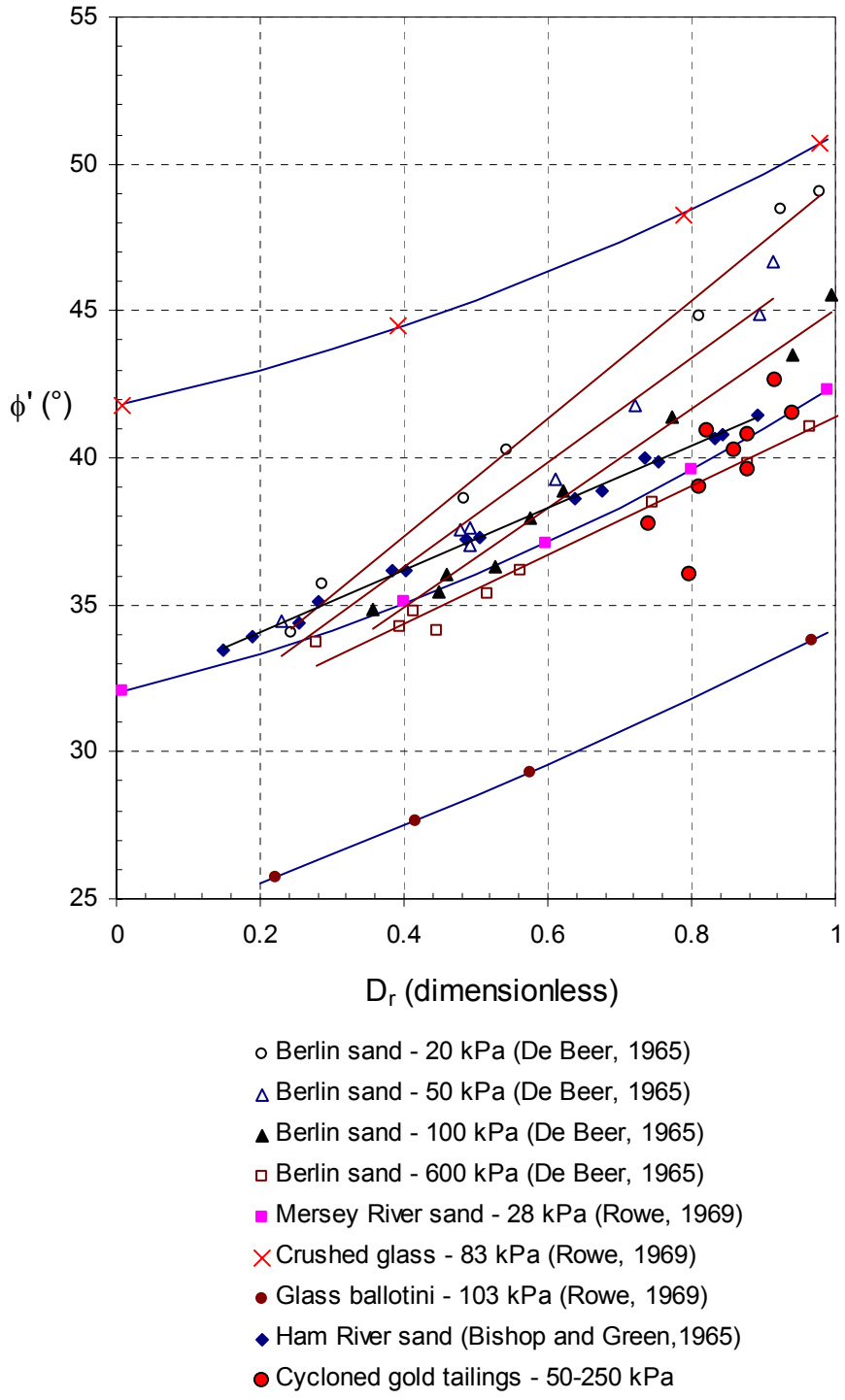

Figure 4.6 *The general trend for the change in ϕ' with change in D_r for test data presented in literature.*

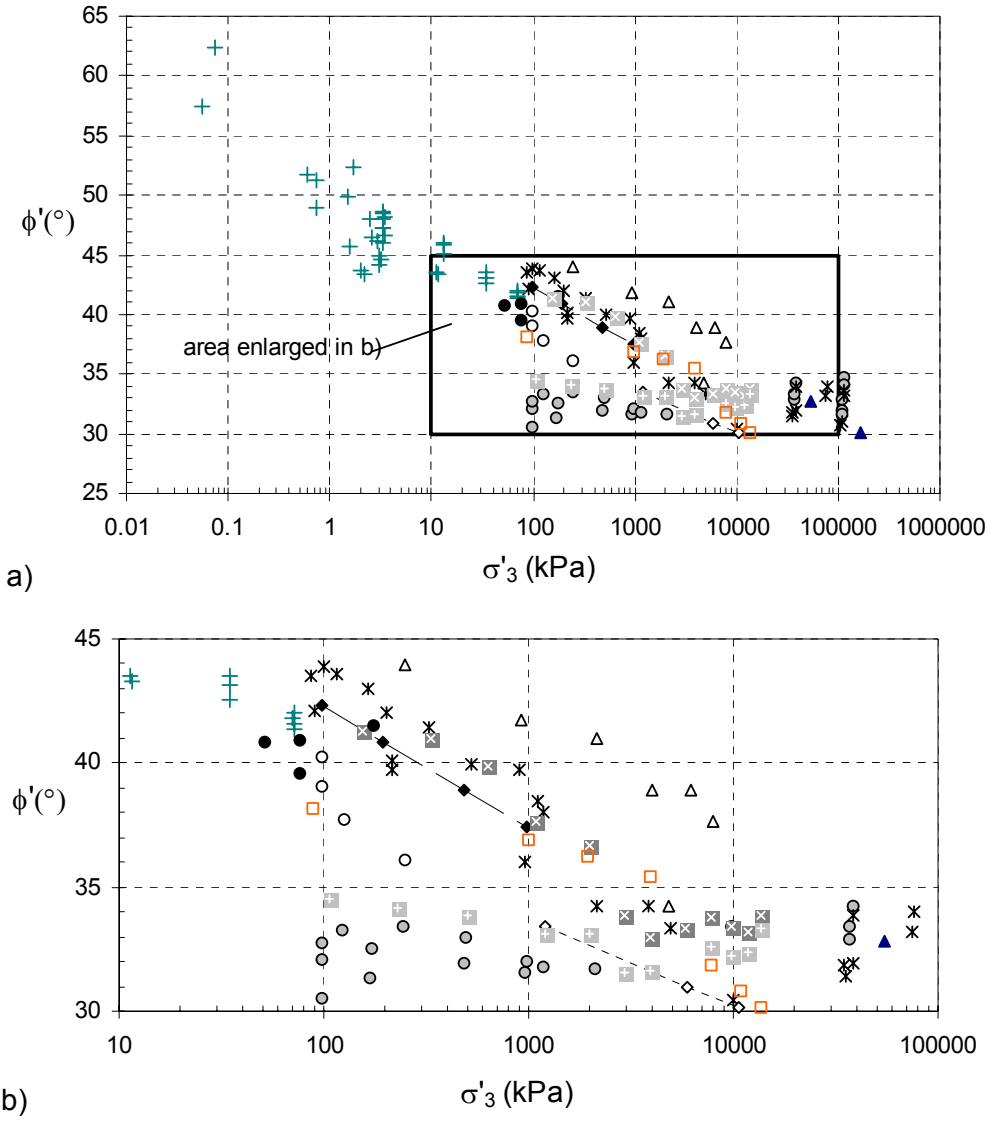

Figure 4.7 *The general trend for the change in ϕ' with change in σ'3 for test data presented in literature.*

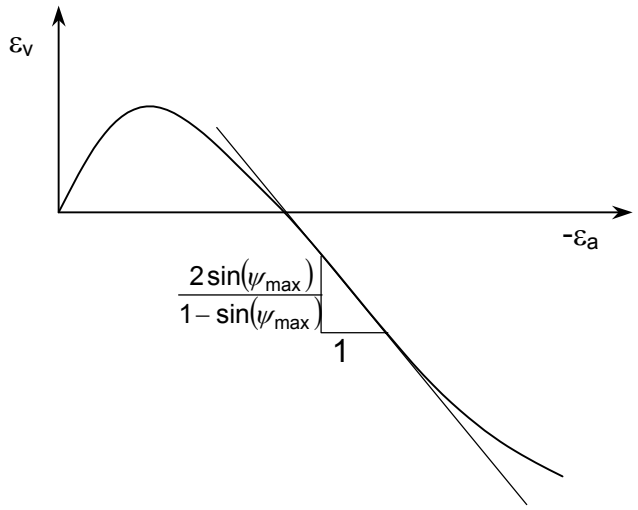

Figure 4.8 *The value of the dilation angle from drained triaxial test data.*

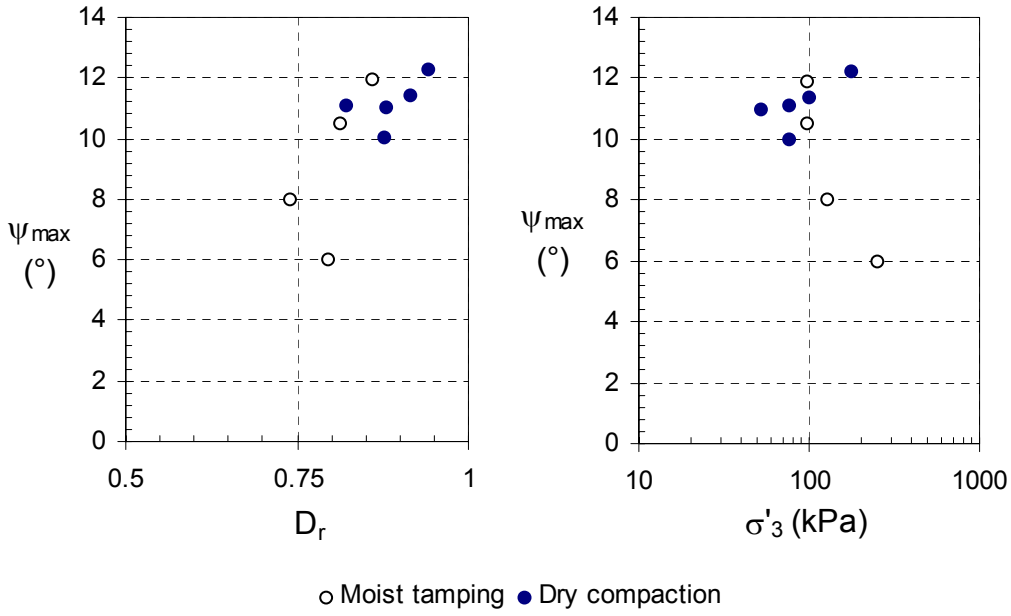

Figure 4.9 *The value of ψ_{max} with respect to relative density, D_r and confining stress, σ'_3 for the tested classified tailings.*

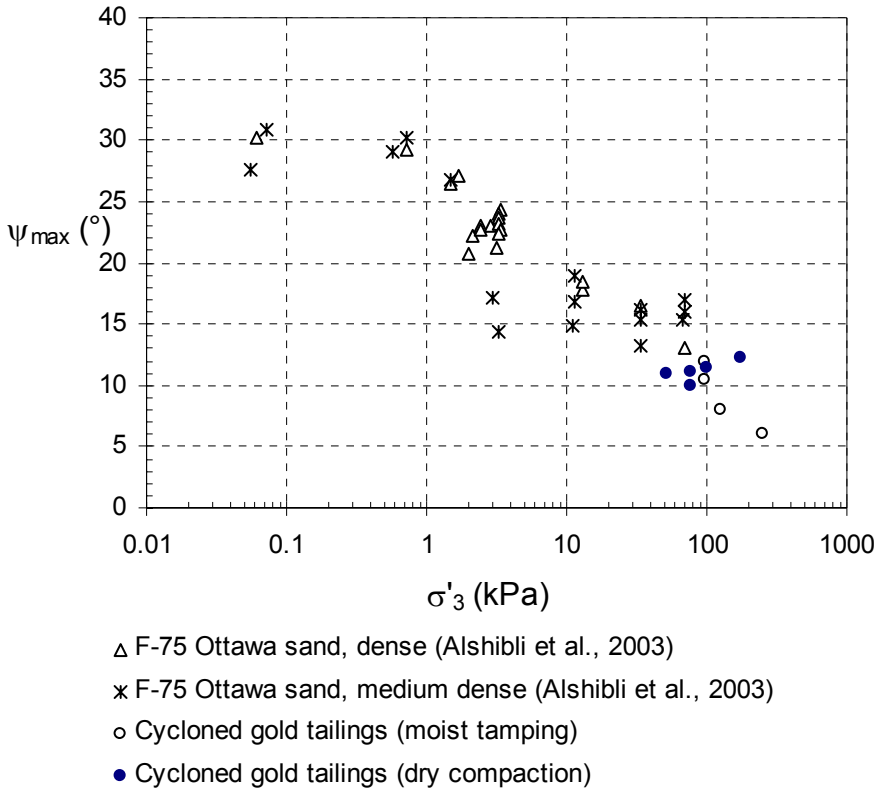

Figure 4.10 *The value of ψ_{max} in relation to σ'_3 for the tested classified tailings and data presented by Alshibli et al. (2003).*

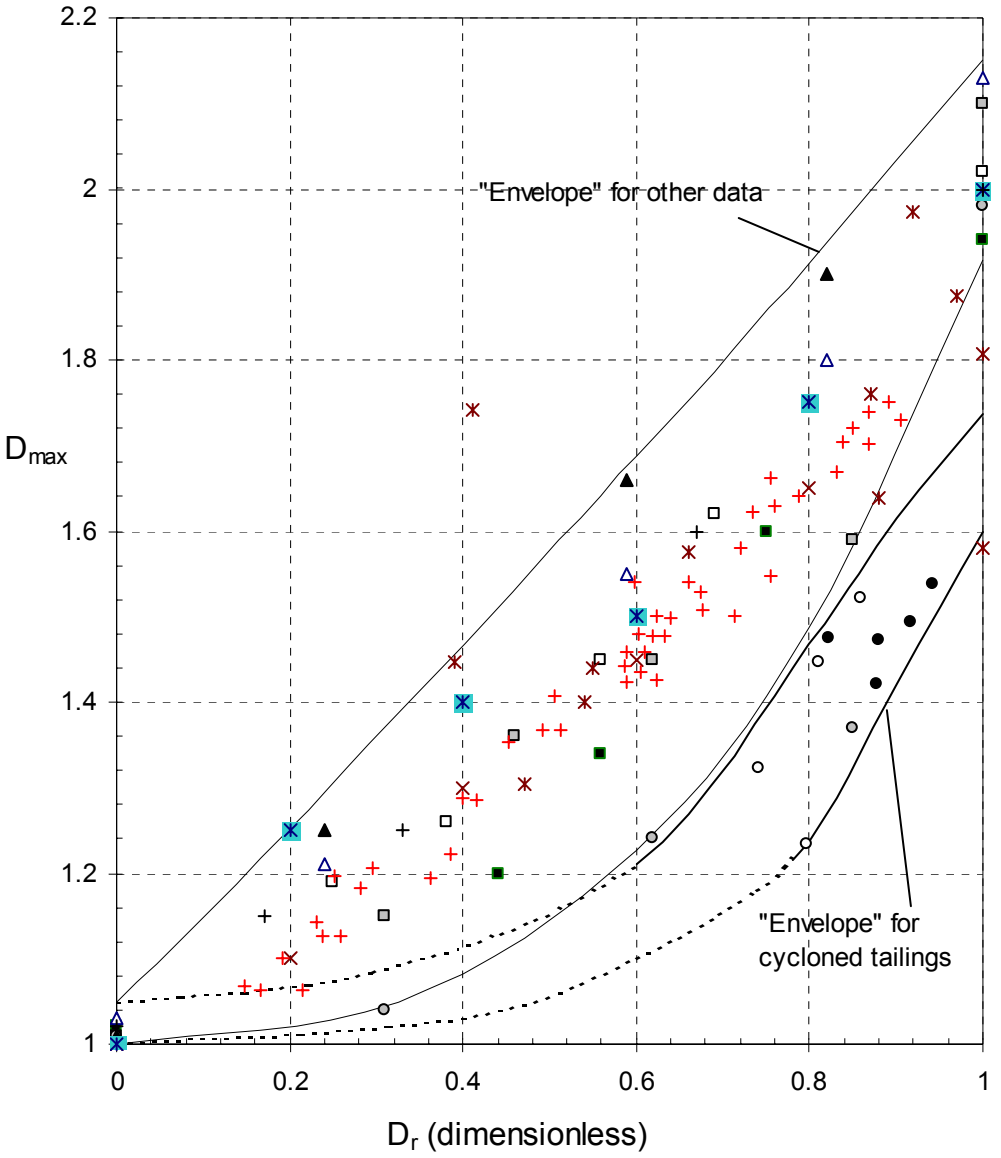

Figure 4.11 *The relationship between the dilational parameter, D_{max}, and the relative density, D_r for the classified tailings and data presented in literature.*

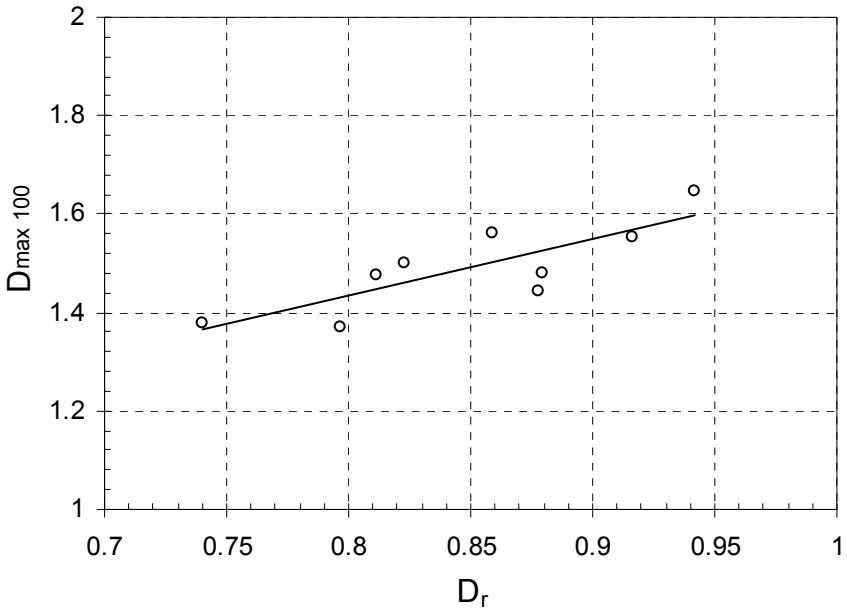

Figure 4.12 *Data of, D_{max}, normalised to σ'_3 = 100 kPa.*

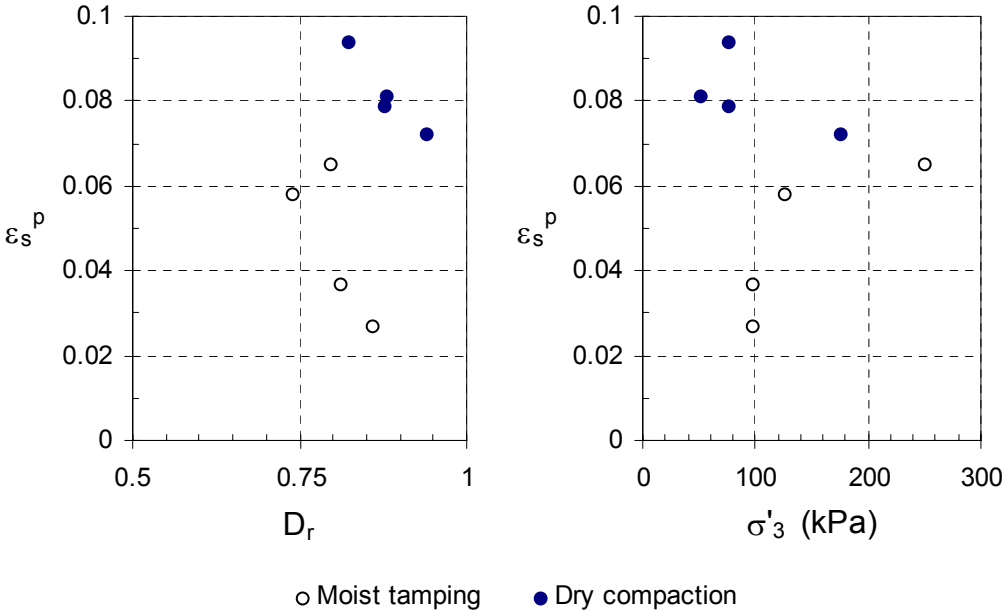

Figure 4.13 *The value of plastic shear strain with respect to relative density, D_r, and confining stress, σ'_3.*

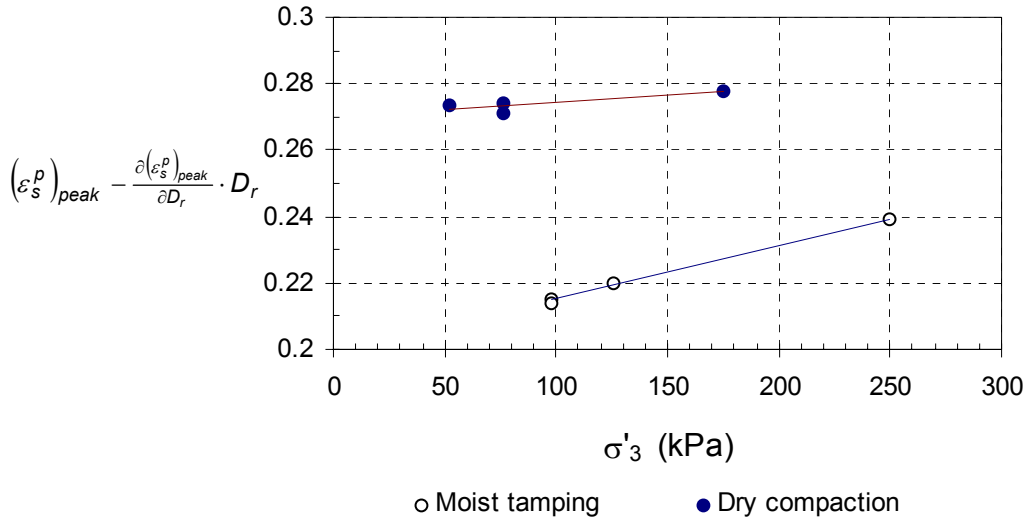

Figure 4.14 *Comparison between the $(\varepsilon_s^p)_{peak}$ for the classified tailings data of the two sample preparation methods.*

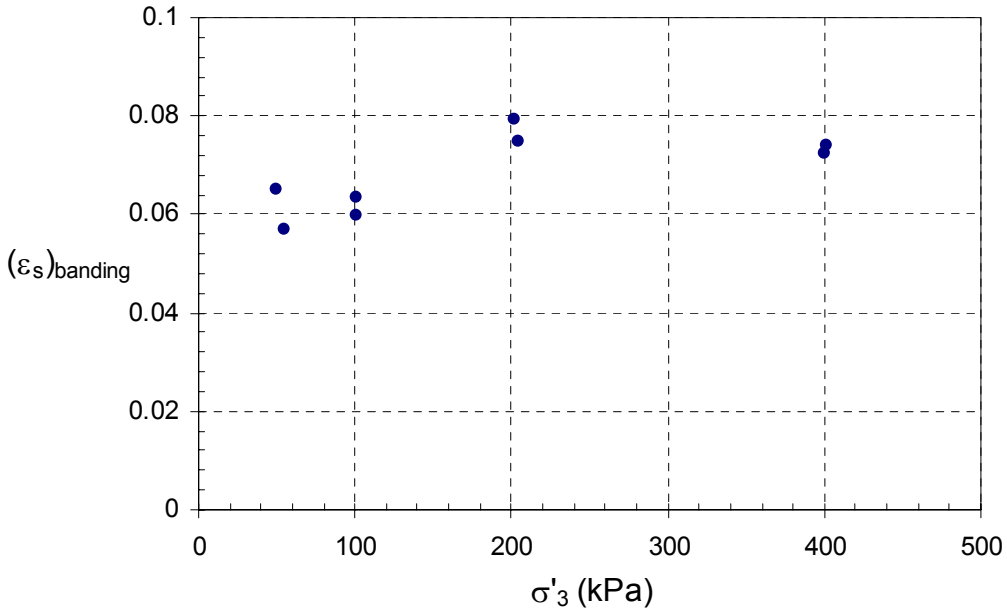

Figure 4.15 *Test data (Han, 1991) of the shear strain intensity at shear banding for coarse Ottawa sand (Papamichos and Vardoulakis, 1995).*

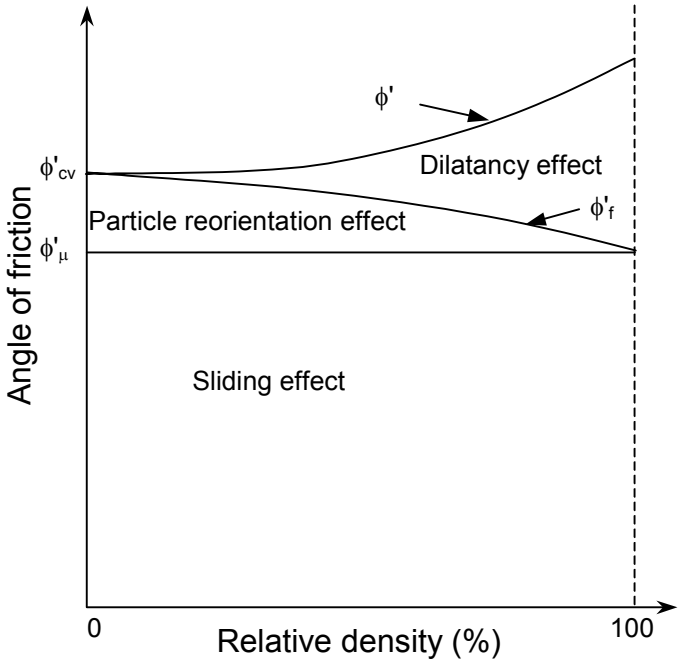

Figure 4.16 Illustration of the components contributing to the strength of granular material (Lee and Seed, 1967).

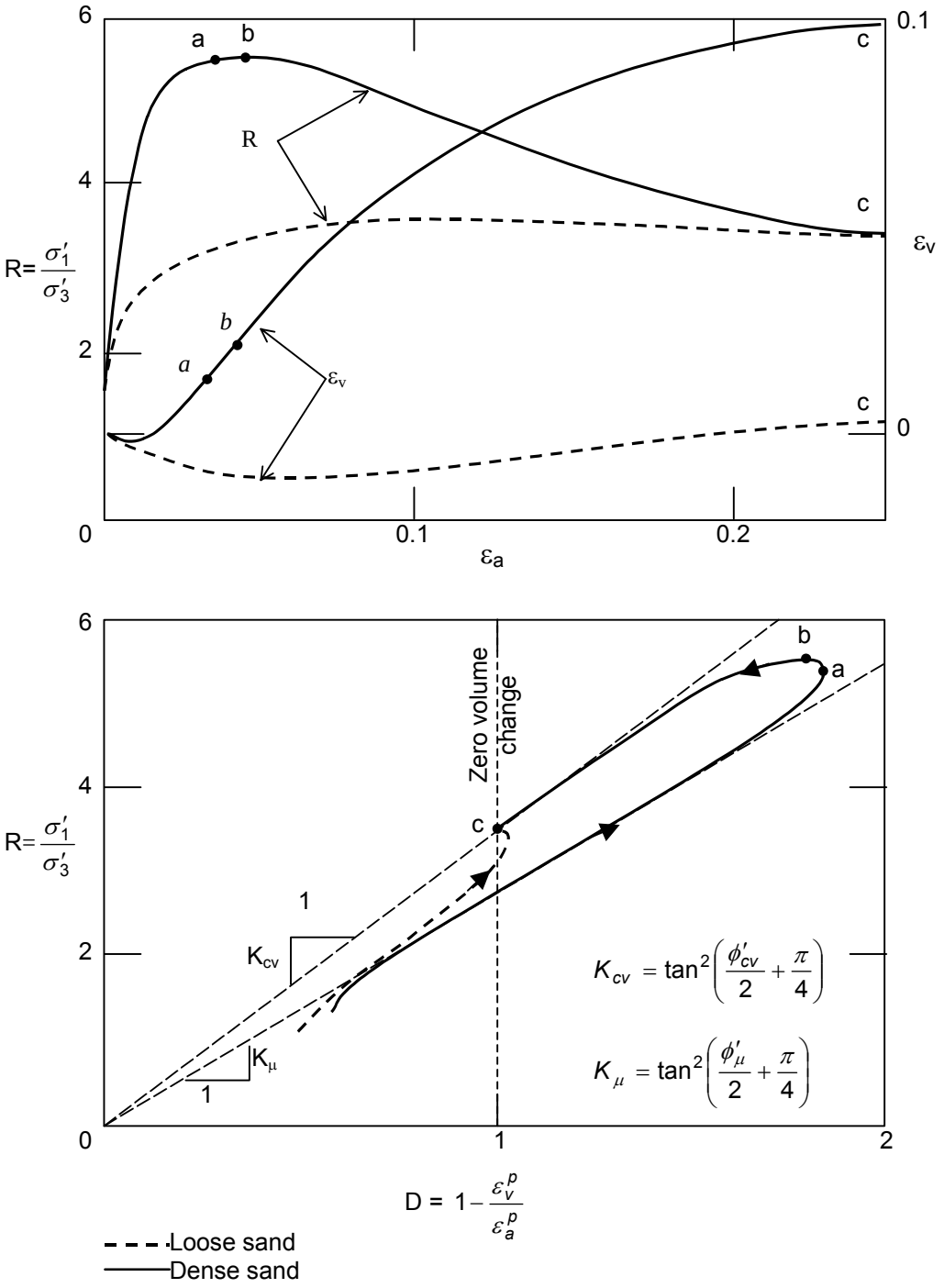

Figure 4.17 *Typical results of triaxial tests on loose and dense sands shown in* R-D *space (based on Horn, 1965a).*

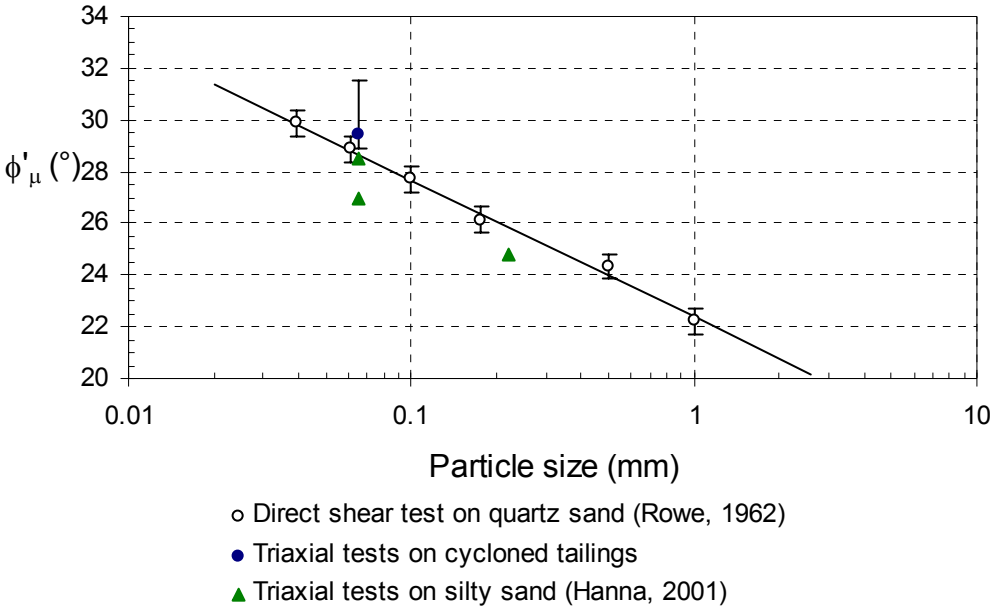

Figure 4.18 *The results of the direct measurement of ϕ'_μ on quartz sand performed by Rowe (1962) with values for silty sand (Hanna, 2001) and cycloned tailings obtained from triaxial test data.*

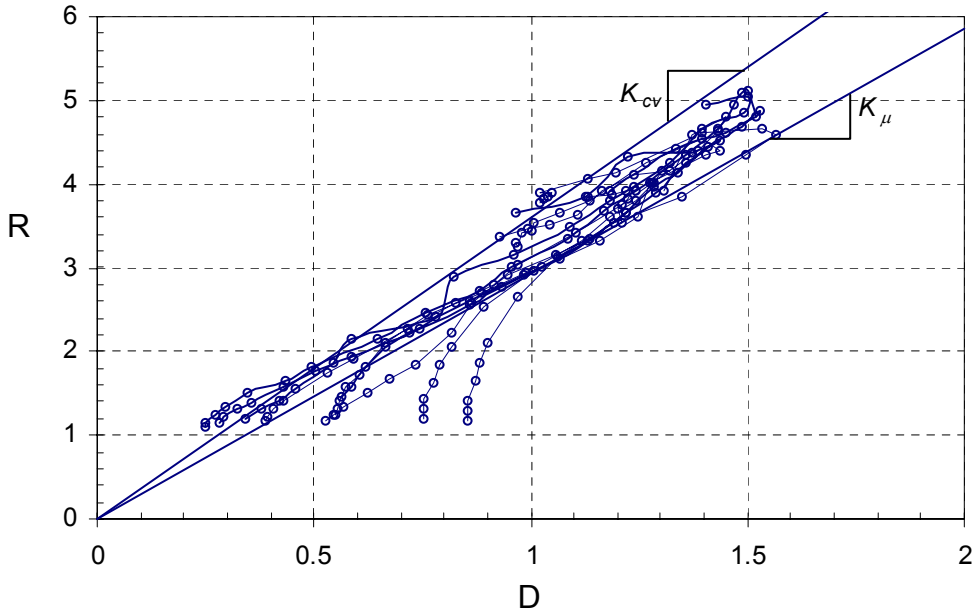

Figure 4.19 *Triaxial test results for all tests on cycloned tailings in* R-D *space.*

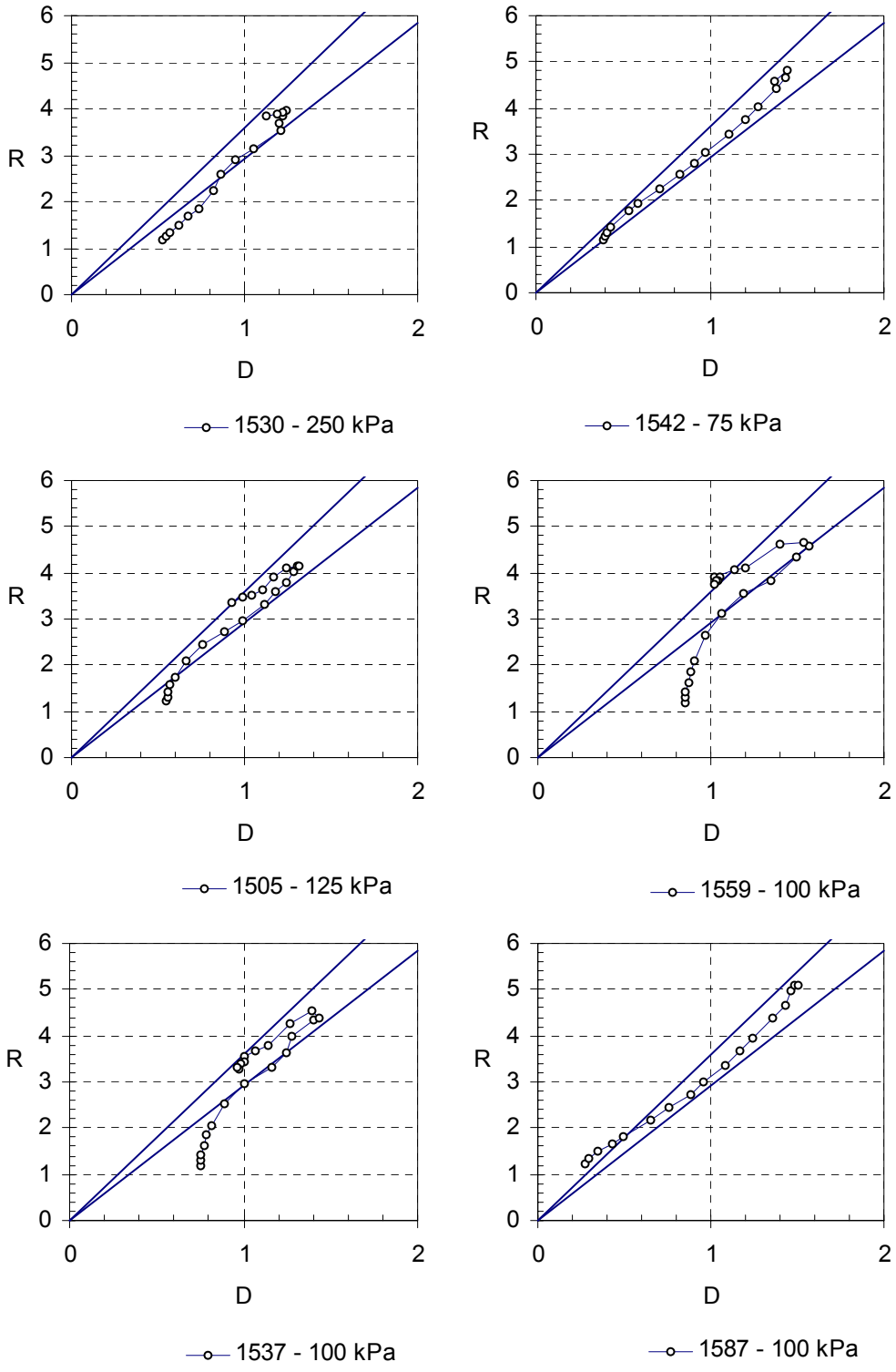

Figure 4.20 *The triaxial test results for all tests on cycloned tailings in* R-D *space showed separately.*

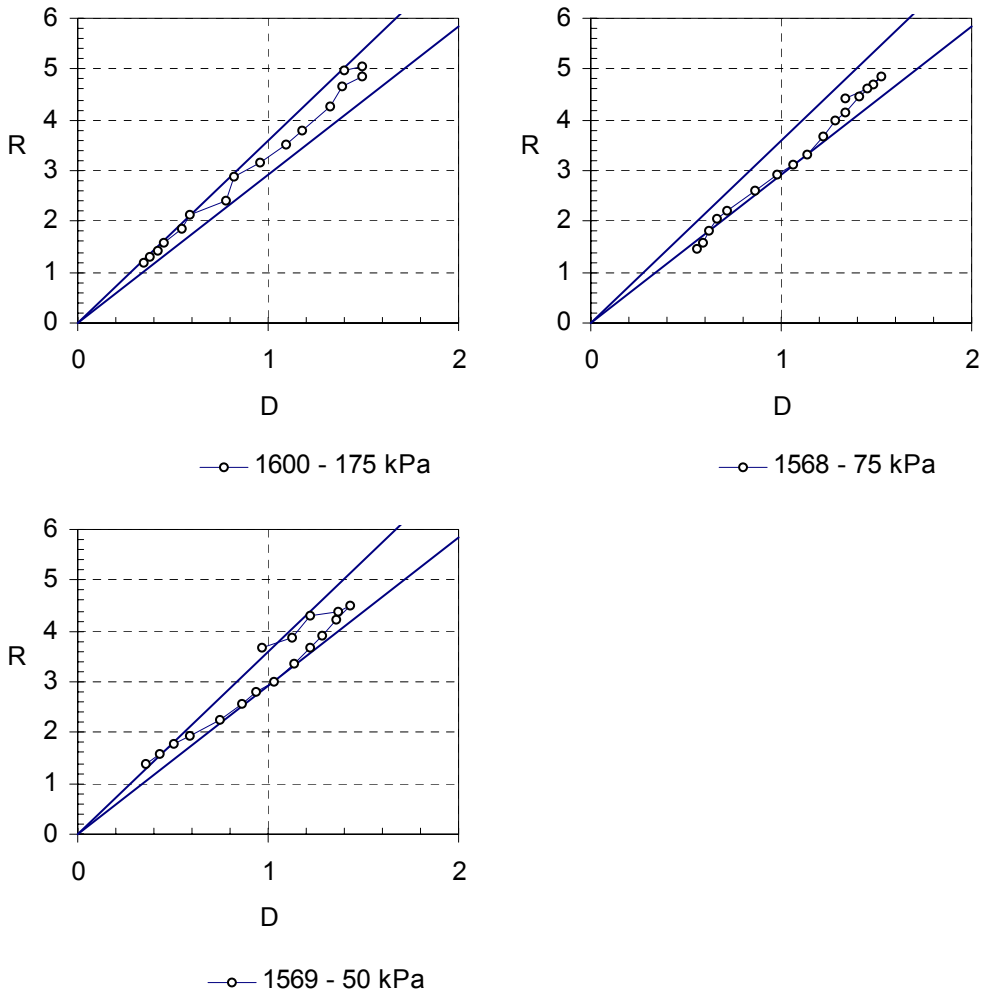

Figure 4.20 (continued) Test results for all tests on cycloned tailings in R-D *space showed separately.*

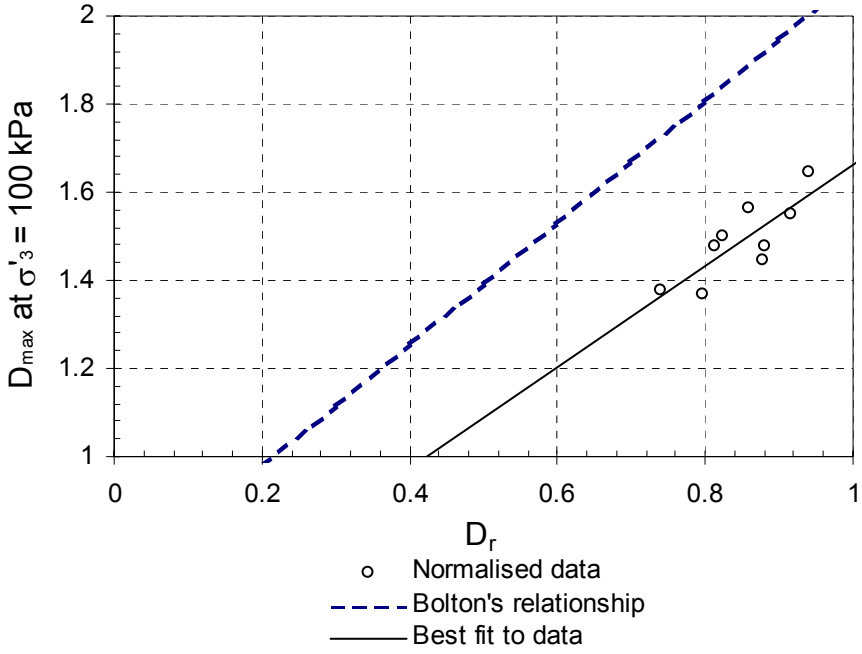

Figure 4.21 *Comparison between the D_{max}, at σ'_3 = 100 kPa obtained experimentally and with Bolton's (1986) expressions.*

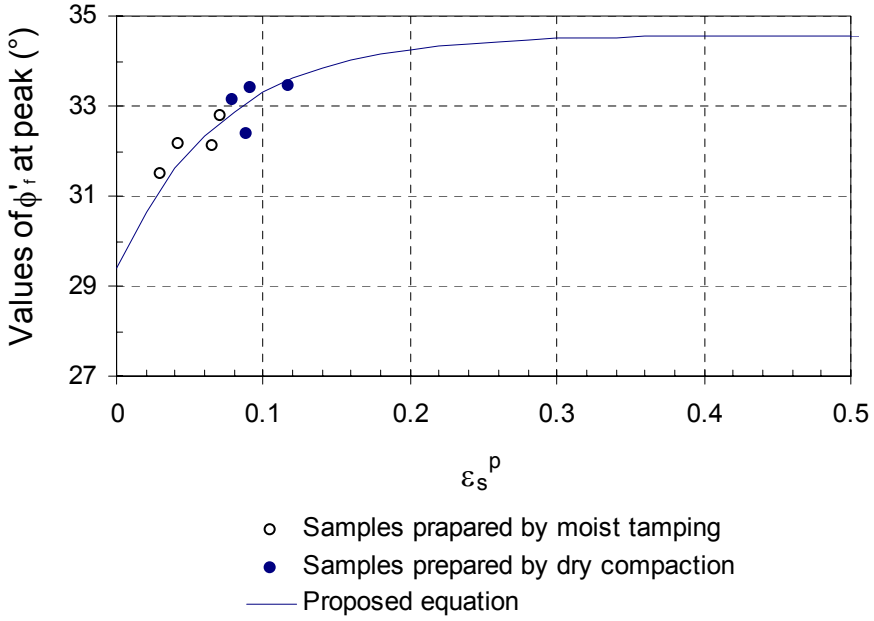

Figure 4.22 *Values of ϕ'_f at peak stress for the tested cycloned tailings.*

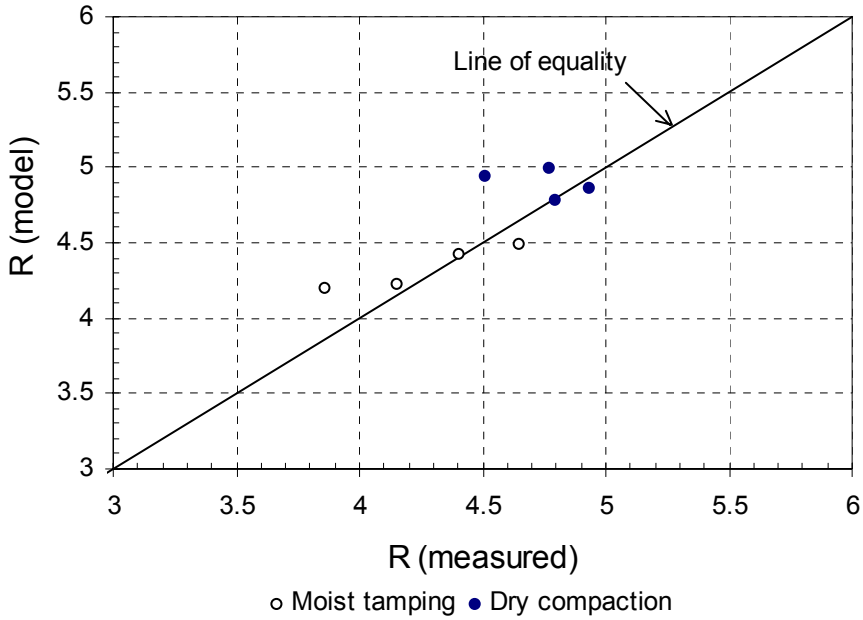

Figure 4.23 Measured and predicted values of R *for the cycloned tailings material.*

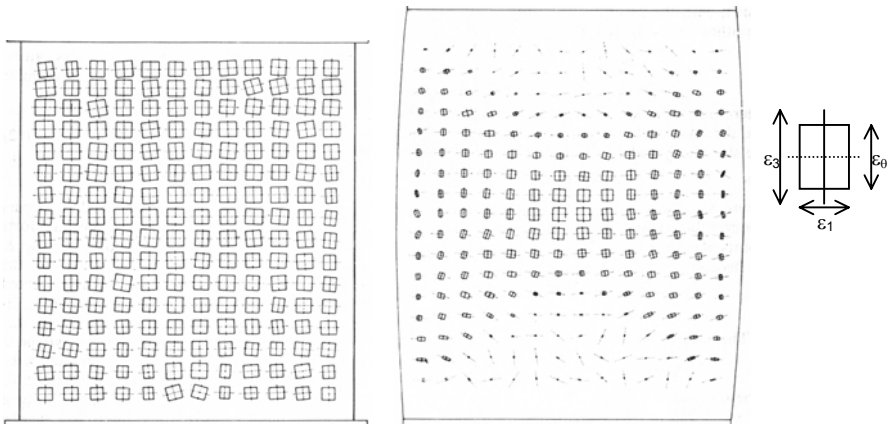

a) Lubricated end platens b) Non-lubricated end platens

Figure 4.24 Uniform and non-uniform deformation modes in test samples with lubricated and non-lubricated end-platens (Deman, 1975).

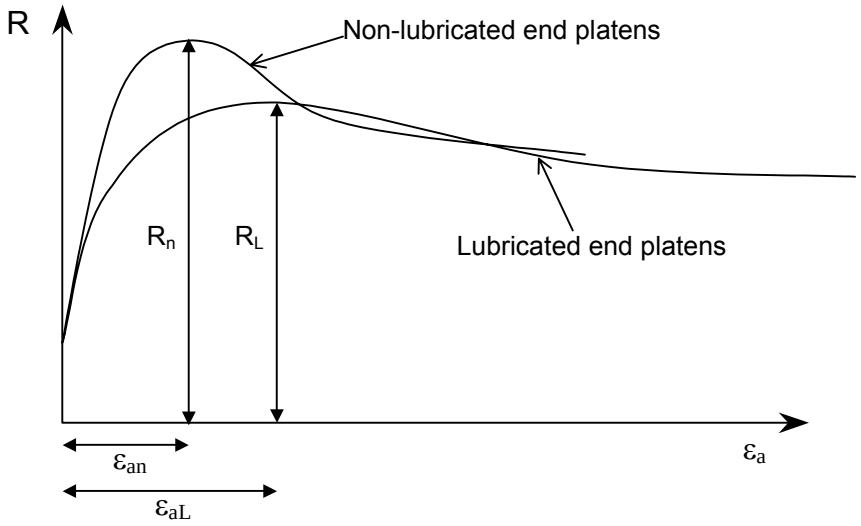

Figure 4.25 Stress-strain curves for triaxial tests with lubricated and non-lubricated end platens.

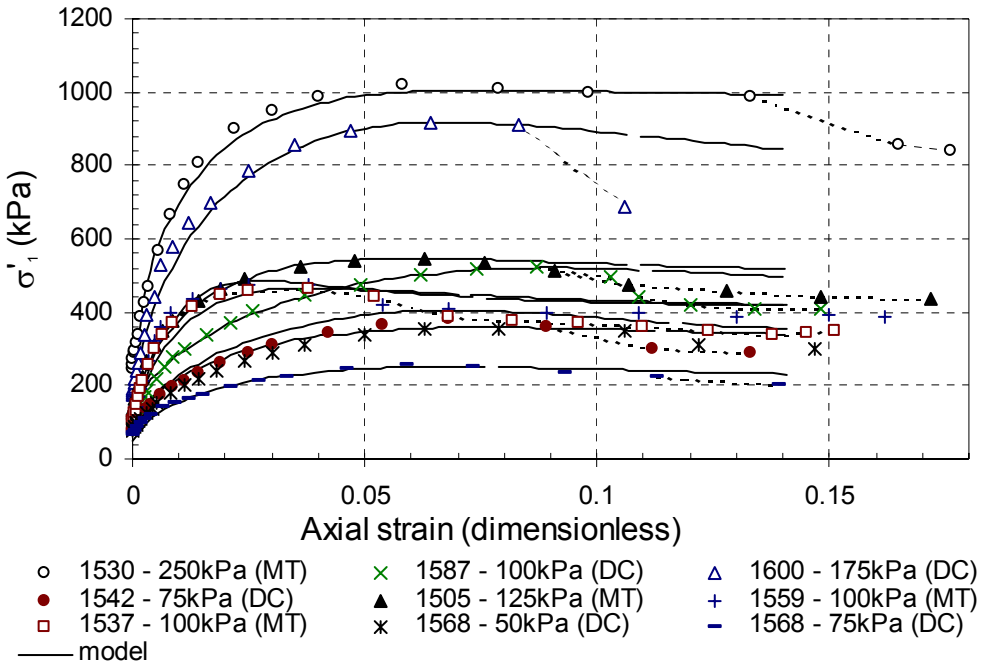

Figure 4.26 *Comparison between the stress-strain data and the numerical modelling for the cycloned tailings material.*

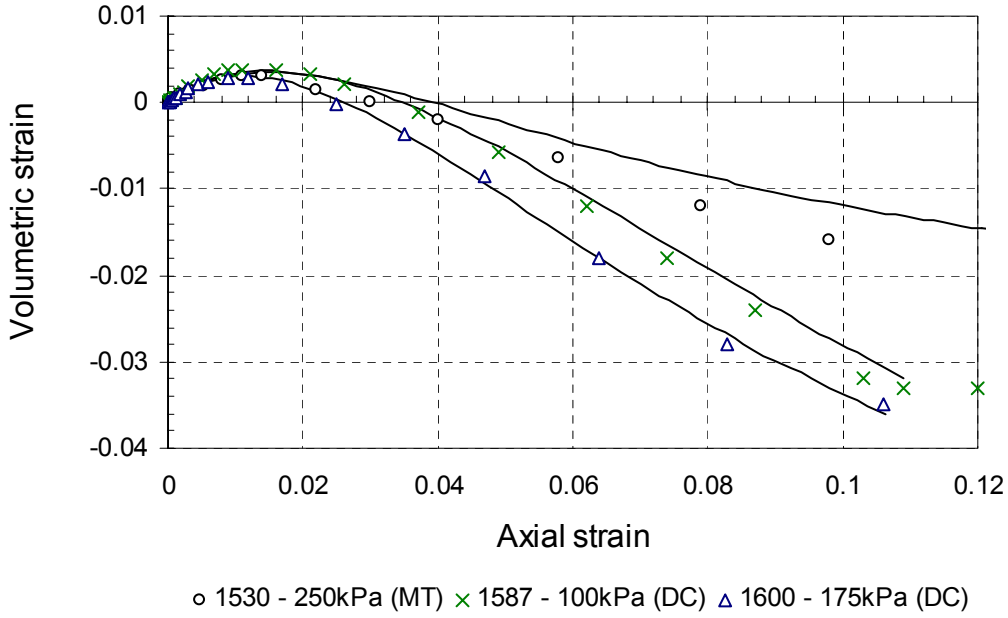

Figure 4.27 *Comparison between the volumetric-axial strain data and the numerical modelling for the cycloned tailings material.*

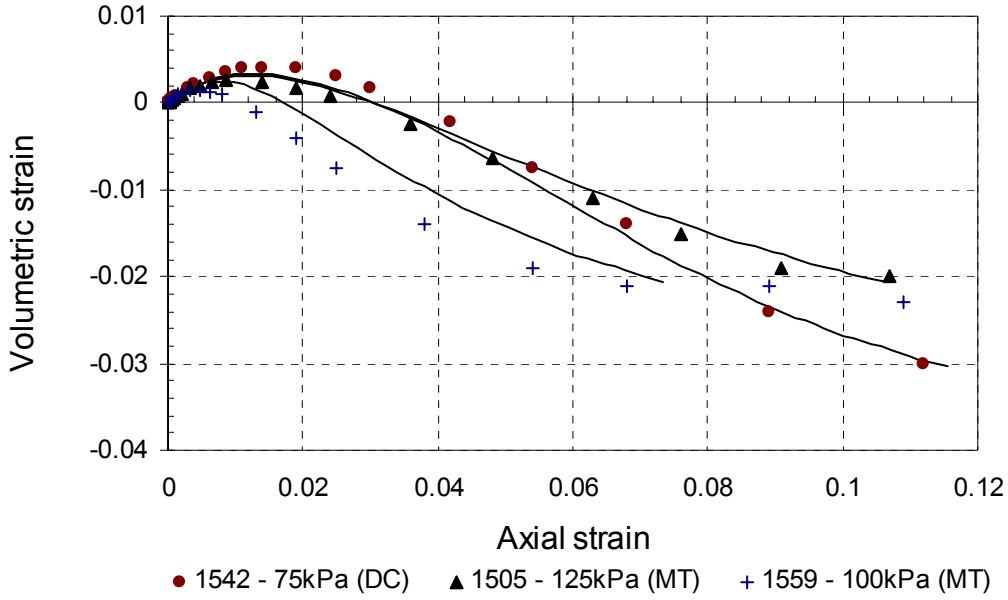

Figure 4.28 *Comparison between the volumetric-axial strain data and the numerical modelling for the cycloned tailings material.*

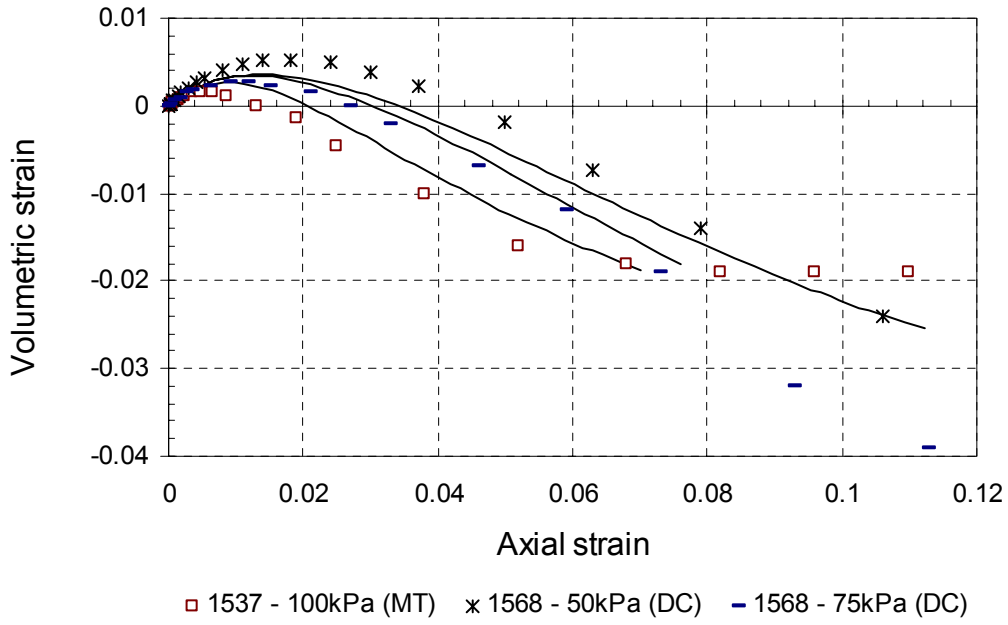

Figure 4.29 *Comparison between the volumetric-axial strain data and the numerical modelling for the cycloned tailings material.*

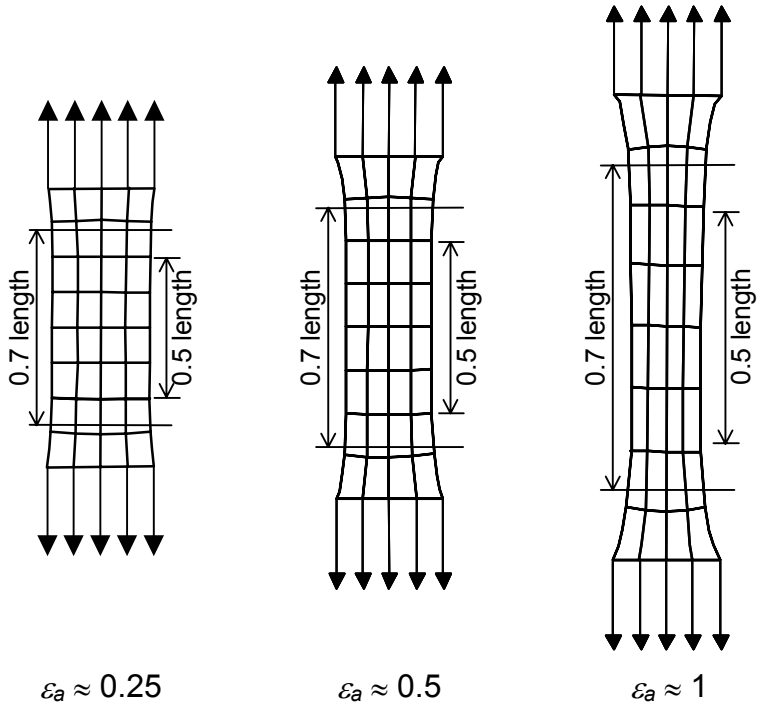

Figure 4.30 Measured deformation profiles of the geomembranes in a uniaxial tensile test.

.

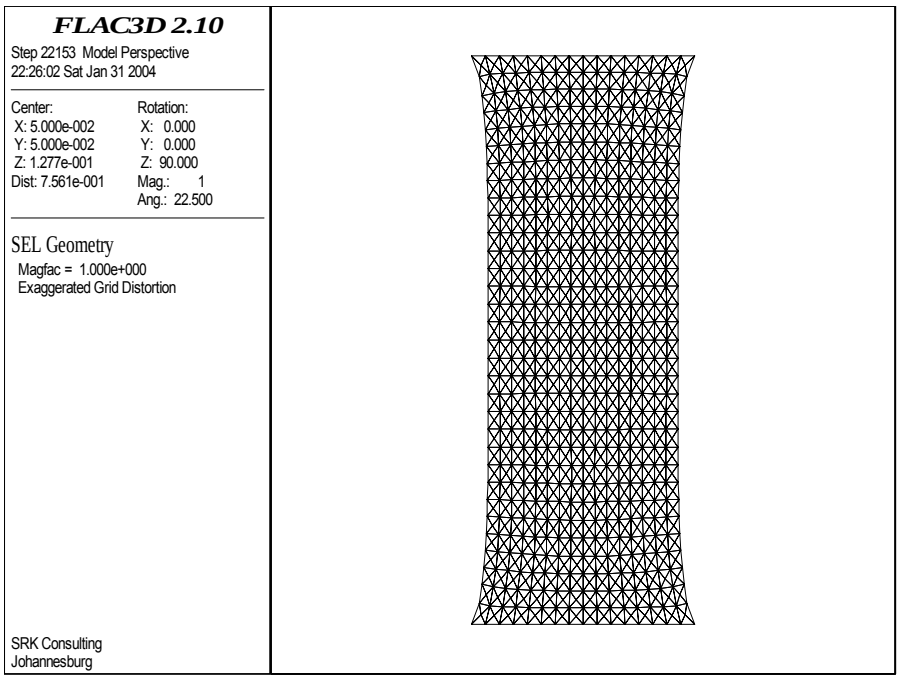

Figure 4.31 Deformed grid of FLAC3D analyses on uniaxial tensile test on membrane.

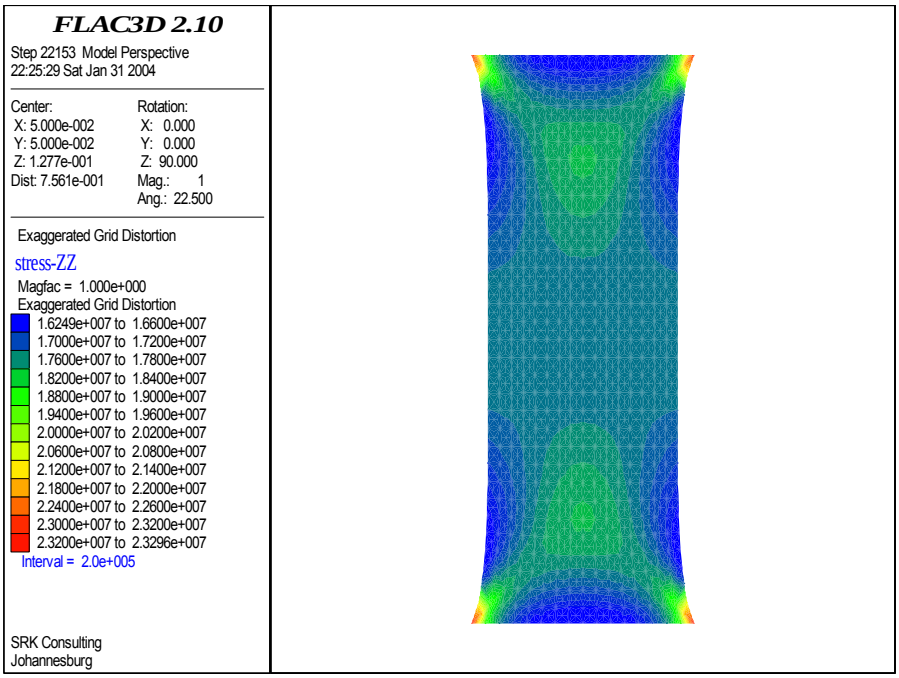

Figure 4.32 Vertical stress from FLAC3D analyses of a uniaxial tensile test on membrane.

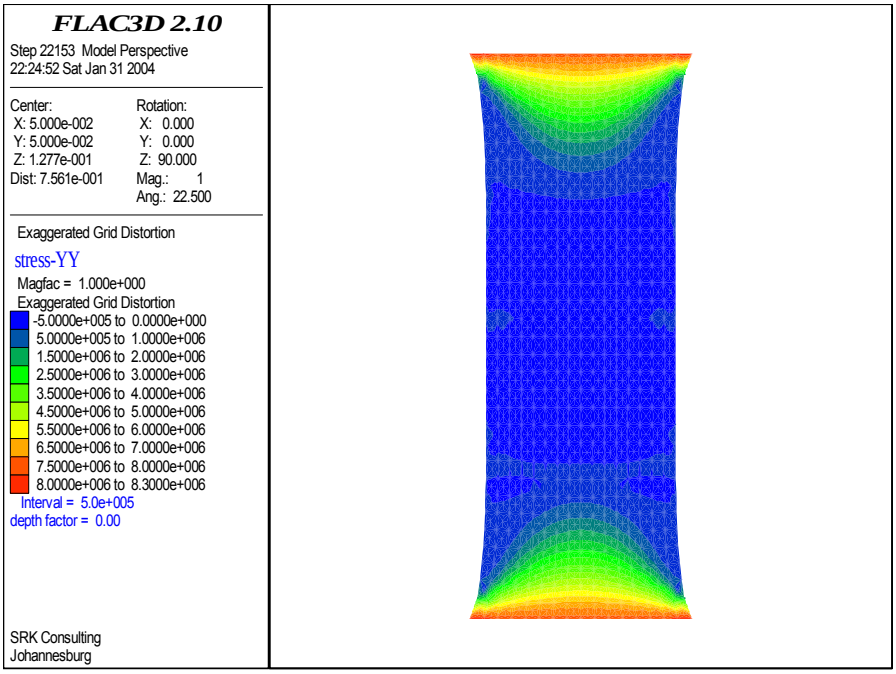

Figure 4.33 In-plane horizontal stress from FLAC3D analyses of a uniaxial tensile test on membrane.

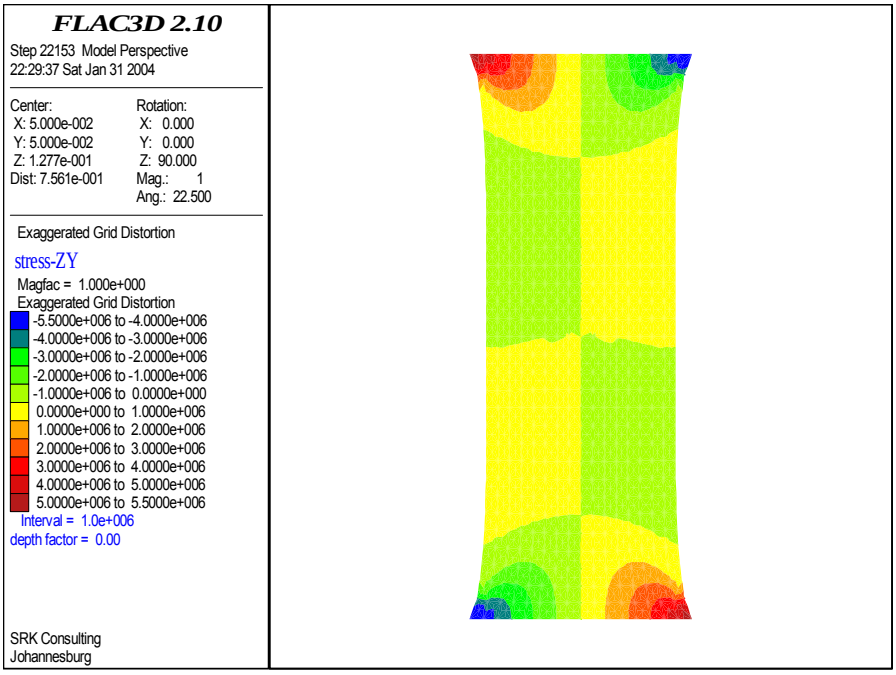

Figure 4.34 In-plane shear stress from FLAC3D analyses of a uniaxial tensile test on membrane.

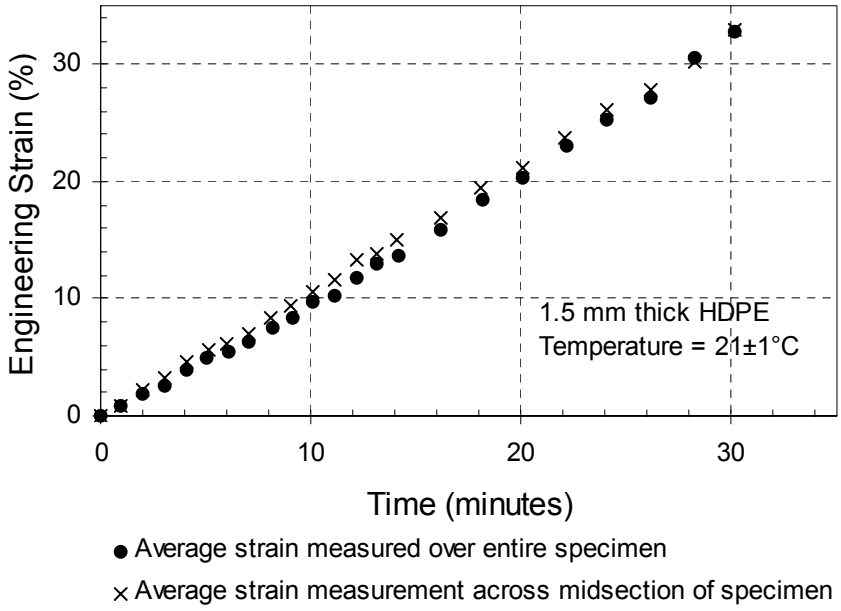

Figure 4.35 Axial strain during a wide-strip tensile tension test on 1.5 mm HDPE membrane (Merry and Bray 1996).

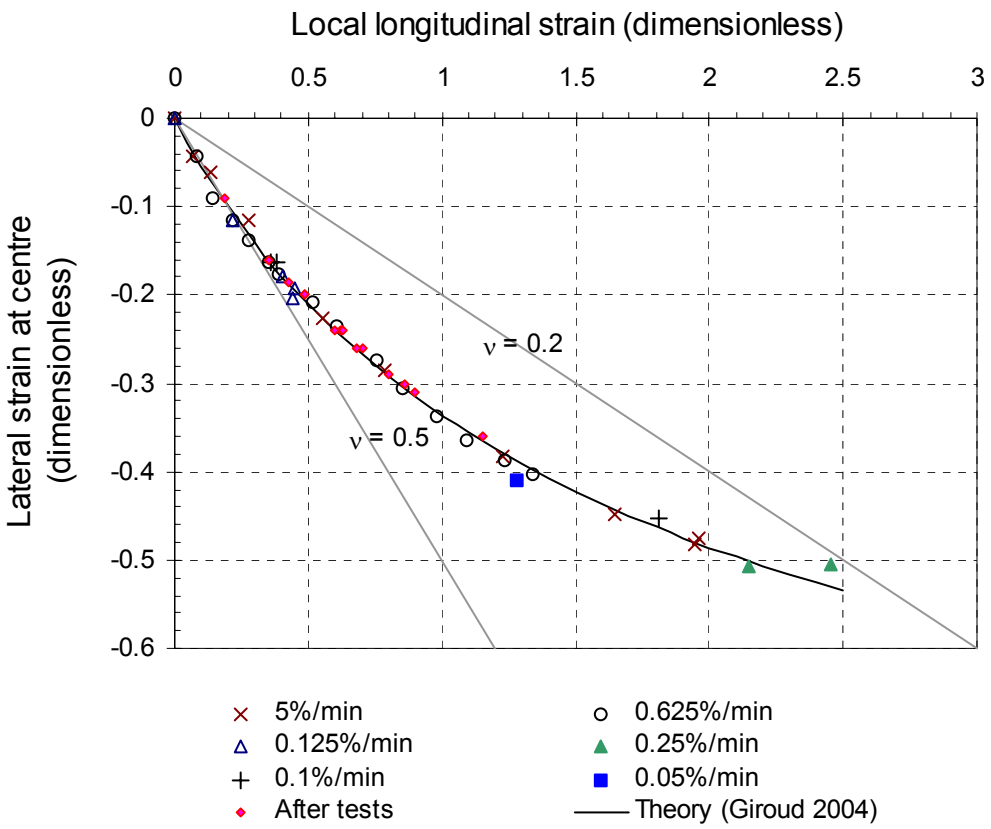

Figure 4.36 Local lateral strain compared to local longitudinal strain obtained from the uniaxial tensile tests on the membranes.

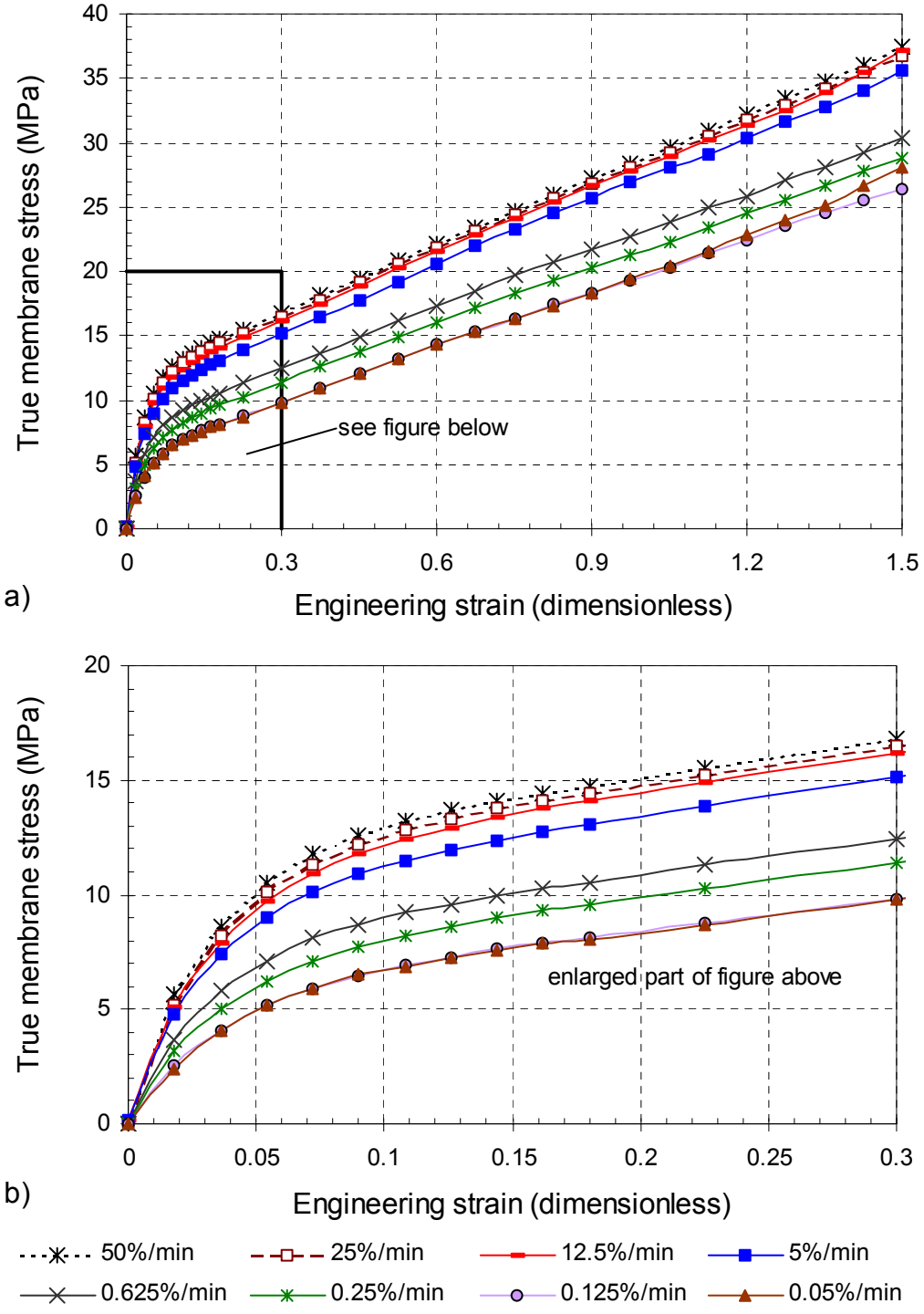

Figure 4.37 Membrane behaviour in terms of true stress and engineering strain.

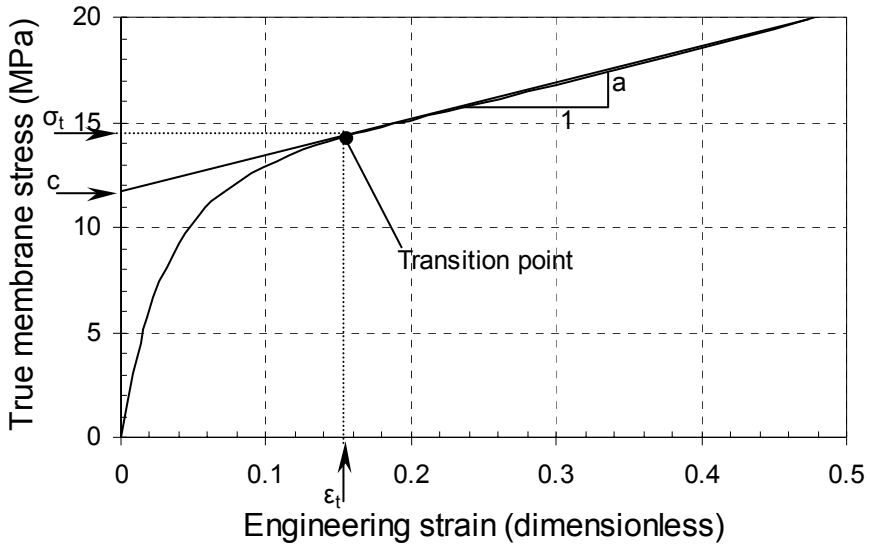

Figure 4.38 *Definition of the transition point in the stress-strain curve for the HDPE membranes under uniaxial loading.*

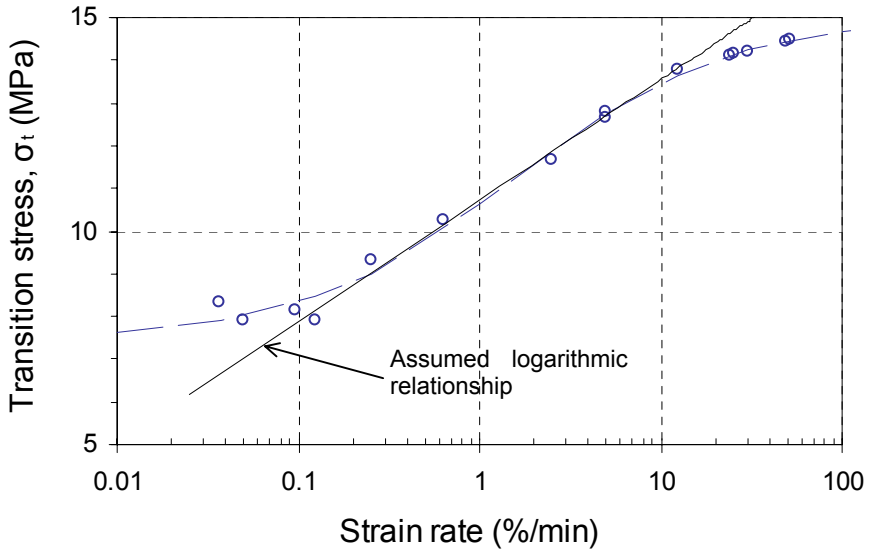

Figure 4.39 *Relationship of transition stress to strain rate for the test data.*

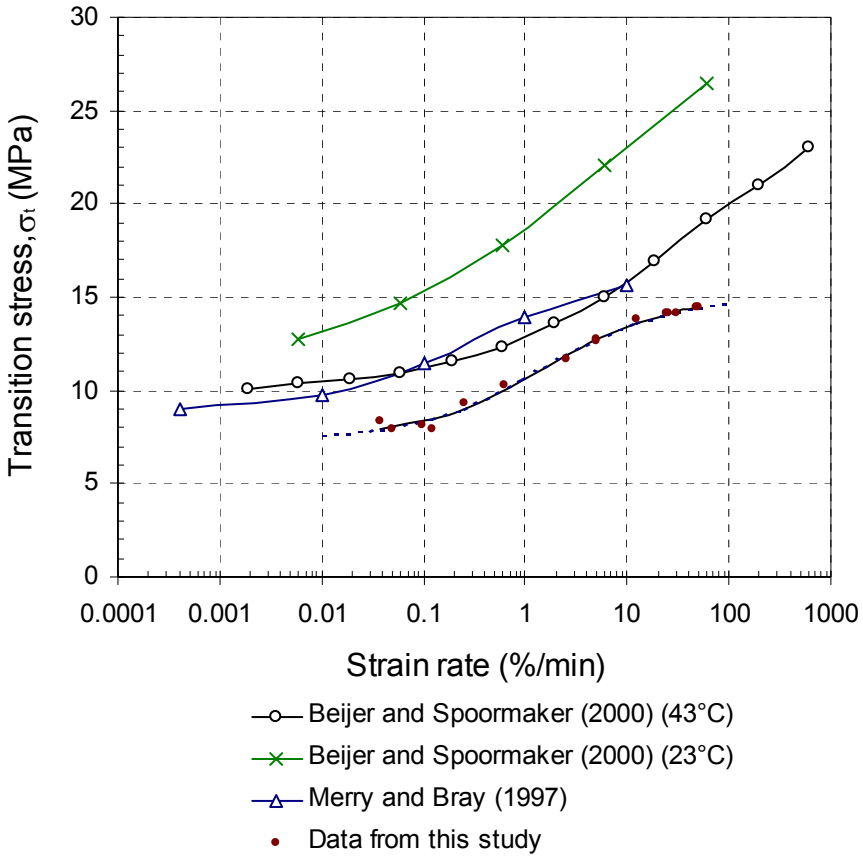

Figure 4.40 Relationship of transition stress to strain rate obtained from data presented in literature.

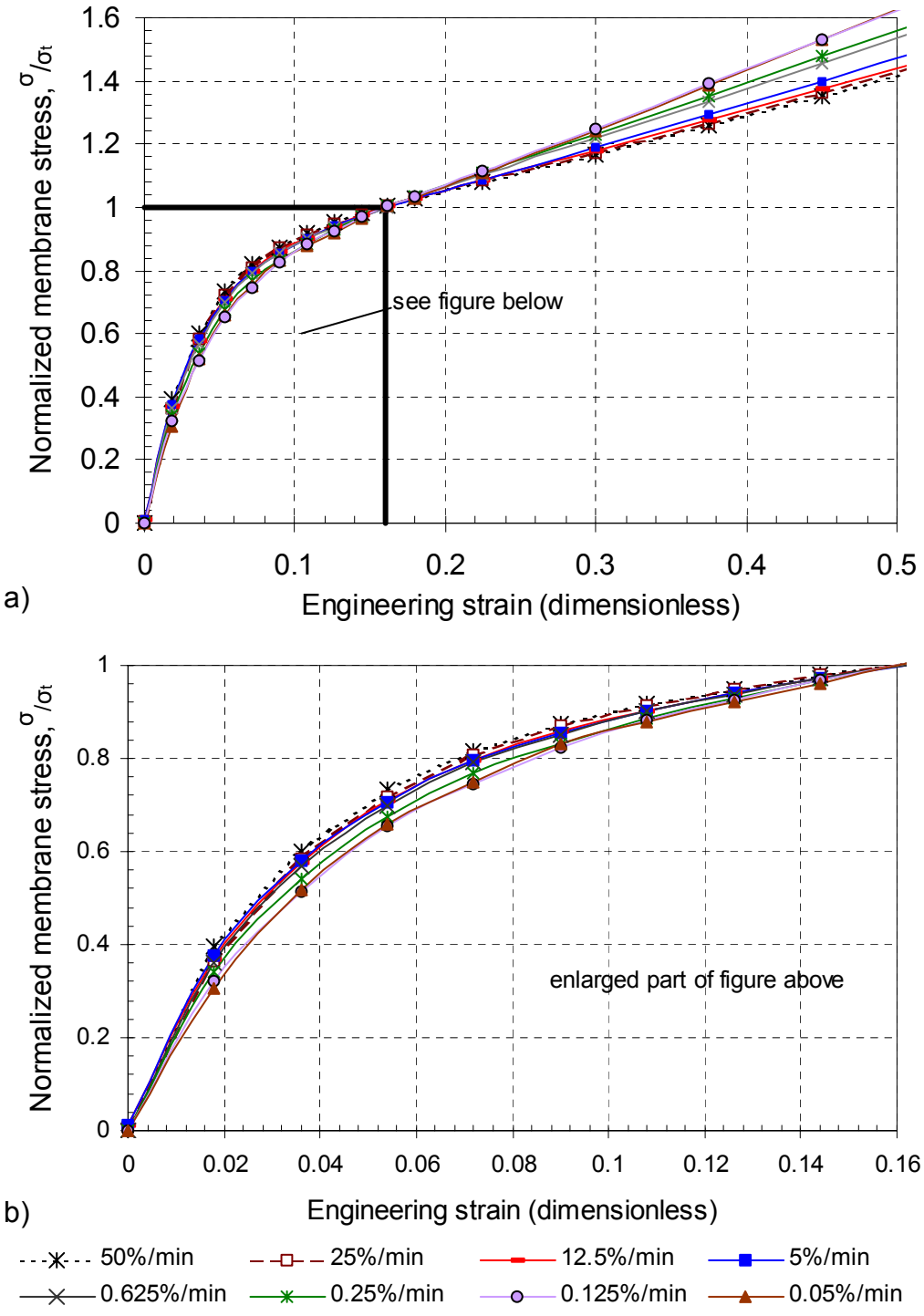

Figure 4.41 Normalized membrane stress-strain curve.

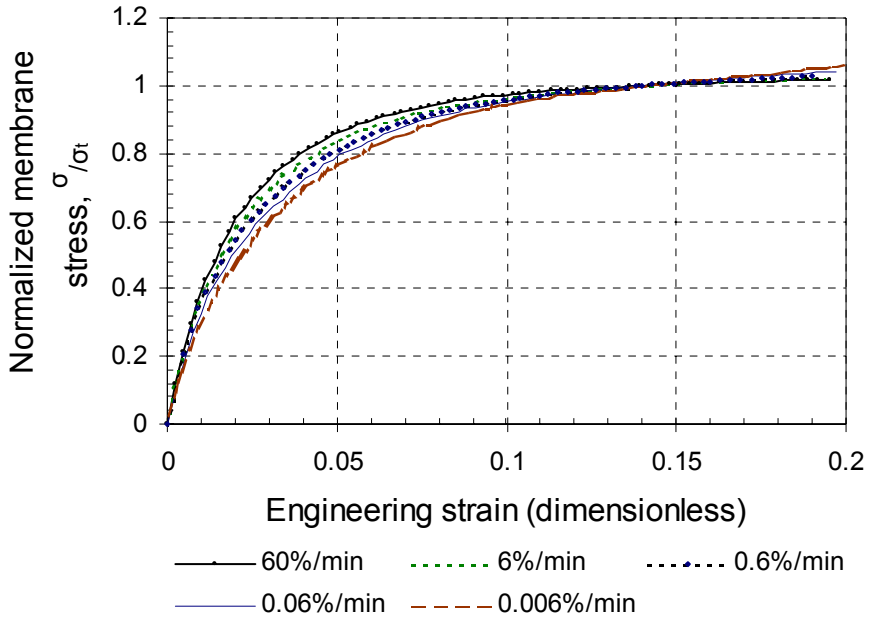

a)

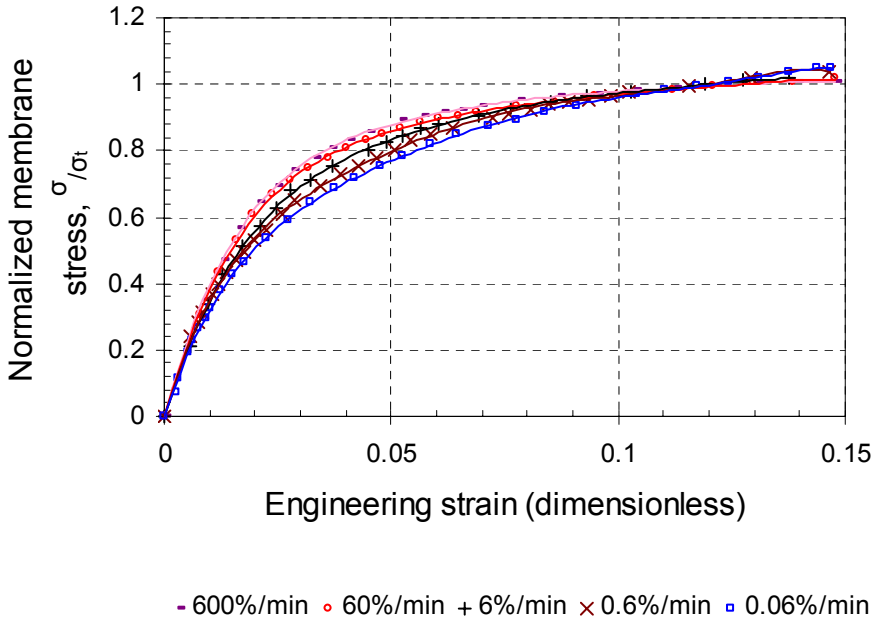

b)

Figure 4.42 *Normalized stress-strain curves for data of* (a) *tensile tests on injection moulding grade HDPE bars (Beijer and Spoormaker, (2000)) and* (b) *compression tests on HDPE recovered from pipes (Zhang and Moore, 1997a).*

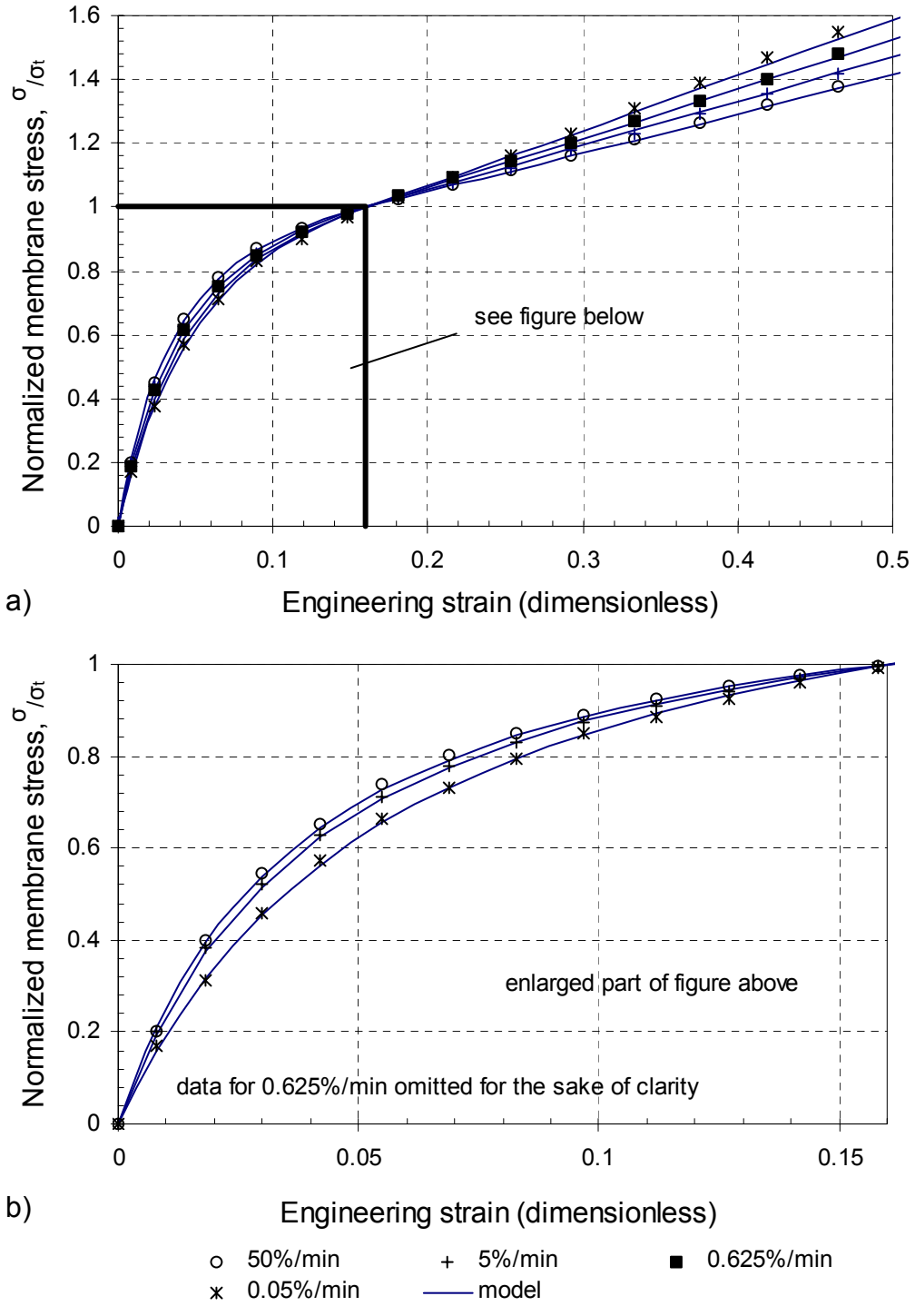

Figure 4.43 Comparison between normalized stress-strain functions of the hyperbolic model and the data.

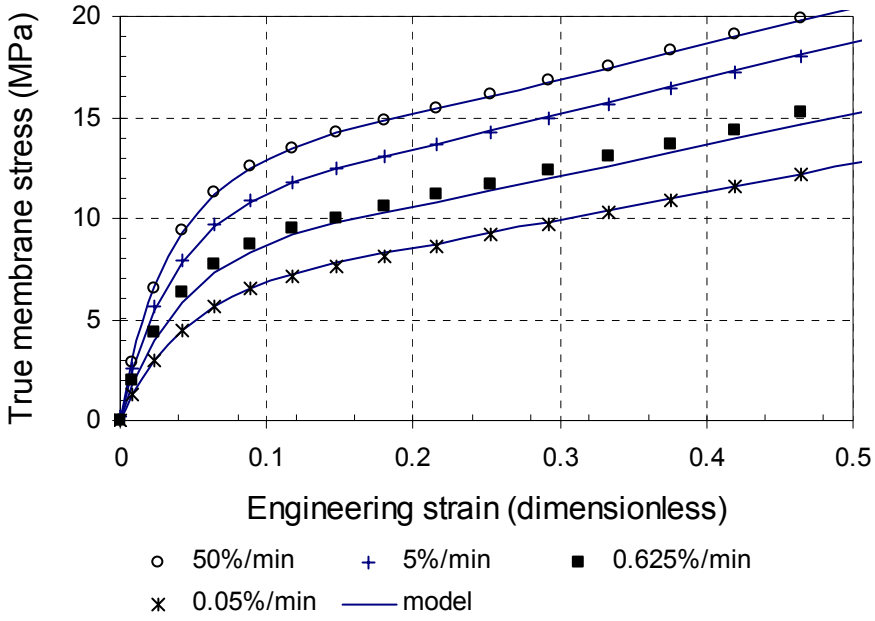

Figure 4.44 Comparison between the hyperbolic model and the original data.

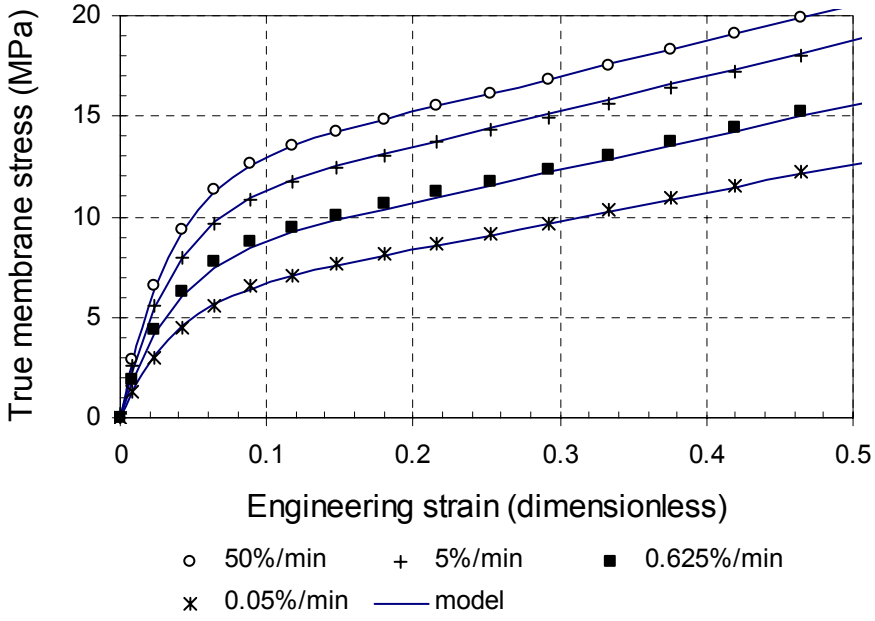

Figure 4.45 Comparison between the exponential model and the original data.

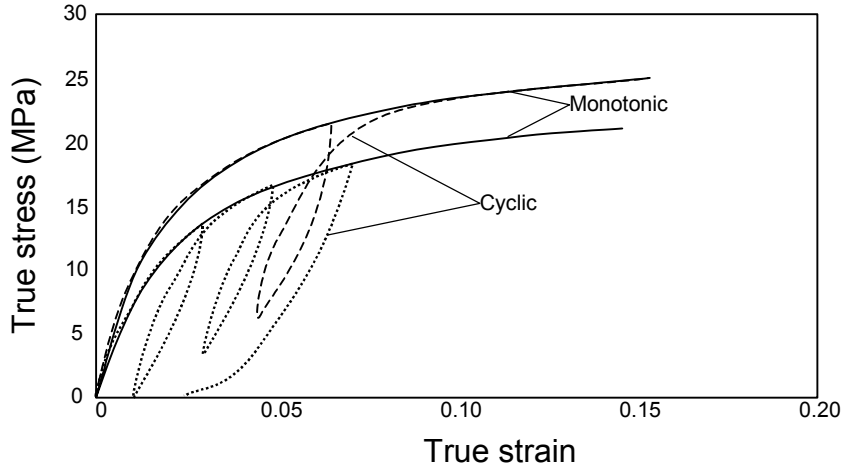

a) Results of cyclic and constant strain compressive tests

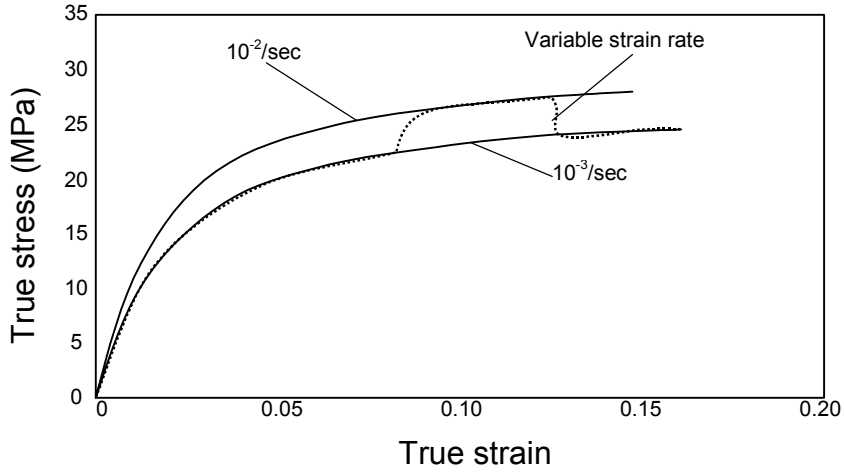

b) Results of constant and variable strain rate tests

Figure 4.46 Results of constant, variable strain rate and cyclic loading tests on HDPE specimens recovered from pipes (Zhang and Moore, 1997a).

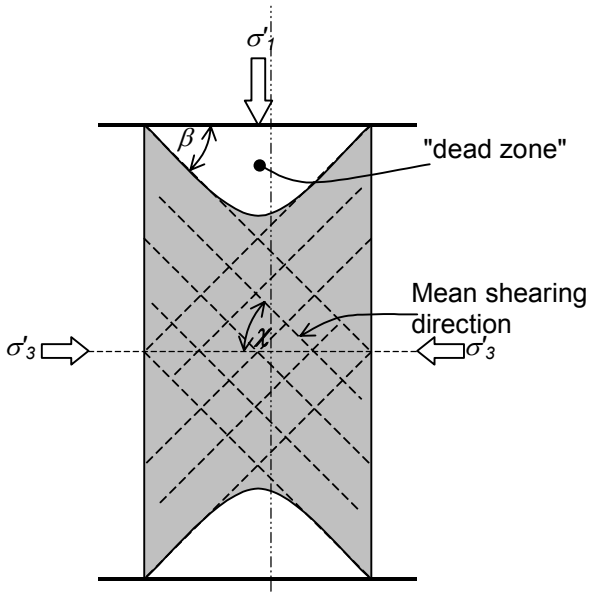

Figure 4.47 *Illustration of the hypothesis that the angle β is equal to the angle χ.*

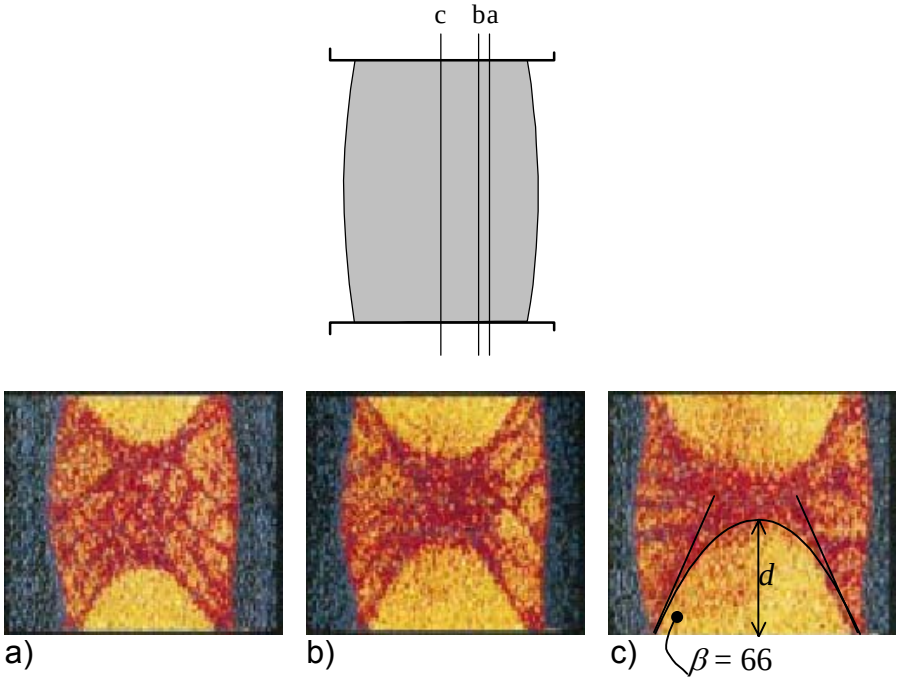

Figure 4.48 *Computed tomographic images of silty sand tested in a conventional triaxial test (Alshibli et al. (2003)) with proposed parabolic estimate of the extent of the "dead zone".*

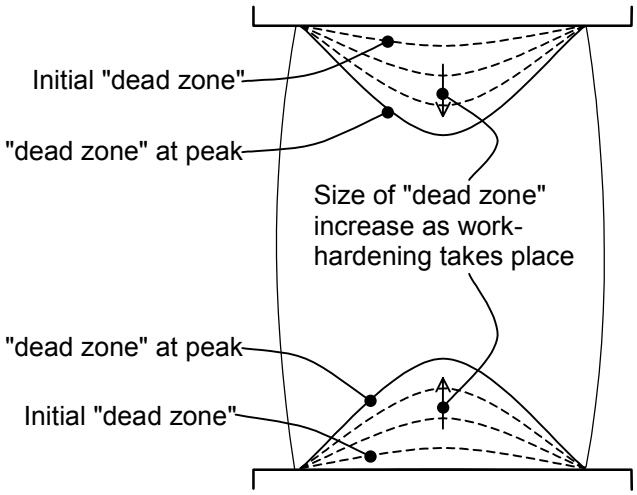

Figure 4.49 *Illustration of the change in the size of the dead zone with strain-hardening of the soil.*

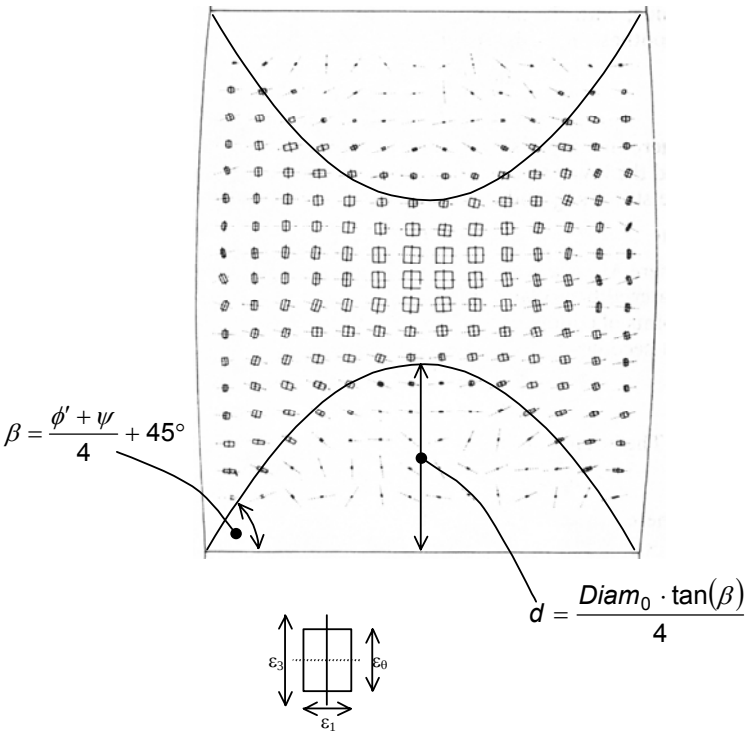

Figure 4.50 *Internal deformation field for dense sand in conventional triaxial test apparatus (Deman, 1975) with proposed parabolic estimate of the extent of the "dead zone".*

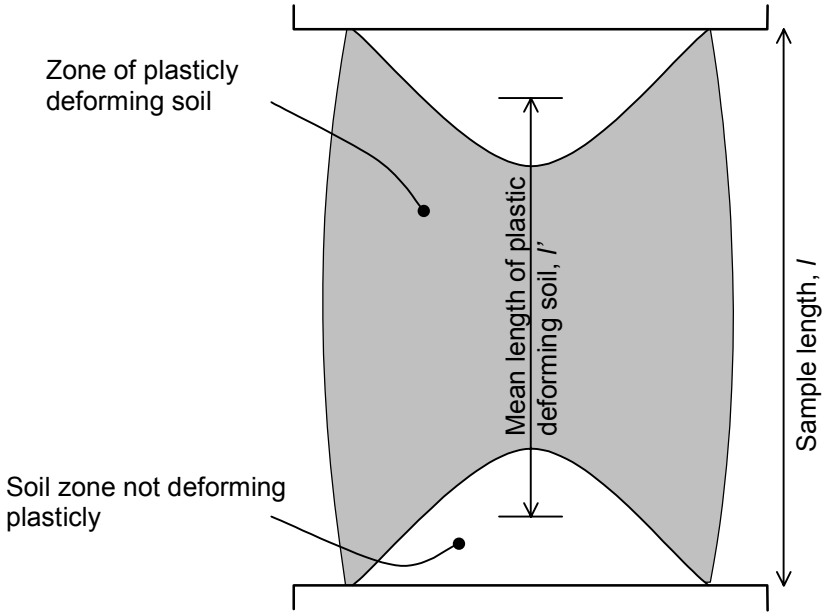

Figure 4.51 The mean length of the plasticly deforming part of the soil cylinder.

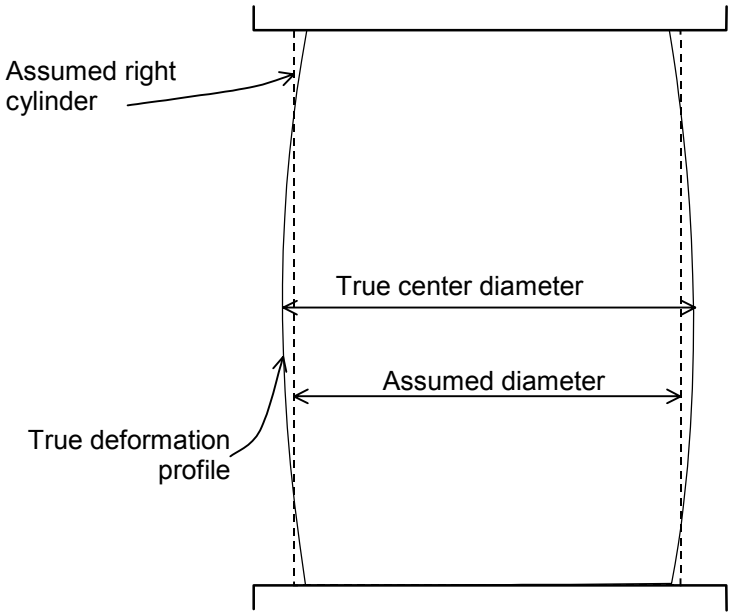

Figure 4.52 The difference between the centre diameter of the soil cylinder and the mean diameter assumed by Bishop and Henkel (1957).

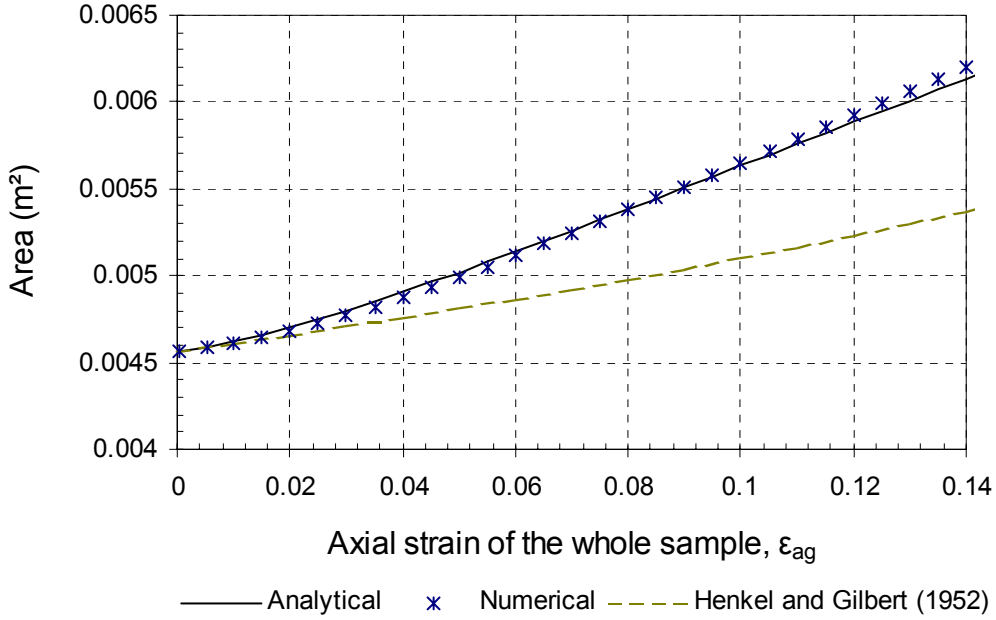

Figure 4.53 *Comparison of the horizontal cross-sectional area at the centre of the triaxial test sample calculated with the analytical and numerical methods.*

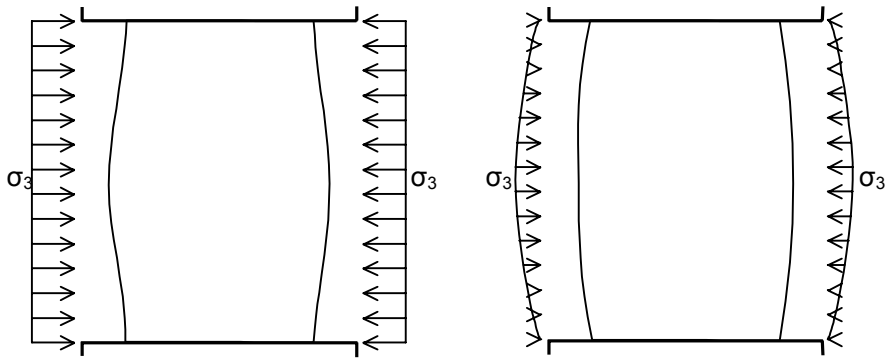

a) Uniform confining stress

b) Non-uniform confining stress due to membrane action

Figure 4.54 *The difference in the deformation profile for a soil cylinder under uniform confining stress and non-uniform confining stress due to membrane action.*

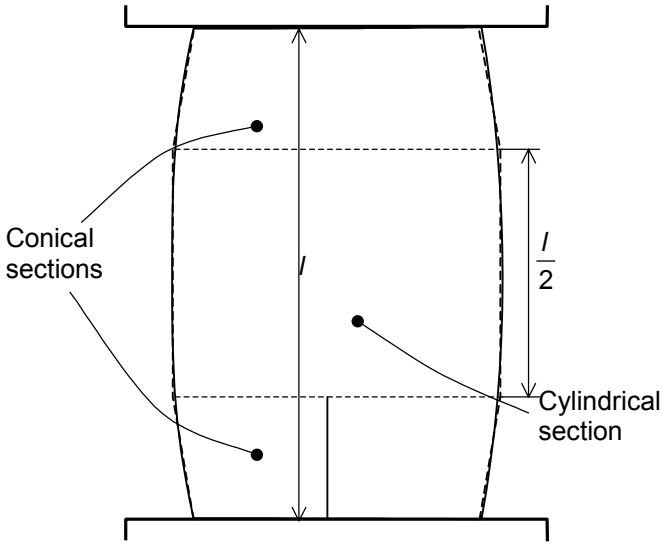

Figure 4.55 *Comparison between the deformation profiles obtained from numerical analysis and a cone and cylinder composite.*

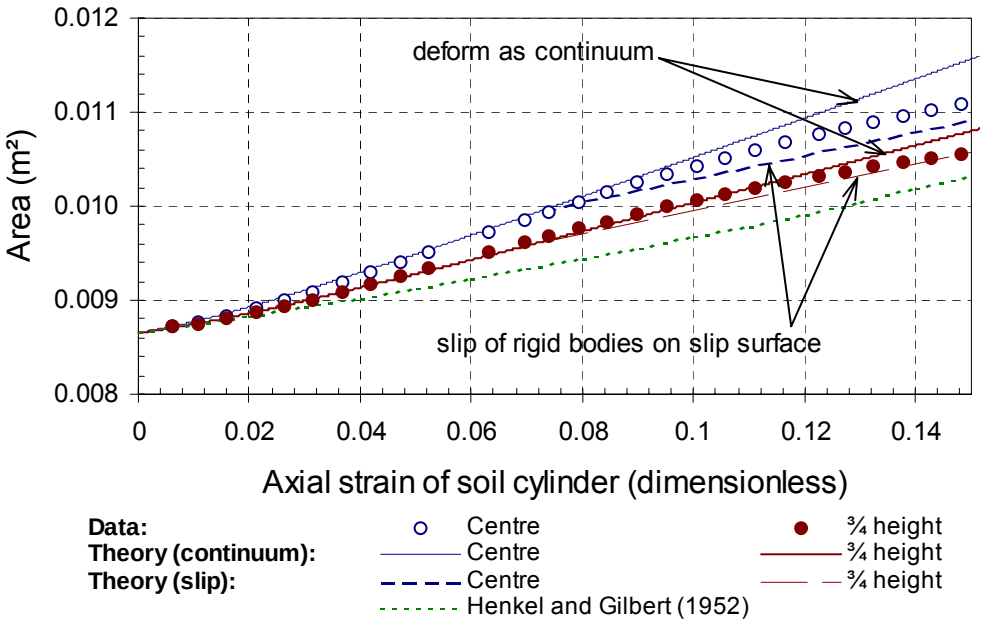

Figure 4.56 *Comparison between measured and calculated cross sectional area at the centre and at quarter height of the soil cylinder.*

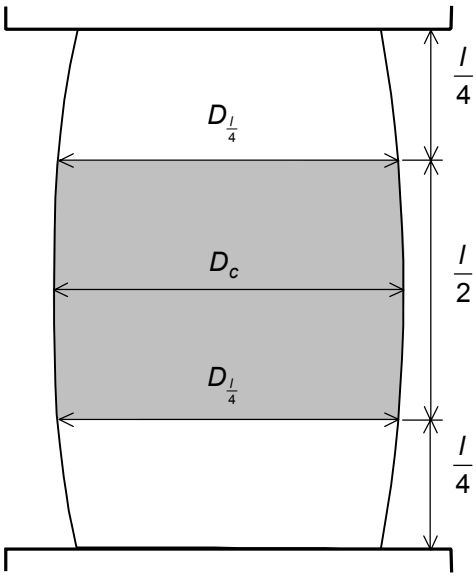

Figure 4.57 The diameters at different locations in the soil cylinder.

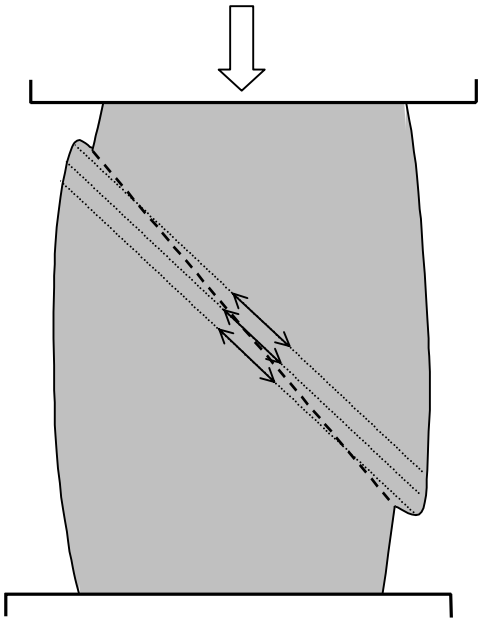

Figure 4.58 Diagonal tension in the membrane due to slip deformation.

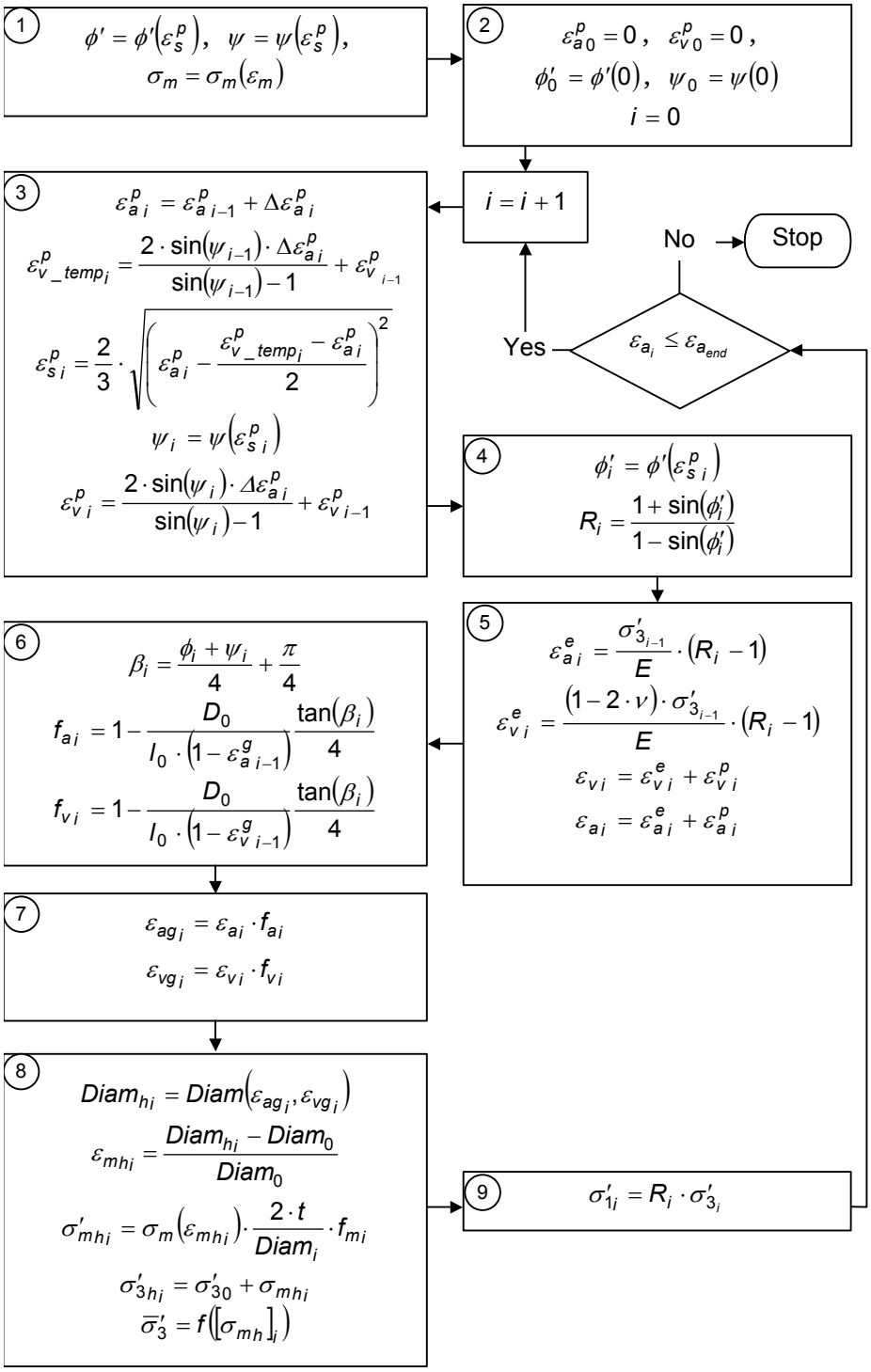

Figure 4.59 Flow chart outlining the calculation procedure for the stress-strain behaviour of granular soil confined in a single geocell.

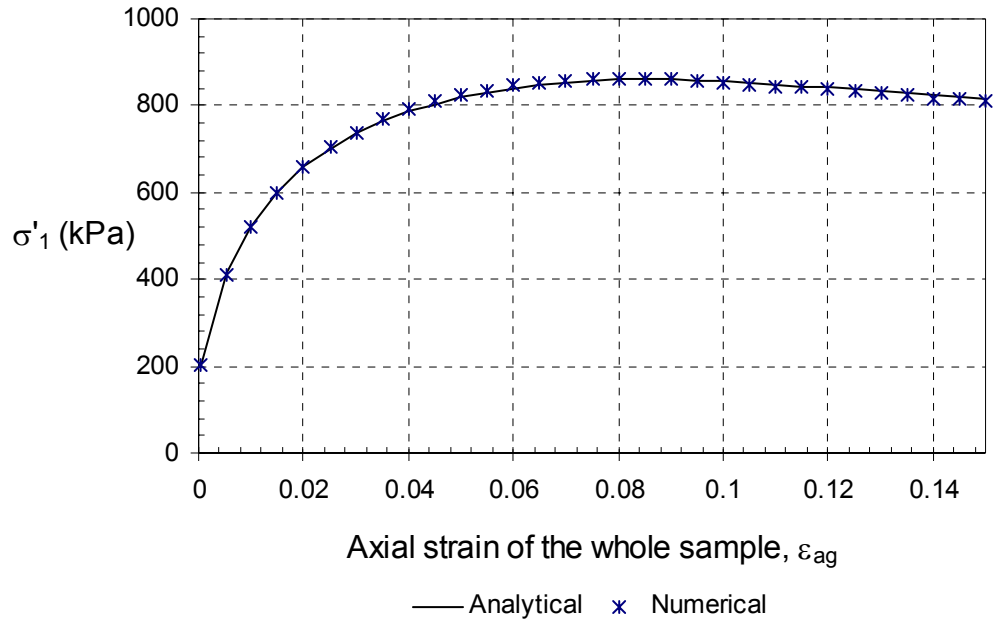

Figure 4.60 *Stress-strain curve for the soil obtained from numerical and analytical procedures.*

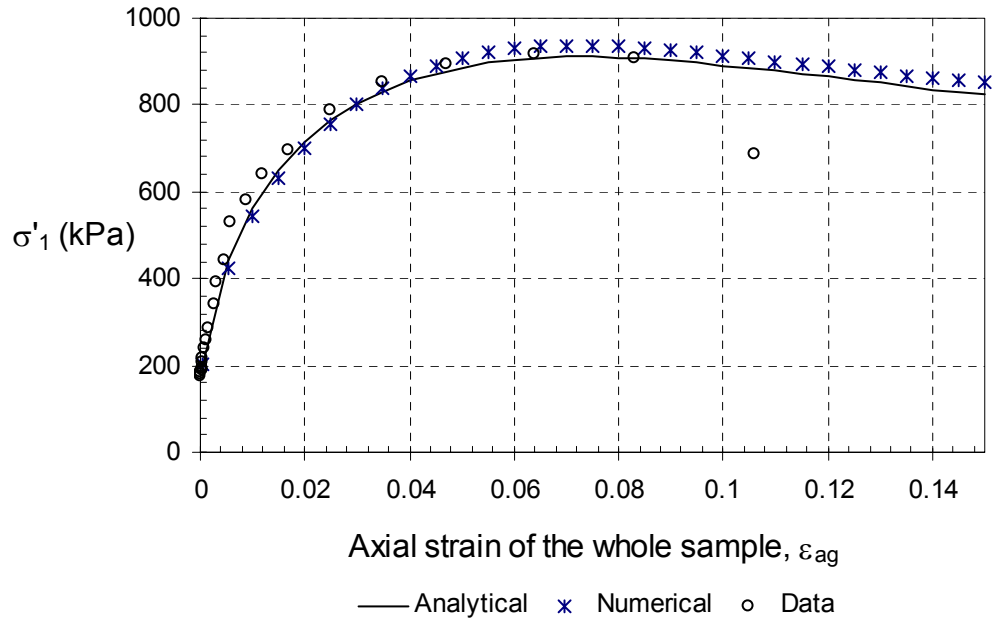

Figure 4.61 *Comparison between the measured and predicted stress-strain response for a triaxial test.*

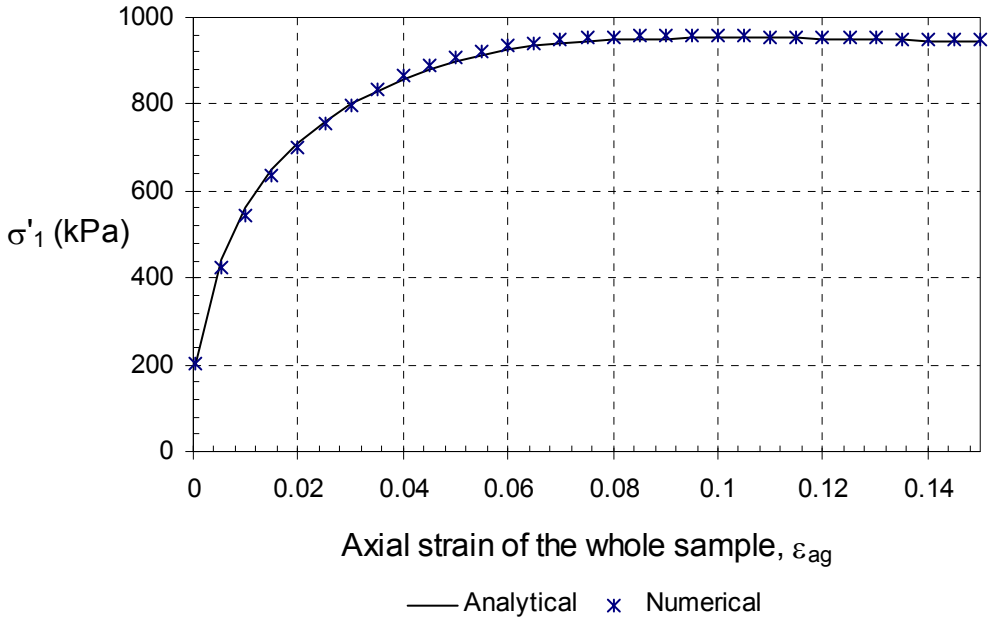

Figure 4.62 *Comparison of the stress-strain response for a single geocell with high confining stress, predicted by the numerical and analytical methods.*

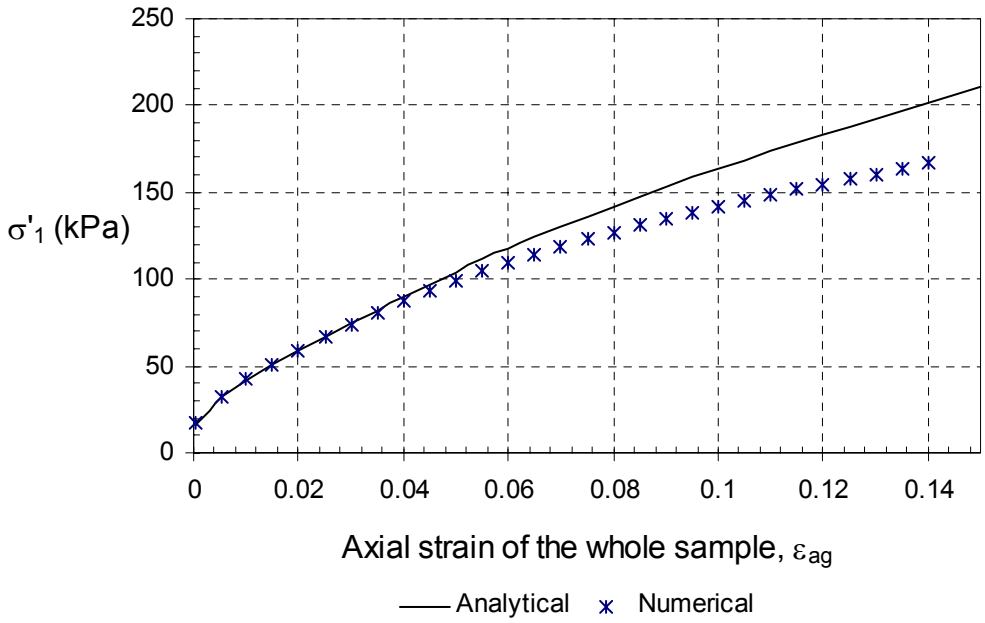

Figure 4.63 *Comparison of the stress-strain response for a single geocell predicted by the numerical and analytical methods, σ_3 =10 kPa, linear elastic membrane.*

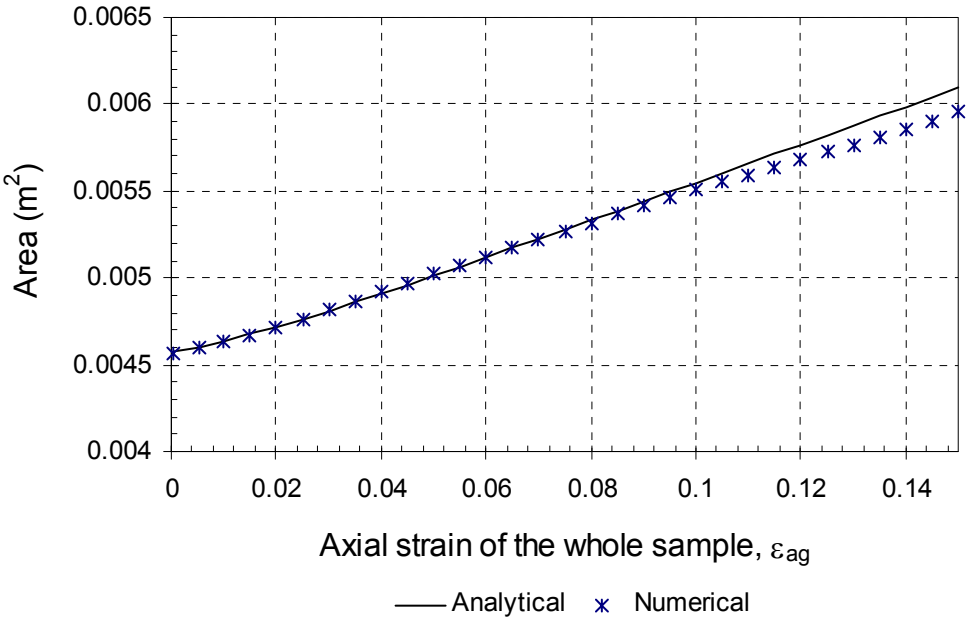

Figure 4.64 *Comparison of the cross sectional area at the centre of the soil cylinder, predicted by the numerical and analytical methods, σ_3 = 10 kPa, Linear elastic membrane.*

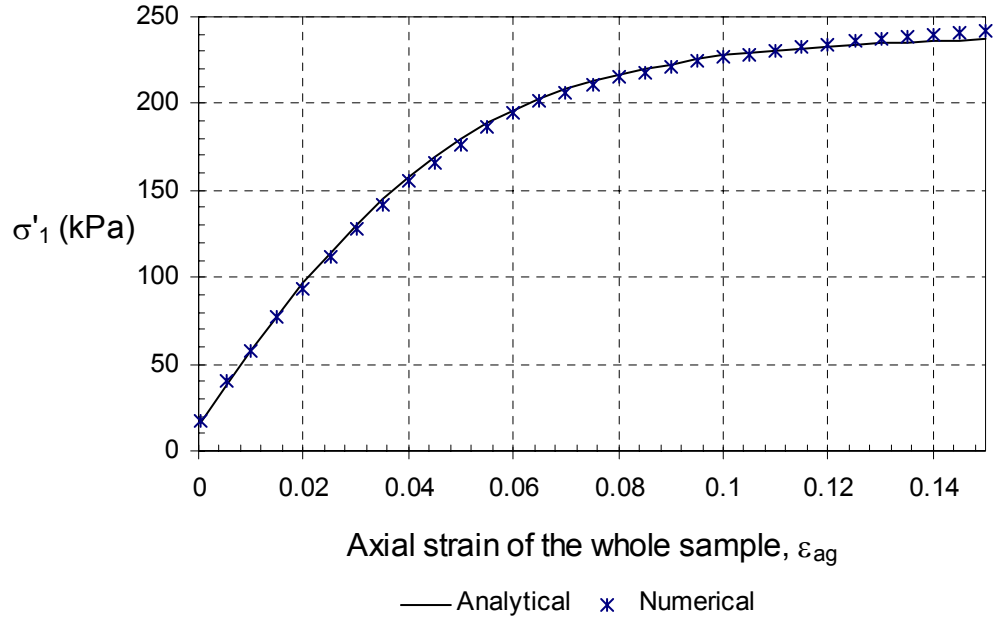

Figure 4.65 *Comparison of the stress-strain response for a single geocell with a non-linear geocell membrane, predicted by the numerical and analytical methods.*

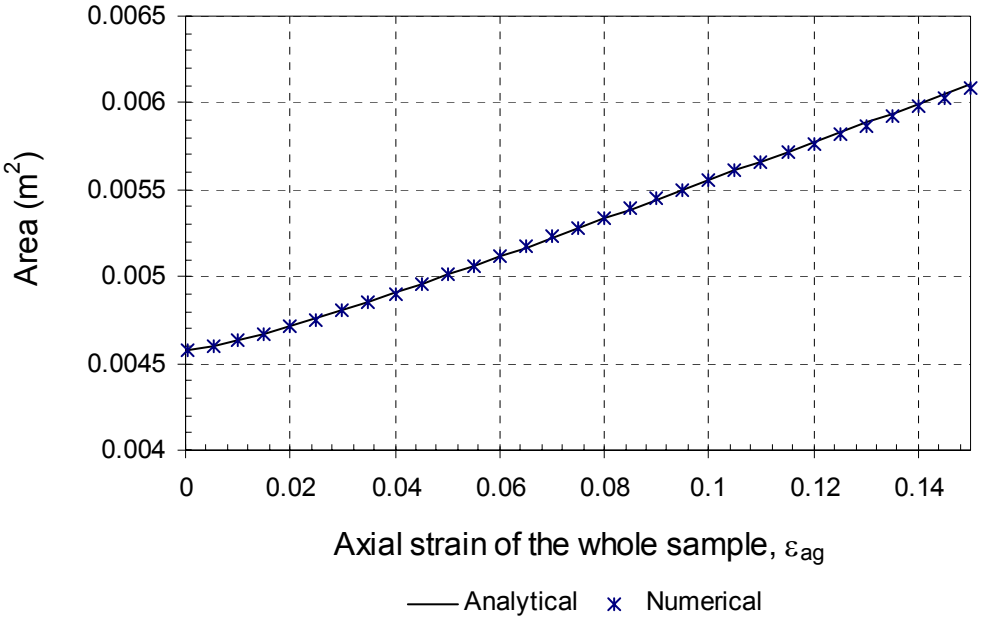

Figure 4.66 *Comparison of the cross sectional area at the centre of the soil cylinder with a non-linear geocell membrane, predicted by the numerical and analytical methods.*

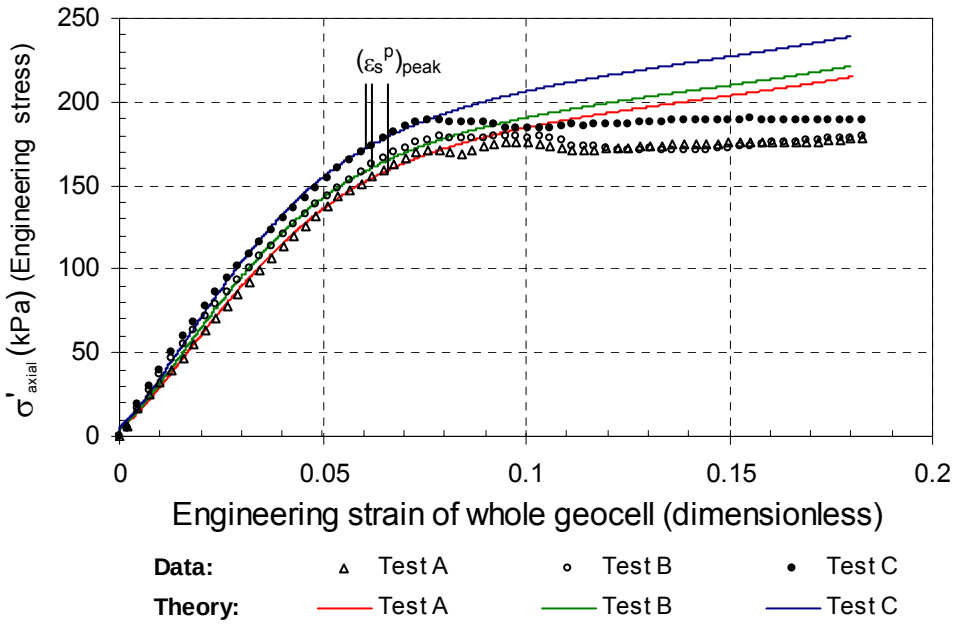

Figure 4.67 *Comparison between the measured and theoretical stress-strain response of single cell geocell systems.*

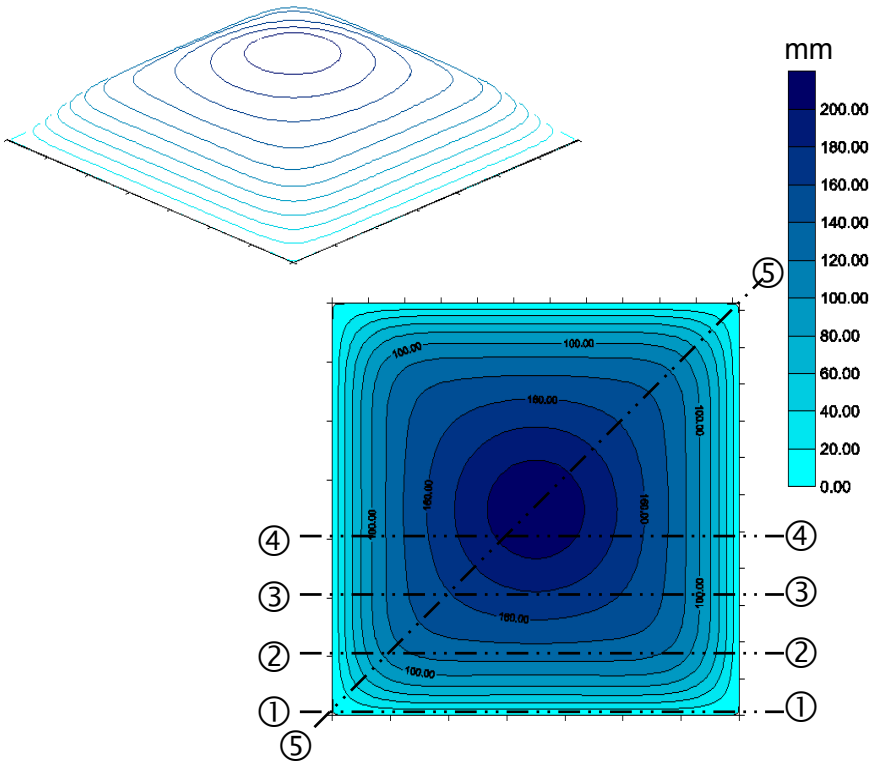

Data along sections lines 1-5 are shown in Figure 4.69

Figure 4.68 Three dimensional representation of the geometry of the measured "dead zone" in the 7x7 cell compression test.

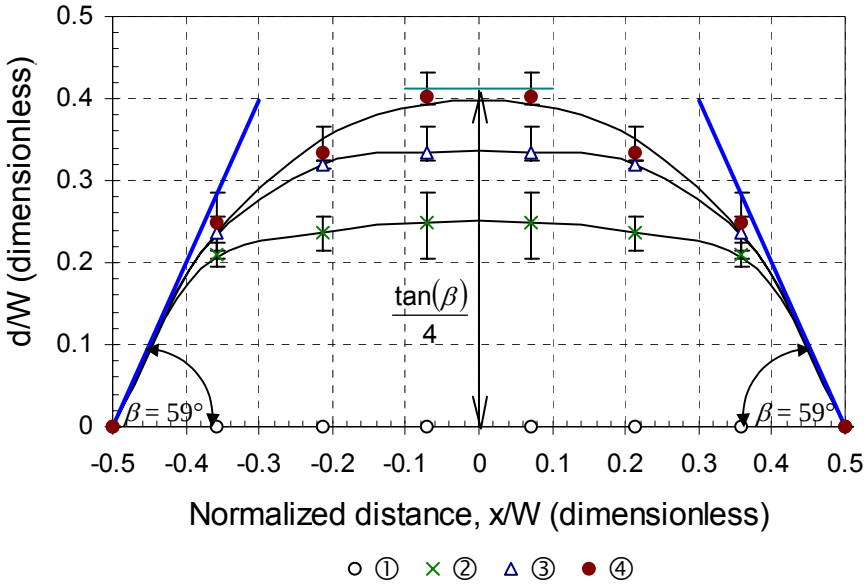

a)

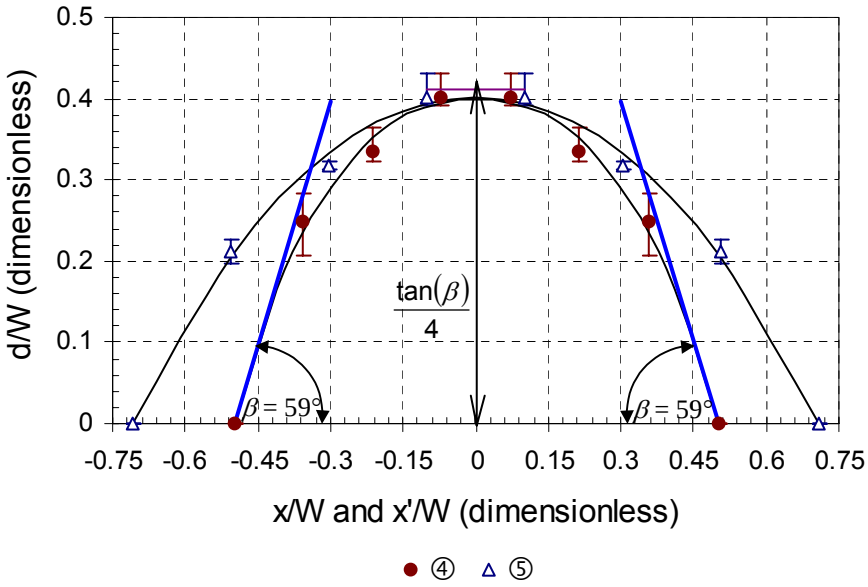

b)

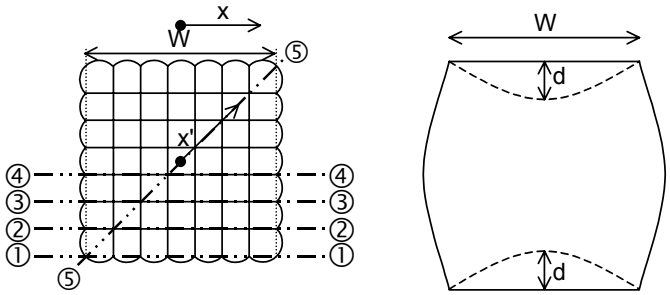

c)

Figure 4.69 *The β angle and theoretical maximum depth of the "dead zone" at peak, superimposed on the "dead zone" obtained from measurements.*

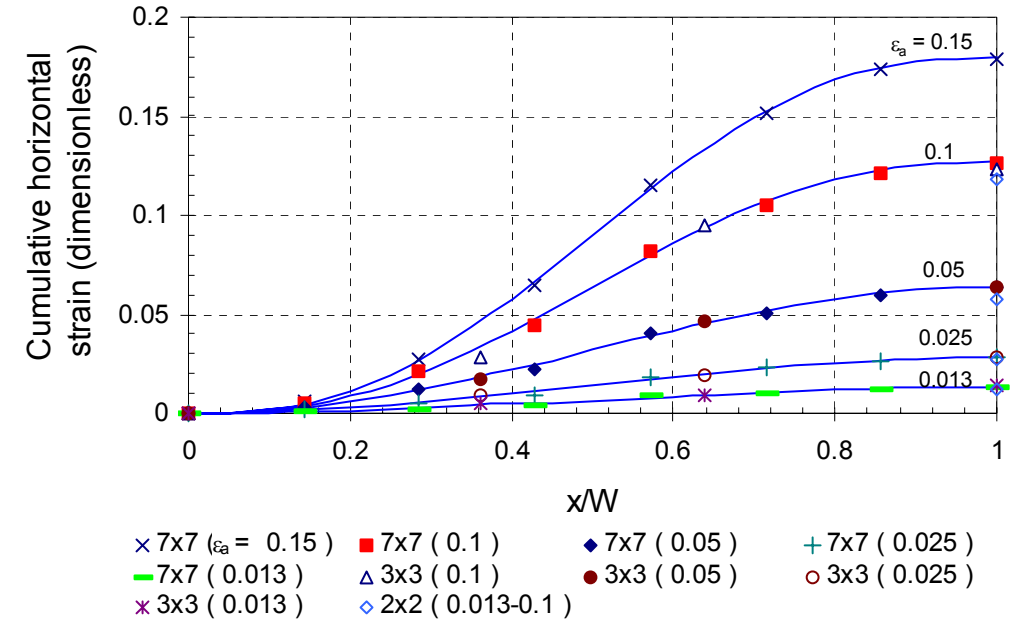

a)

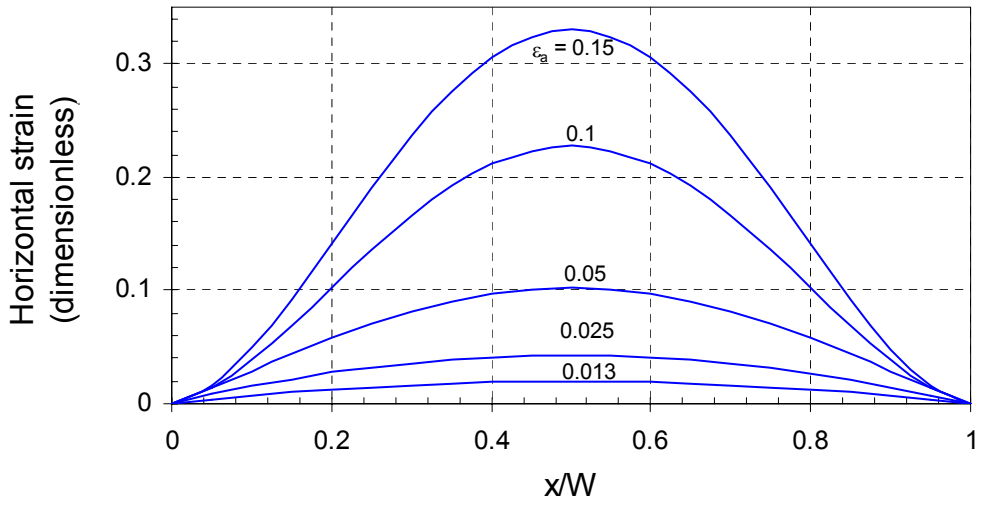

b)

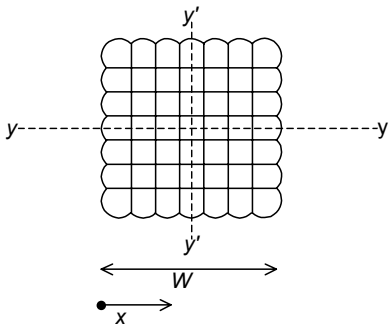

Figure 4.70 *Horizontal strain distribution at mid-height in 3x3 and 7x7 cell packs along the symmetry axis y-y.*

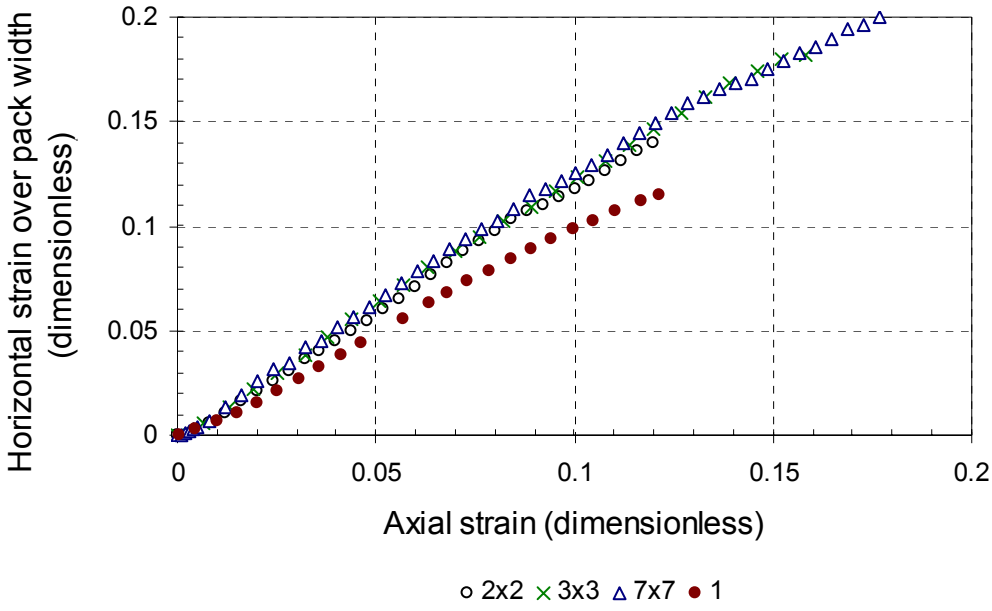

Figure 4.71 Measured horizontal strain over the whole pack width at mid-height.

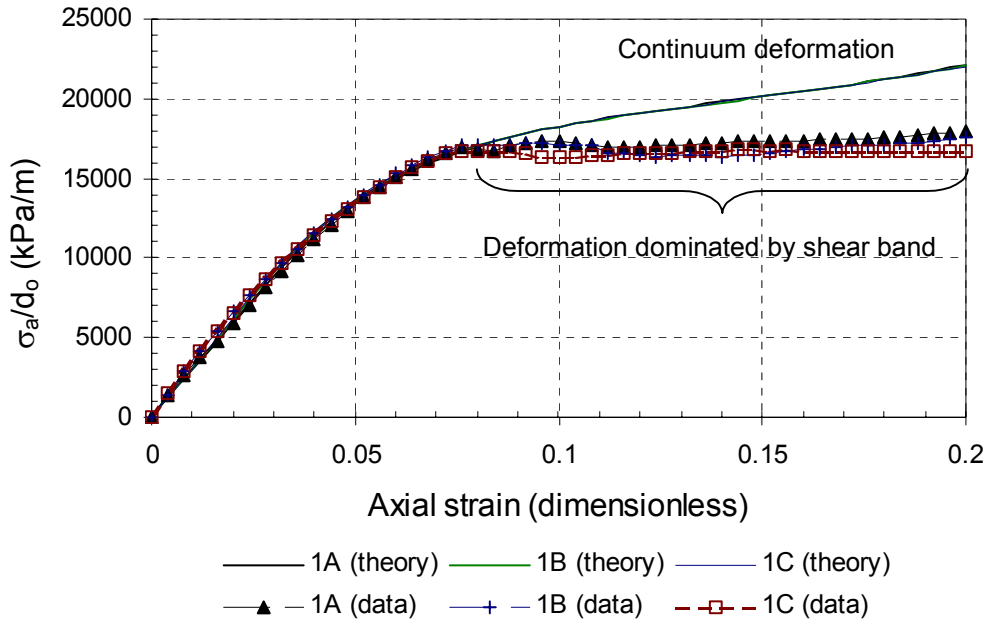

Figure 4.72 *Experimental and theoretical stress-strain curves for the single cell tests normalized with respect to cell diameter.*

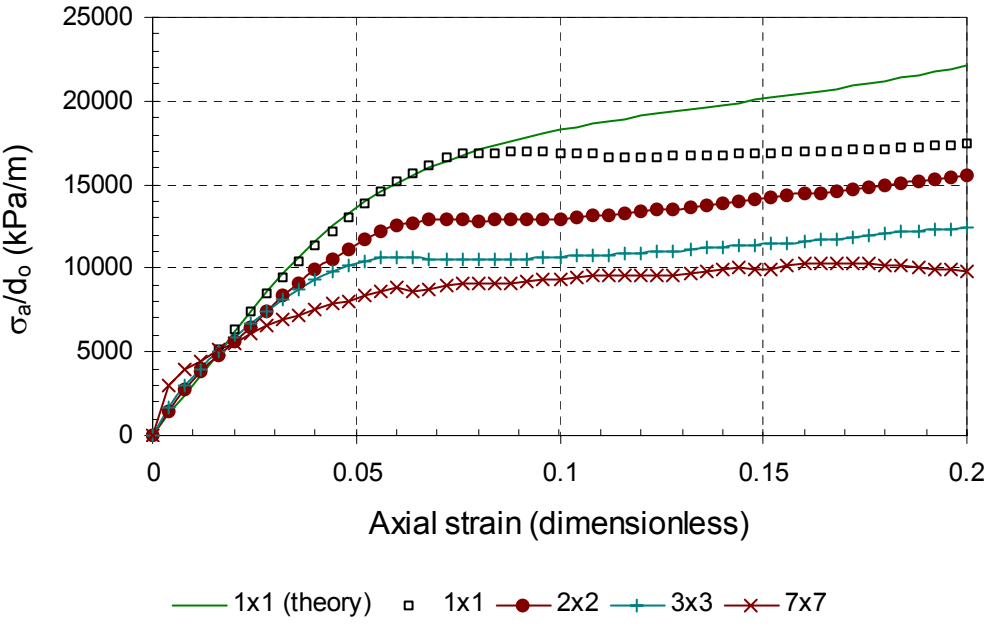

Figure 4.73 *Experimental stress-strain curves for multi-cell packs normalized with respect to original cell diameter.*

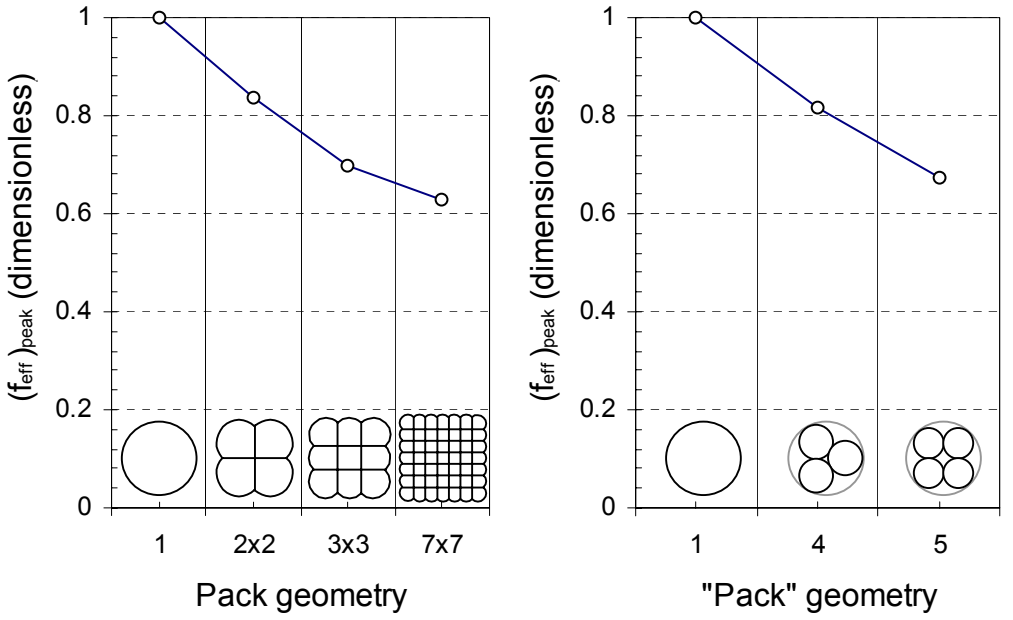

a) Data from current study

b) Data from Rajagopal et al. (1999)

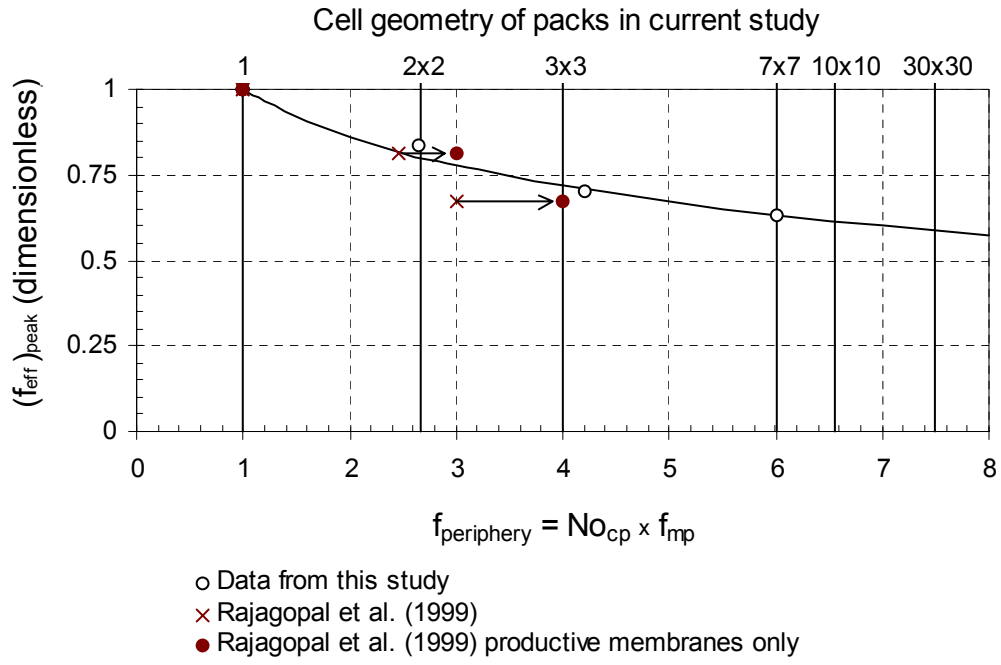

No_{cp} = the number of cells on the periphery, f_{mp} = the fraction of membranes belonging to only one cell.

c)

Figure 4.74 Efficiency factor with a change in the pack geometry.

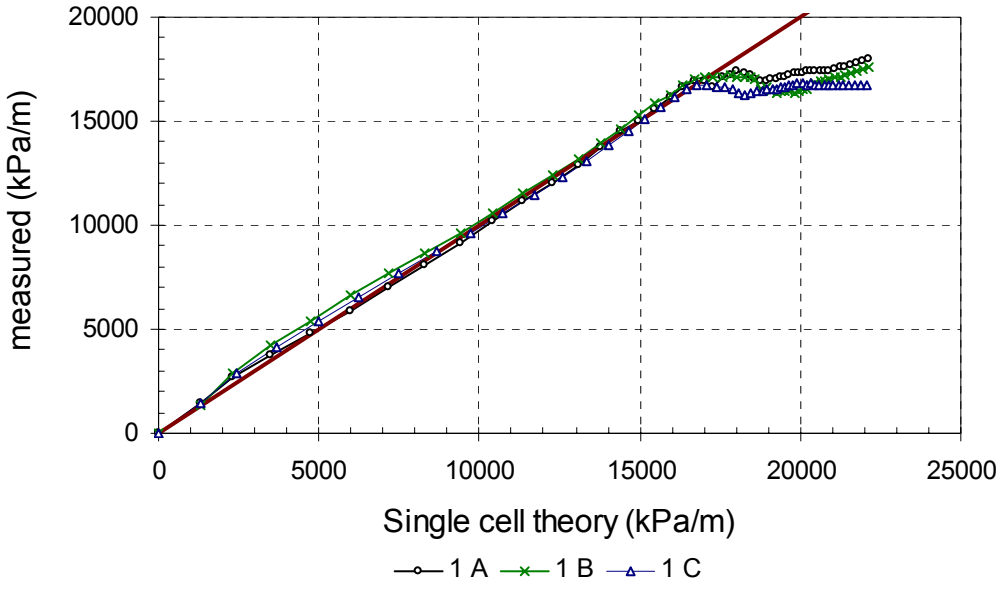

a) Single cell geometry

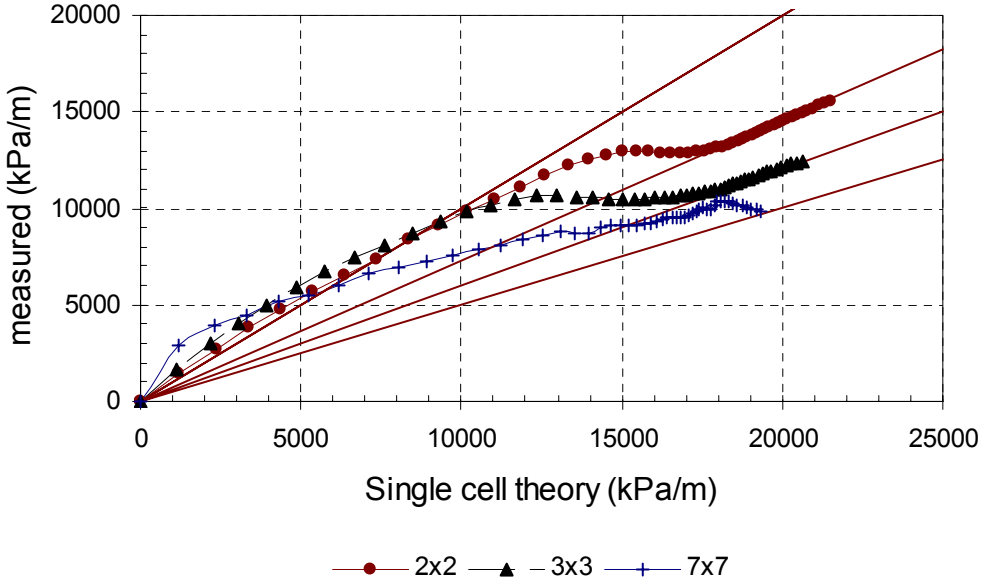

b) Multiple-cell geometry

Figure 4.75 Comparison between measured stress-strain curves and the single cell theoretical curve in normalized stress space.

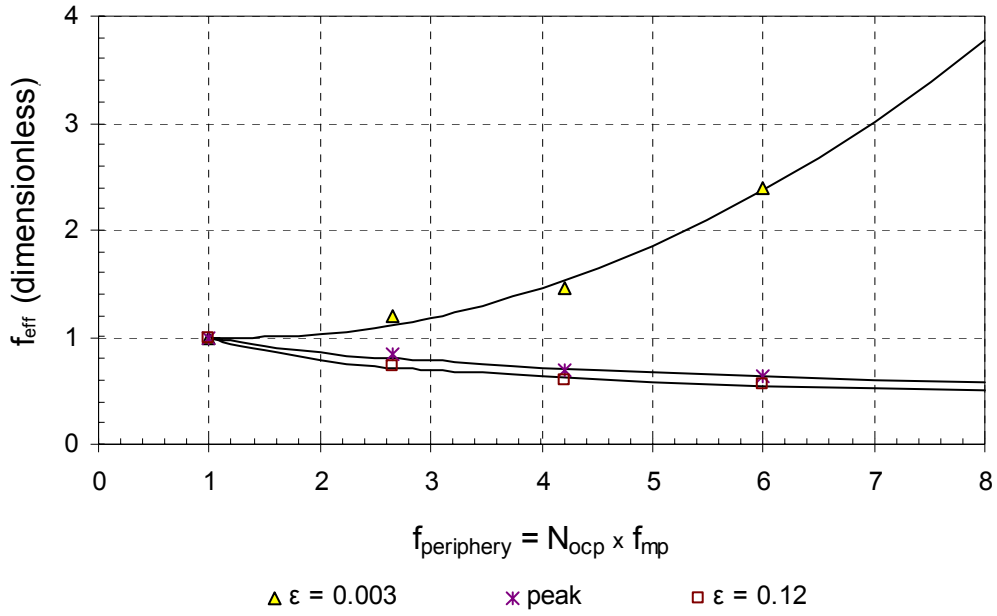

Figure 4.76 The efficiency factor for the packs at different axial strains.